

Dissertation

submitted to the

**Combined Faculties for the Natural Sciences and for Mathematics
of the Ruperto-Carola University of Heidelberg, Germany
for the degree of Doctor of Natural Sciences**

Put forward by

Diplom-Physikerin Christine Ruhland

born in Groß-Gerau, Germany

Oral examination: June 29th, 2011

SIGNPOSTS OF HIERARCHICAL MERGING

Referees:

Prof. Dr. Hans-Walter Rix

Prof. Dr. Eva Grebel

Zusammenfassung

In einem Λ CDM Universum spielt die Verschmelzung von Galaxien eine Schlüsselrolle in deren Entstehung und Entwicklung. Diese Arbeit konzentriert sich auf die Untersuchung von zwei Aspekten in diesem Zusammenhang.

Der Erste bezieht sich auf die Akkretion von Satellitengalaxien auf Scheibengalaxien, im Besonderen auf die Milchstraße. Dabei wird die Galaxie in ihrer Morphologie kaum beeinflusst. Jedoch wird dadurch zum Aufbau der Sternpopulationen in der lichtschwächsten, aber ausgedehntesten, Komponente der Galaxie beigetragen, dem stellaren Halo. Ich habe Techniken entwickelt stellare Ströme, die durch Gezeitenkräfte aus Satellitengalaxien gebildet werden, zu entdecken und erforschen. Das Hauptergebnis ist die Entdeckung eines Kandidaten für einen stellaren Strom und die detaillierte Charakterisierung des Sagittarius Gezeitenstroms, der eine entscheidende Rolle in der Erforschung des Potentials der Milchstraße spielt.

Das andere Projekt konzentriert sich auf die Erforschung von elliptischen Galaxien von denen geglaubt wird, dass sie das Ergebnis der Verschmelzung von Scheibengalaxien sind. Ich zeige, dass die beobachtete Entwicklung ihrer Farben-Helligkeitsbeziehung (ein Indikator ihrer Sternpopulationen) konsistent ist mit einer konstanten Hinzufügung von Galaxien mit kürzlich gestoppter Sternentstehung.

Diese Studien zeigen auf beiden Skalen Konsistenz mit der Vorstellung, dass Verschmelzungen eine wichtige Rolle in der Gestaltgebung von Galaxien spielten und weiterhin spielen.

Abstract

In a Λ CDM universe, the merging of galaxies plays a key role in their formation and evolution. In this thesis I focus on two aspects of this picture.

The first one is the accretion of satellite galaxies onto disk galaxies, specifically the Milky Way, leaving the galaxy mostly undisturbed in its morphology, but contributing to the stellar populations of its faintest, but most extended component, the stellar halo. I have developed techniques for detecting and exploring stellar streams formed through the tidal disruption of satellites. The main results are the discovery of a candidate stellar stream, and detailed characterization of the Sagittarius tidal stream, a key probe of the Milky Way potential.

In the other project, I explore the evolution of early-type galaxies — thought to be the result of merging of disk galaxies. I show that the observed evolution of their color-magnitude relation (a probe of their stellar populations) is consistent with a constant addition of galaxies with recently truncated star formation.

On both scales these studies are consistent with the notion that merging has played an important role in shaping the galaxies as we see them in the present day universe and continues to do so.

In memory of dear friends

CONTENTS

1	Introduction	3
1.1	Bimodality in the Galaxy Population	3
1.1.1	Red Sequence	4
1.1.2	Blue Cloud	6
1.2	Hierarchical Structure Build-up	7
1.2.1	Formation of Disk Galaxies	10
1.2.2	Dwarf Galaxies	10
1.2.3	Accretion of Satellites	11
1.2.4	Major Mergers and Morphological Transformation of Galaxies .	12
1.3	Thesis Outline	15
I	Studying the Assembly History of Disk Galaxies	17
2	Introduction - The Stellar Halo	19
2.1	Early Studies of the Halo Formation	19
2.2	Development of the Current Formation Picture	20
2.2.1	Formation of Tidal Streams	21
2.2.2	Dwarf Galaxies Companions	22
2.2.3	Characterization of the Halo as a Whole	23
2.3	Stellar Halos and Tail Tails Around Other Disk Galaxies	24
2.4	Stellar Streams as Probes of the Potential	26
3	Search for Stellar Streams in the Milky Way Halo	29
3.1	The Sloan Digital Sky Survey	29
3.2	Blue Horizontal Branch Stars	30
3.2.1	Spectroscopic Classification	31

CONTENTS

3.2.2	Photometric Classification	35
3.2.3	Empirical Distance Uncertainties	38
3.3	Coordinate Transformations	42
3.4	Techniques for Finding and Studying Structures	49
3.4.1	Structure Search in Distance Slices	49
3.4.2	Nearest Neighbors Alignments	49
3.4.3	Spectroscopic Follow-up	55
3.5	Summary	59
4	The Structure of the Sagittarius Stellar Stream as Traced by Blue Horizontal Branch Stars	61
4.1	Introduction	61
4.2	Data	64
4.2.1	Blue Horizontal Branch Stars	64
4.2.2	N-Body Models for the Sgr Stream	67
4.3	Results	67
4.3.1	Probabilistic BHB Density Maps	67
4.3.2	Thickness of the Leading Arm, and Spatial Selection of Sgr BHB Star Candidates	73
4.3.3	Bifurcation of the Leading Arm Perpendicular to the Plane	77
4.3.4	Kinematics and Comparison to Models	78
4.3.5	Selection of a ‘Clean Sample’ of BHB Star Candidates	84
4.4	Discussion and Conclusions	89
II	Studying the Formation of the Elliptical Galaxy Population	93
5	The Evolution of the Scatter of the Cosmic Average Color-Magnitude Relation: Demonstrating Consistency with the Ongoing Formation of Elliptical Galaxies	97
5.1	Introduction	98
5.2	Data	99
5.2.1	Intermediate redshift data	100

5.2.2	The low-redshift sample from the Sloan Digital Sky Survey . . .	103
5.3	<i>k</i> -corrections	103
5.4	Results	104
5.4.1	Selection of Red Sequence Galaxies	104
5.4.2	Fitting the Red Sequence	105
5.5	Interpretation	111
5.5.1	The evolution of single bursts	112
5.5.2	The evolution of galaxies with truncated star formation	113
5.5.3	Expectations for the Scatter Measurement	113
5.5.4	Blue Spheroids	119
5.6	Discussion and Conclusions	120
III Conclusions and Outlook		125
6 Summary & Conclusions		127
7 Outlook		131
Bibliography		144
Acknowledgements		145

CONTENTS

LIST OF FIGURES

1.1	Color-magnitude diagram from Blanton (2006)	4
1.2	Elliptical galaxies	5
1.3	Lenticular galaxy	5
1.4	Disk galaxies	6
1.5	Cosmological simulations of structure formation	9
1.6	Cosmological simulation of the formation of Milky Way sized halos	10
1.7	Simulation of disk galaxy formation	11
1.8	Observations of galaxy mergers	13
1.9	Simulation of galaxy mergers	14
2.1	Distribution of halo stars in the SDSS field	21
2.2	Stellar halo formation simulations	25
2.3	The Andromeda halo as seen in the PAndAS	26
2.4	Galaxies showing substructures in their halos	27
3.1	Color-color diagram of SDSS DR6 stars with spectra	32
3.2	Typical spectrum of a high-S/N BHB star	33
3.3	Comparison between normalized BHB star and BS star spectra	34
3.4	Selection resulting from the f_m vs. $D_{0.2}$ method	34
3.5	b_γ vs. c_γ selection method	36
3.6	Photometric BHB star selection	37

LIST OF FIGURES

3.7	The BHB section of the color magnitude diagram for the Ursa Minor dwarf spheroidal galaxy	39
3.8	Distance accuracy for individual BHB stars	40
3.9	Heliocentric distance slices	50
3.10	Galactocentric distance slices	51
3.11	Nearest neighbor alignment visualization	53
3.12	Nearest neighbor alignment visualization, stream candidate detection slices	53
3.13	Stream candidate distance slice in BHB stars	54
3.14	Overdensity maps	54
3.15	Example for the identification of spectroscopic follow-up candidates	56
4.1	Distribution of M giants in the Sgr plane	66
4.2	Density maps of BHB stars in the Sgr plane with different probability cuts	69
4.3	Density maps of BHB stars in the Sgr plane with color cut	70
4.4	On-sky view of the trailing arm distance shell	71
4.5	Comparison of BHB star data with models in a prolate potential	74
4.6	Heliocentric distance as a function of orbital longitude	75
4.7	Distribution of heliocentric distances for an angle slice	76
4.8	On-sky visualization of the bifurcation	79
4.9	Mean distance and line-of-sight thickness of the two branches	80
4.10	Comparison of the BHB star data with different models	82
4.11	Heliocentric radial velocity as a function of orbital longitude	85
4.12	Distance and velocity dispersions	90
5.1	The distribution of the spectroscopic redshift samples	100

5.2	Measured colors in 606–850 as a function of redshift	102
5.3	Assessment of the k -correction uncertainties	107
5.4	Color-magnitude diagram for $U - V$ against M_V at restframe	108
5.5	CMR intercepts in $U - V$ as a function of redshift	111
5.6	Evolution with redshift for different metallicities	112
5.7	Model tracks with truncated star formation	114
5.8	The integrated number of truncated galaxies as a function of cosmic age	115
5.9	Illustration of the metallicity dependence of galaxy colors	116
5.10	Modeled red sequence evolution	117
5.11	Metallicity distribution for the modeled galaxy sample	118
5.12	Blue spheroid ratio as a function of redshift	121
5.13	On-sky distribution of spectroscopic redshift sample	124

LIST OF FIGURES

LIST OF TABLES

3.1	Distances to clusters and dwarf spheroidals	41
3.2	Stream candidate stars	59
4.1	Width of the leading arm	76
4.2	Distances and widths of the two branches of the bifurcated stream . . .	78
4.3	Radial velocities of the leading arm	84
4.4	Sample selected for a high probability of association with Sagittarius. .	88
5.1	Color intercepts and scatter	109
5.2	Measured scatter of the red sequence compared with simulated values .	116
5.3	Spectroscopic redshifts from different catalogs	123

INTRODUCTION

We are probably nearing the limit of all we can know about astronomy.

SIMON NEWCOMB (1835-1909)

THE MILKY WAY as a ribbon spanning over the night sky has been ‘observed’ for thousands of years, but the realization of the true nature of this band of light and its connection with other luminous ‘clouds’ is a relatively new discovery. Understanding the nature and evolution of these galaxies of different shapes and sizes has been a rapidly evolving field especially in the last few decades.

Although individually different in their detailed appearance, the galaxy population in the present day universe shows much regularity. This can be understood in the context of the common aspects in their formation history in which the gravitational attraction of matter plays a key role. In this chapter I introduce the properties of high mass galaxies in the present-day Universe, focusing on their broad-brush properties, followed by an overview of the cosmological picture of structure formation, starting from the very beginning of the universe to the formation, evolution and transformation of galaxies to their appearance today.

1.1 Bimodality in the Galaxy Population

Attempts to classify galaxies to understand their formation and evolution date back several decades (e.g., Hubble, 1936), starting out with a classification mostly based on the morphology of the objects. As it has been already suggested in these early classification schemes, the luminous galaxy population in the present day universe can be divided roughly into two classes, following their observational properties: a featureless spheroidal type and a disk-dominated type. It is now clear that the structure of galaxies, which is reflecting the dynamics of the stars in galaxies, remarkably, is connected reasonably closely with the star formation histories, which reflects the history of the gas

content of the galaxies and its conversion into stars, and other properties of galaxies. One common way of thinking about this connection is to consider two broad classes of galaxies: the red sequence and blue cloud.

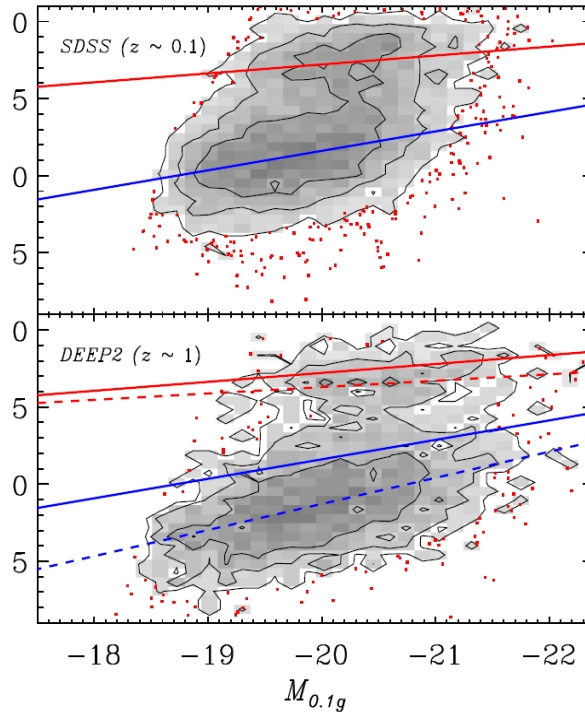


Figure 1.1: Color-magnitude diagrams at a redshift of $z \sim 0.1$ from the Sloan Digital Sky Survey (SDSS) and at $z \sim 1$ from the Deep Extragalactic Evolutionary Probe (DEEP2). The red sequence and blue cloud clearly show two concentrations with a red and blue line showing fits to the relations (solid for SDSS and dashed for DEEP2). Image taken from Blanton (2006).

1.1.1 Red Sequence

Red sequence galaxies have a tight correlation between their luminosities and colors (see Figure 1.1). It is populated by galaxies which are dominated by old stellar populations. They have practically no on-going star formation and very little gas. As old stars have lower surface temperatures than young stars their emission is noticeably redder causing the separation in the color regime, which is the main contribution to the separation in this diagram. Morphologically, these galaxies are bulge dominated systems, mostly elliptical or lenticular galaxies. In their projections on the sky many elliptical galaxies show a flattening in one axis compared to the other (Figure 1.2). This can not be explained with rotation (e.g., Davies et al., 1983; Bender & Nieto, 1990), rather the stars in elliptical galaxies show anisotropic velocity distributions. The highly flattened

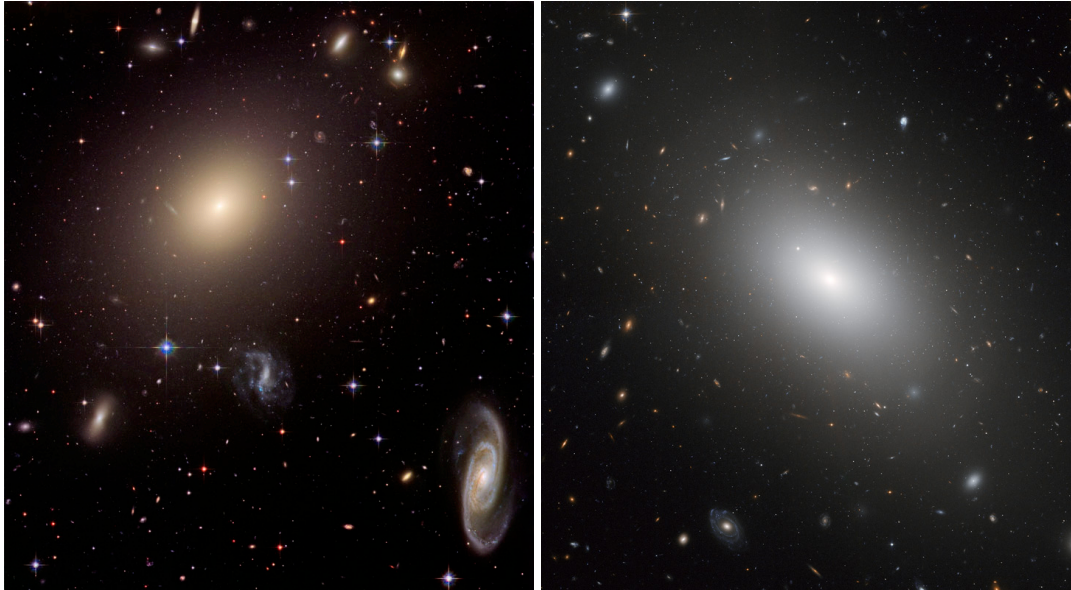


Figure 1.2: Elliptical galaxies: a galaxy in the Abell Cluster S0740 (ESO 325-G004, left panel) and NGC 1132 (right panel).

Image credit: NASA, ESA, and The Hubble Heritage Team (STScI/AURA).



Figure 1.3: The Sombrero Galaxy as a typical example for a lenticular galaxy. It shows a disk, but also a very prominent bulge.

Image credit: NASA and The Hubble Heritage Team (STScI/AURA).



Figure 1.4: Disk galaxies: the barred spiral NGC 1300 (left) and M101 (right).

Image credits: NGC 1300: NASA, ESA and The Hubble Heritage Team; M101: NASA, ESA, K. Kuntz (JHU), F. Bresolin (University of Hawaii), J. Trauger (Jet Propulsion Lab), J. Mould (NOAO), Y.-H. Chu (University of Illinois, Urbana), and STScI.

galaxies in this category can mostly be characterized as lenticular galaxies as they can be resolved into a central bulge and disk component (see Figure 1.3). Otherwise, galaxies in this category show close to no internal structure.

Elliptical galaxies are also called early-type galaxies as they were believed to be an early stage in galaxy evolution and would evolve into disk galaxies (which are therefore also called late-type galaxies). Today, the most popular picture for their formation suggests the opposite, namely that elliptical galaxies form out of the collision of two disk galaxies. This also provides an explanation why this group is hosting the most massive galaxies and also why, in contrast to disk galaxies, the stars in these galaxies are on randomly organized orbits. In Part II of this thesis I study the evolution of the red sequence and with that the evolution of the elliptical galaxy population.

1.1.2 Blue Cloud

A second concentration in the color-magnitude plane is build by the so-called blue cloud. The bluer color of these galaxies indicates that they have on-going star formation and young stellar populations. They are also morphologically distinct from red sequence galaxies as they are dominated by a rotating disk component. For their prominent disk component they are called disk galaxies or, as they mostly show spiral patterns in the disks, also spiral galaxies (Figure 1.4). For historical reasons they are also called late-type galaxies. They represent lower mass galaxies, but in numbers they are more common than the early-type galaxies.

In contrast to elliptical galaxies, disk galaxies mostly show clear internal structure.

The disks often have spiral arms, which show enhanced star formation compared to the interarm regions. Another common feature in the inner parts of the disk are bars. Furthermore, they mostly show a approximately spherical concentration of stars around their centers, the bulge, which is similar in kinematics and stellar populations to the elliptical galaxies as they also show randomly directed orbits and old stellar populations resulting in a more reddish color than the disk component. Another component of disk galaxies, which can only be observed in near-by galaxies due to a very low surface brightness, is the stellar halo. Both for the formation of the bulge and the stellar halo the accretion of stars from satellite galaxies is believed to have played a dominant role. Part I of this thesis will focus on the halo of the Milky Way and its substructure as traces of accretion events.

In the next section I summarize the current picture of galaxy formation which also gives an explanation for the evolution of two different types of large galaxies.

1.2 Hierarchical Structure Build-up

The current cosmological picture contains two ingredients which are not directly observable in lab experiments: dark matter and dark energy. They have been both postulated to provide an explanation for observations which could not be understood with luminous matter, also called baryonic matter, alone.

Dark matter was postulated as a form of matter which purely interacts via gravity. Although its nature is still unclear we have now a wealth of evidence for its existence. Here, the gravitational effects on the kinetics in and between galaxies is an important aspect which gave rise to the discovery of dark matter in the first half of the 20th century. Studying the motions of galaxies in the Coma cluster Zwicky (1933) found that the cluster mass, estimated taking the luminous matter, showed a mismatch with the kinetic energy of the cluster. Following the virial theorem the kinetic energy should equal half the potential energy, which was much higher in the case of the Coma cluster than the baryonic mass. Similar discoveries were made several decades later when the rotation curves of disk galaxies were studied finding that the motion of the matter in the disks was suggesting a higher mass than estimated by the surface brightness profiles of the galaxies (Rubin & Ford, 1970; Rubin et al., 1980). But galaxy kinematics are not the only sources of evidence for the existence of a not observable matter component in galaxies. The paths of photons are also affected by gravity known as the gravitational lensing. Here, galaxy clusters gave a second piece of evidence for their large dark matter content. The

strength of the light bending effect in several clusters (e.g. Abell 1689) can only be explained by an additional non-luminous matter component. Very special evidence is given by the Bullet cluster, which formed through the collision of two clusters. Through the gravitational lensing effect of this cluster a spatial separation between baryonic and dark matter was found, thought to be the result of the different characteristics of the two matter forms and their behavior in the merging event (Markevitch et al., 2004). Another indication for the existence of dark matter are observations of the large-scale structure and the Cosmic Microwave Background (CMB) which can not be explained with baryonic matter alone.

Observations of supernovae Ia revealed an accelerated expansion of the universe through the comparison for the distances of galaxies measured with these standard candles and their redshifts (Riess et al., 1998; Perlmutter et al., 1999), although one would rather expect the expansion to slow down under the influence of gravity. This led to the postulation of dark energy. Furthermore measurements of the anisotropies in the CMB suggested that the universe is close to flat. That requires an energy density in the universe which is equal to the critical density. However, baryons and dark matter were found to account only for about 30% of this value. To explain the remaining 70% an additional form of energy, dark energy, is needed. Likewise the large-scale structure also suggests that the density of matter is only 30% of the critical density.

The Λ Cold Dark Matter (Λ CDM) model is the simplest known model which is in general agreement with most observed phenomena like e.g. the cosmic microwave background, large scale structure and accelerating expansion of the Universe. Λ indicates that the so-called cosmological constant is assumed to be not zero. It originates from the dark energy making an accelerating expansion of the Universe possible. Ω_Λ gives the fraction of energy contained by dark energy, with a most probable value of 0.7 (Spergel et al., 2003).

In the Λ CDM model, all structure in the universe formed out of primordial density fluctuations as seeds for the formation of larger concentrations of matter. In this 'bottom-up' scenario small dark matter halos formed first and grew through subsequent accretion and merging with other halos. Over time also large halos formed through this process (see Figure 1.5 and 1.6). Structure growth in this manner goes on to the present day.

Density fluctuations on all scales were initiated by quantum fluctuations in the very early universe which increased to macroscopic size by inflation. The statistics on these

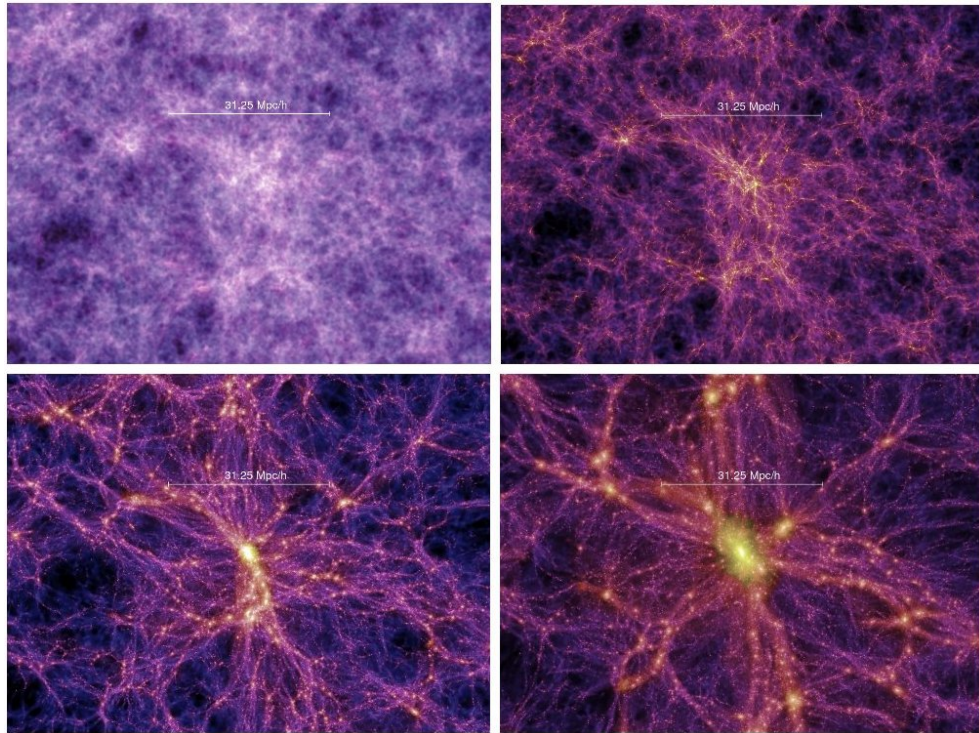


Figure 1.5: Cosmological simulations of structure formation show the concentration of dark matter over cosmic time. In this simulation (Springel et al., 2005) the frames show a region at 0.21, 1.0, 4.7 and 13.6 Gyrs after the Big Bang. These frames are centered on a region which represents the formation of a galaxy cluster.

fluctuations at the epoch of recombination give a very good description of the tiny fluctuations of around one part in 10^5 as they are seen today in the CMB with the Cosmic Background Explorer (COBE) and later the Wilkinson Microwave Anisotropy Probe (WMAP Spergel et al., 2003). Since dark matter is influenced by gravity alone, density fluctuations could already start to grow before recombination set in and baryonic matter could accrete. Not feeling the radiation pressure anymore, the recombined baryons could fall into the potential wells built by the dark matter particles (White & Rees, 1978). In the collapse the angular momentum is mostly conserved leading to flat, disk-like, gas concentrations within the dark matter halos while the gas is cooling down through emission of radiation (Zel'Dovich, 1970). Additionally to the further growth through the infall of gravitational attracted matter these initial density fluctuations also grew through merging with other small units of accreted matter.

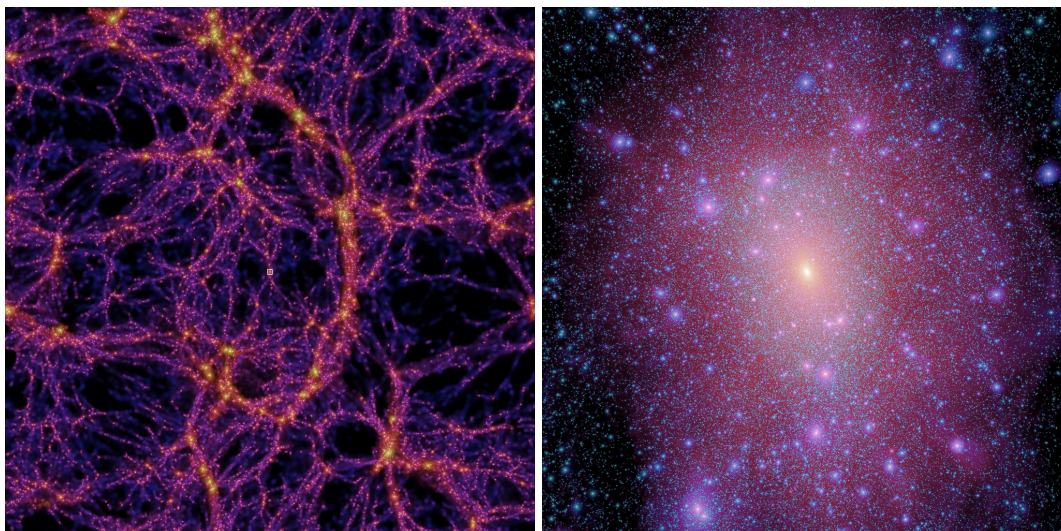


Figure 1.6: Dark matter simulation of a Milky Way sized halo from the Aquarius project. The left panel shows the full simulation box which is centered on the halo presented in the right panel in full resolution.

1.2.1 Formation of Disk Galaxies

In the mesh of dark matter filaments density concentrations grow mainly where these filaments are coming together. Dark matter and also baryonic matter is gravitationally pulled towards these concentrations from along the filaments. Dark matter plays an important role in this context as it started earlier to accrete and thus had already build potential wells to trigger the accretion of baryonic matter. In the center of the dark matter halo the gas reaches densities which allow it to cool and condense. Angular momentum conservation leads to the formation of a flat disk of gas, and as star formation sets in, also stars. The disk grows through the further accretion of material (see Figure 1.7). There are a number of models simulating the formation of disk galaxies in a cosmological framework (e.g., Navarro & Steinmetz, 1997; Abadi et al., 2003; Sommer-Larsen et al., 2003; Governato et al., 2007).

1.2.2 Dwarf Galaxies

Surrounding the major dark matter halos in which large galaxies can form, cosmological simulations predict a large number of smaller dark matter halos, also referred to as subhaloes. These subhaloes also accrete baryonic matter and form stars, although it is not clear yet if there is a lower mass limit for a dark matter halo to form stars. With the growing number of dwarf galaxies detected in the Local Group we start to learn to be able to address these questions. Typically these galaxies are highly dark matter

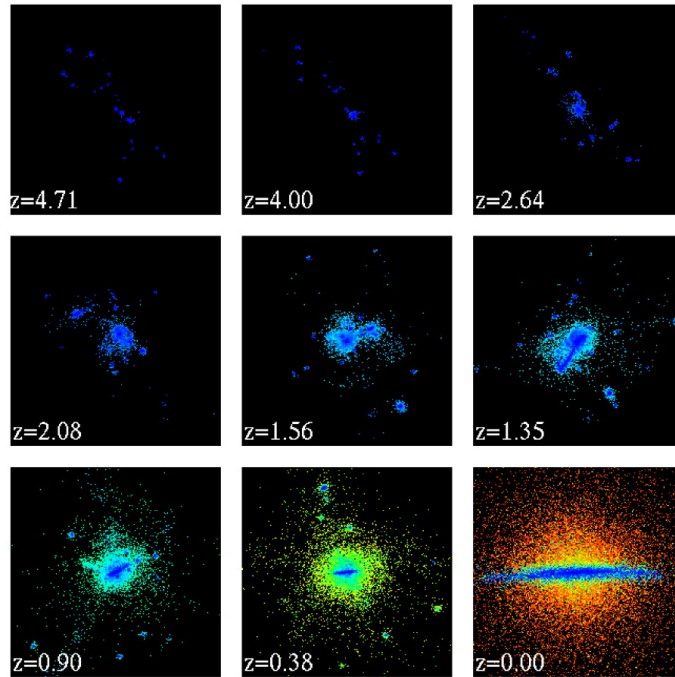


Figure 1.7: Star formation in a dark matter halo (Abadi et al., 2003). The gas settles into a disk in which stars form.

dominated systems hosting metal-poor stellar populations. I will discuss this population in a little more detail in Chapter 2.

1.2.3 Accretion of Satellites

As demonstrated by observations, and also predicted by Λ CDM, small galaxies dramatically outnumber large galaxies. Given that the massive galaxies are surrounded by a large number of small satellites, accretion of these satellites is bound to be an important growing mechanism besides the accretion of dark matter and gas.

In general, the outcome of a merging event is strongly dependent on the mass ratio between the merging galaxies. If one galaxy is much smaller than the other (‘minor merger’), the larger galaxy will be morphologically mostly unaffected by the merging event, whereas the smaller galaxy will dissolve in the gravitational potential of the larger one, adding its stars to the stellar populations of the host. Another effect on the large galaxy could be that it starts to form a bulge or the formation or addition of material to a stellar halo (Toth & Ostriker, 1992; Velazquez & White, 1999; Moster et al., 2010).

Also the disks of late-type galaxies can get disturbed by merging events with smaller galaxies, which can result in a distorted or thickened disk.

While a satellite orbits around the host galaxy gravitational forces act on it, causing it to dissolve and sink towards the center of the potential. In this process the main effects are tidal disruption and dynamical friction. Tidal forces are pulling the satellite apart due to the different strength of the gravitational field on its nearer and further side. This elongates the satellite until the stars get unbound. Another gravitational effect acting on the satellite is dynamical friction (Chandrasekhar, 1943a,b,c). As the satellite is moving through the potential of the larger galaxy the distribution of mass in the host changes due to the gravitational pull of the satellite. This results in the formation of mass concentrations along the orbit of the satellite. This increased density behind the satellite is decelerating it. Thus, dynamical friction causes the satellite galaxies to lose momentum, resulting in an infall towards the center of the potential. The stars which got unbound continue to follow approximately the orbit of the satellite, but due to the gravitational influence of the satellite and other mass concentrations in the halo, their orbits can evolve also quite a bit (e.g., Choi et al., 2007). This will be discussed in a bit more detail in the next chapter. In a non-spherical potential the orbit of the satellite will also precess. Over many orbits this will also cause the debris to cover a wider area of the halo.

The orbital angular momenta of the satellites are rarely aligned with the angular momentum of the disk, and so an approximately spheroidal stellar halo is expected to result from such a process. In Chapter 2 the formation of the stellar halo will be discussed in more detail.

1.2.4 Major Mergers and Morphological Transformation of Galaxies

The situation is different for mergers between galaxies of comparable mass ('major merger'). Here, processes will take place which will change the shape of the galaxies significantly. The detailed result of a merging event also depends on several other parameters like relative velocity or angular momenta of the merging components.

Among the huge amount of observed galaxies there is quite a number of interacting galaxy pairs. Although these interaction are not very common (only about 1% of galaxies), the long duration of the most violent merging phases, when the morphologies are



Figure 1.8: In this Figure images of different pairs of galaxies are arranged to represent snapshots in a typical merging event of two disk galaxies to one large elliptical galaxy. (Image credit: NASA, ESA, the Hubble Heritage Team)

most dramatically disturbed, allow the observation of many of these events. Given the timescales of these merging events we can only observe snapshots of different systems to build a global picture of a typical merging process. Figure 1.8 gives some examples of galaxies in different stages of a merger process arranged in a way to suggest a time sequence if we would look at a single pair of galaxies. Since the strange morphologies observed for some galaxies was considered to originated from the interaction of two galaxies and this was proposed as a possible formation mechanism for the formation of elliptical galaxies (Toomre & Toomre, 1972) extensive simulations brought some light in the understanding of the involved mechanisms (e.g., White, 1978; Barnes & Hernquist, 1996; Cox et al., 2006). Figure 1.9 shows a simulation of such an merger event.

Given the large distances between stars even in a direct ‘collision’ between two galaxies the stars themselves are extremely unlikely to collide. Rather, the forces acting on the stars are purely gravitational. Again, dynamical friction plays an important role in shaping the orbits of the stars, in the major merger case this affects both galaxies. Another effect acting on the galaxies is violent relaxation. The rapid changes of the potential well have a randomizing effect on the orbits of stars, such that stars which have been on initially very similar orbits can end up on very different final orbits. This is an important mechanism in the transformation of two merging disk galaxies to one large

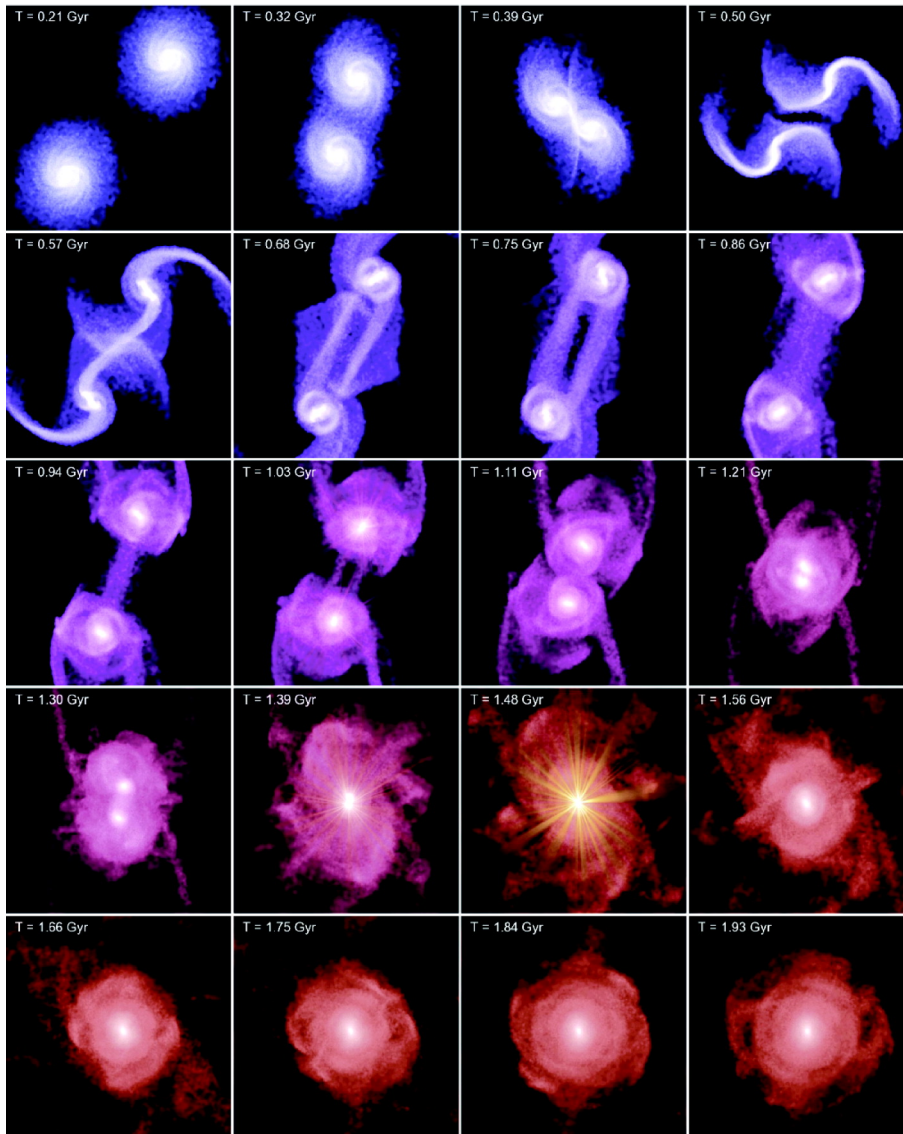


Figure 1.9: In most simulations of mergers between disk galaxies the resulting galaxy resembles something similar to an elliptical galaxy. This Figure shows such a simulation (Hopkins et al., 2006). The color is indicating that the baryonic gas fraction is decreasing in the process as the gas is consumed.

elliptical galaxy. The disks will be destroyed, with the disk population attaining a high velocity dispersion this can result in a transformation into a spheroidal component. In the rapidly changing potential well the gas which is initially located in nearly circular orbits, ends up in non circular orbits, leading to gas shocking and loss of angular momentum. This causes widespread gas compression and enhanced star formation. This is manifested in a generally enhanced star formation rate (SFR) in interacting galaxies (Robaina et al., 2009), and dramatic enhancements in some cases (e.g., Sanders & Mirabel, 1996). Another possible effect is that the super-massive black hole (SMBH) in the galaxy centers can be fed by the gas which would initiate active galactic nuclei (AGN) activity. Part of the matter is also lost in the intergalactic medium (IGM) which can be observed for instance in tidal tails. Through the violence of the interaction the remaining gas is either ejected or heated so strongly that any further star formation is suppressed. AGN feedback is expected to play an important role in the gas ejection (e.g., Springel et al., 2005).

1.3 Thesis Outline

In this thesis I will describe work that is related to the dark matter-driven assembly of galaxies. In this context I present work on two different projects:

In Part I of this thesis I present a study of the low density stellar halos of galaxies, in particular streams of stars from tidal disruption of dwarf galaxies. This work is following the path of trying to understand in detail how disk galaxies assemble in a cosmological context.

Part II focuses on the exploration of the star formation histories of the non-star forming galaxy populations, as a constraint on the formation history of the population. This is relevant to identifying the physical processes that give rise to non-star forming galaxies.

Part I

Studying the Assembly History of Disk Galaxies

INTRODUCTION - THE STELLAR HALO

SURROUNDING THE DISK and bulge of late-type galaxies are low-density clouds of stars which extend way further out, especially also perpendicular to the plane of the disk, than these denser components. They consist of old metal-poor stars which have, in contrast to the disk stars, high velocity components perpendicular to the plane of the disk. Despite the large volume occupied by the halo, the density is so low that the number of stars is a small fraction of the total number of stars in the galaxy. Although the apparent insignificance given the small contribution to the total mass of the galaxy, the halo is a valuable part of the galaxy when it comes to the study of the formation history. Due to the long dynamical times, the overall low density and the absence of in-situ star formation, structures are conserved over a long time and therefore can be used to study the formation history of the galaxy, and with that also serves as a laboratory to test theories of structure formation.

2.1 Early Studies of the Halo Formation

Eggen et al. (1962) started a completely new approach in studying the formation of our galaxy by using stellar abundances and dynamics for galactic archeology. For stars in the solar neighborhood they observed a strong correlation between the metallicity and the eccentricity. To explain this observation they proposed a model, referred to as monolithic collapse, in which the formation of stars should have taken place through the rapid collapse of a spheroidal cloud, the ‘protogalaxy’. The formation of the oldest stars would have happened early in this collapse around the time when the first stars in the universe were formed. More metal-rich stars then would have formed later when the cloud had settled into a disk. This scenario aimed to explain both the different metal abundances and orbital properties of stars in the disk and the halo of the Milky Way.

Later, Searle & Zinn (1978) found a wide range of metal abundances in the Galactic globular clusters independent of their distances to the Galactic Center, which argued more for a formation which took place over an extended period of time out of independent fragments. Also the distribution of stars in the halo shows a large amount of substructure. Bell et al. (2008) and Xue et al. (2010) showed that this is indeed consistent with the halo being entirely composed of the debris from dwarf galaxies. But there is a tendency towards higher oblateness and towards some rotation that may be harder to understand in a hierarchical framework (Chiba & Beers, 2000; Carollo et al., 2007) and may indicate the presence of a component formed in the potential well of the Milky Way.

2.2 Development of the Current Formation Picture

With the advent of surveys with both a large sky coverage and sufficient depth to get a detailed global picture of the halo, in particular the Sloan Digital Sky Survey (SDSS), the halo revealed a richness in structures.

With the discovery of the Sagittarius (Sgr) dwarf galaxy, which also showed signs of tidal disruption (Ibata et al., 1994; Gómez-Flechoso et al., 1999), a vast amount of discoveries started mapping out the tidal debris left behind on its orbit around the Milky Way. In the following years parts of the stream could be found south of the satellite (Mateo, 1998; Majewski et al., 1999), and later also in the northern part of the halo large overdensities were discovered starting with RR Lyrae and BHB stars in the SDSS (Ivezić et al., 2000; Yanny et al., 2000, see also Figure 2.1 for the appearance of the stream in main sequence stars, Belokurov et al., 2006a), many other detections followed. The association of these overdensities with the Sagittarius dwarf was probed with a number of modelling attempts (Johnston et al., 1999; Helmi & White, 2001)¹. With the Two Micron All Sky Survey (2MASS) the stream was observed in M giants over the full circle (Majewski et al., 2003). Over the last years the stream was studied in more and more detail (e.g., Vivas et al., 2001; Newberg et al., 2002; Martínez-Delgado et al., 2004). In Chapter 4 I present a project for which I studied the stream in the SDSS.

Also a number of other extended structures and overdensities were discovered in the halo. Among the many discoveries are other extended streams like the Monoceros ring (Yanny et al., 2003; Ibata et al., 2003) or the Orphan stream (Belokurov et al., 2007b)

¹In Section 2.4 I will also discuss briefly the aspect of tidal streams as a probe of the gravitational potential.

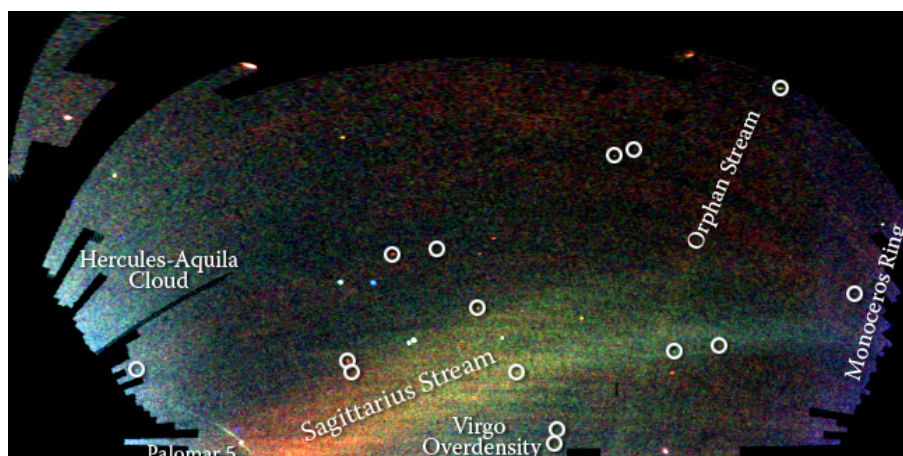


Figure 2.1: Distribution of halo stars in the SDSS field. The colors indicate distances while the intensity is giving the density of the stellar distribution. The circles mark Milky Way companions (globular clusters and dwarf galaxies) which have been discovered by the SDSS. Image credit: V. Belokurov and the SDSS.

and also extended overdensities like the Virgo and Hercules-Aquila overdensities (Duffau et al., 2006; Jurić et al., 2008; Belokurov et al., 2007a), but also narrow streams originating from globular clusters like Palomar 5 (Odenkirchen et al., 2001), showing that globular clusters also add to the halo population.

2.2.1 Formation of Tidal Streams

As already discussed in Chapter 1 satellites captured in the gravitational potential of a large galaxy such as our Milky Way experience strong tidal forces causing the stars in the outer layers of the satellite to become unbound and dynamical friction which is causing the orbit to spiral towards the center of the Galaxy. This force is proportional to the square of the mass of the satellite remnant. Looking at the combination of these two effects implies that the state of disruption a satellite is in when falling into the Galactic Center depends on the initial mass of the system. The more massive a satellite the quicker it will spiral in. Thus, massive systems may still have a remaining core when they reach the Galactic Center while less massive objects will dissolve completely before that. The length of time a system takes for getting disrupted is also determined by the compactness of the satellite.

The typical orbits of captured satellites have high ellipticities. In these orbits the tidal forces have a strong peak around the pericentre. So mostly the stars get stripped on the pericentric passage. Once the stars got unbound from the satellite they continue to move along an orbit similar to the orbit of the satellite at the time they got stripped. Depending

on which side of the satellite these stars are originating from, their orbital periods vary from that of the satellite. Stars from the leading side of the satellite will have shorter periods. This will cause the leading tail to be closer in and the trailing tail to be further out than the orbital path of the remnant.

The mass, and therefore the gravitational potential, of the satellite itself also has a large influence on the shape of the tidal tails as the combined effect with the host galaxy's potential can result in strongly asymmetric forces on the two sides of the satellite and large differences in the tails from the orbit of the satellite (e.g. Choi et al., 2007).

Tidal tails are giving important insights mainly in two respects. First, they document accretion processes in the Milky Way and other large galaxies. We can approach to understand the mechanisms for building up a stellar halo as we see it today by studying satellites in various stages of the disruption process. Second, the extended stellar streams we see around the Milky Way allow us to reconstruct the orbits of individual satellites which will increase our understanding of the shape of the gravitational potential and the distribution of mass in the Milky Way (e.g. Johnston et al., 1999; Helmi, 2004a; Law et al., 2005; Fellhauer et al., 2006; Koposov et al., 2009; Law & Majewski, 2010b; Peñarrubia et al., 2010a; Jin & Lynden-Bell, 2007; Binney, 2008., see also Section 2.4).

2.2.2 Dwarf Galaxies Companions

In recent years a growing number of dwarf galaxies has been discovered around the Milky Way (e.g., Willman et al., 2005; Zucker et al., 2006; Grillmair, 2006, 2009; Belokurov et al., 2007c, 2009) and M31 (e.g., Majewski et al., 2007; Martin et al., 2009), also pushing down the lower limits of galaxy luminosities known to date. This field experienced a wealth of new discoveries in the last years triggered mainly by the SDSS which provided sufficient depth and sky coverage. By considering the limitations of the available depth and sky coverage the numbers hidden in the so far unprobed volume around the Galaxy can be extrapolated revealing that there probably is a large number of satellites around the Milky Way matching much closer the predictions of cosmological models than the number of known satellites just a few years ago suggested (Koposov et al., 2008; Tollerud et al., 2008; Walsh et al., 2009).

Typically these dwarf galaxies are low-metallicity gas-poor systems which have a high dark matter to luminosity ratio ($M/L > 100$) as can be found through the kinematics of

2.2 Development of the Current Formation Picture

these systems. The ultra-faint dwarfs with luminosities of about $10^3 - 10^4 L_{\odot}$ are found to be the most metal poor stellar systems known (Kirby et al., 2008; Geha et al., 2009) show an extreme dominance of dark matter (Martin et al., 2007; Simon & Geha, 2007; Strigari et al., 2008). This makes them interesting as probes of cosmological models and star formation in halos as they represent the smallest dark matter halos known to host stars. Therefore, the dwarf galaxy population provides important hints towards the questions how star formation efficiency in dark matter halos depends on the mass of the halo and if there is a limit below which star formation is strongly suppressed. Interestingly, the dwarf spheroidals found around the Milky Way show a similar dark matter halo mass of about $10^7 M_{\odot}$ in the inner 300 pc (Strigari et al., 2008) with only a small variation compared to the large range they span in luminosity and also no visible trend between the halo mass and the luminosity. This could either hint towards a lower mass limit for star formation or towards a lower limit for the mass of dark matter halos themselves, which could provide information about the properties of dark matter particles. These high dark matter ratios at the faint end of the known satellites also implies that even quite massive dark matter halos are difficult to detect as their stellar content represents only a very faint overdensity against the background.

2.2.3 Characterization of the Halo as a Whole

But besides a growing number of tidal stream detections also efforts were made to characterize the halo as a whole and evaluating to which extent the stellar halo could have formed out of these merger events. In the currently favored cosmological model predicts a large number of subhalos around the large halos of major galaxies. In contrast to this prediction the number of luminous satellites observed around the Milky Way has been fairly low. Bullock et al. (2001) looked into a solution of this so-called missing satellite problem by simulating the accretion of these subhalos onto the Milky Way. This way the model suggested a solution for this discrepancy with the cosmological theory and also reproduced substructures in the halo as been detected in the early SDSS data. Bell et al. (2008) quantified the deviations from a smooth density distribution using the rms of the data around the smooth oblate or triaxial model profile showing by comparison with models (Bullock & Johnston, 2005) that the level of observed substructures is quantitatively consistent with a build-up entirely out of disrupted satellites. Also these models follow the prediction of the current cosmological model by building the halo through the accretion of about 100–200 luminous satellite galaxies. However, they

find that the majority of the mass in the halo comes from the about 15 most massive accreted satellites. Recently, Xue et al. (2010) studied the statistical properties of BHB stars which have similar positions on the sky and found that these tend to have more similar distances and radial velocities compared to a random sampling. Also this study showed consistency with a pure accretion origin.

2.3 Stellar Halos and Tail Tails Around Other Disk Galaxies

Due to the low surface brightness of stellar halos the detection and exploration of the halos around other galaxies is challenging and is therefore naturally limited to the rather local universe. Nevertheless also around the Andromeda galaxy a giant stellar stream could be found (Ibata et al., 2001a). In recent years the stellar halo of the Andromeda galaxy was studied in great detail, especially with the Pan-Andromeda Archaeological Survey (PAndAS, see e.g., McConnachie et al., 2009, and also Figure 2.3) revealing a number of dwarfs (e.g., Martin et al., 2009; Richardson et al., 2011; Brasseur et al., 2011) and tidal debris (Ferguson et al., 2002; Ibata et al., 2007) in its halo.

Also around a growing number of nearby galaxies halos and big streams could be detected (e.g., NGC 891; Mouhcine et al., 2010; NGC 5907; Zheng et al., 1999; Martínez-Delgado et al., 2008). Martínez-Delgado et al. (2010) presented pilot survey starting a systematic search for stellar tidal stream around disk galaxies. Already in this set of eight galaxies a large variety of halo features can be seen (see Figure 2.4). These observations can be used as input for cosmological models reconstructing the formation history of typical disk galaxies. This shows that the build-up of a stellar halo through accretion of satellite galaxies is a common phenomenon.

The external view on other galaxies comes with some advantages compared to the internal observing position on the Milky Way's stellar halo. It is easier to get a global picture of the halo. But the larger distances and projection effects also generate different challenges. Having information of the composition of a large sample of stellar halos of different galaxies will help the understanding of the formation histories of these components in general as well as possibly the interpretation of observations in our own system.

Also the question arises to which extent we see similarities and differences between the detailed formation histories of the different galaxies. For example, the Andromeda

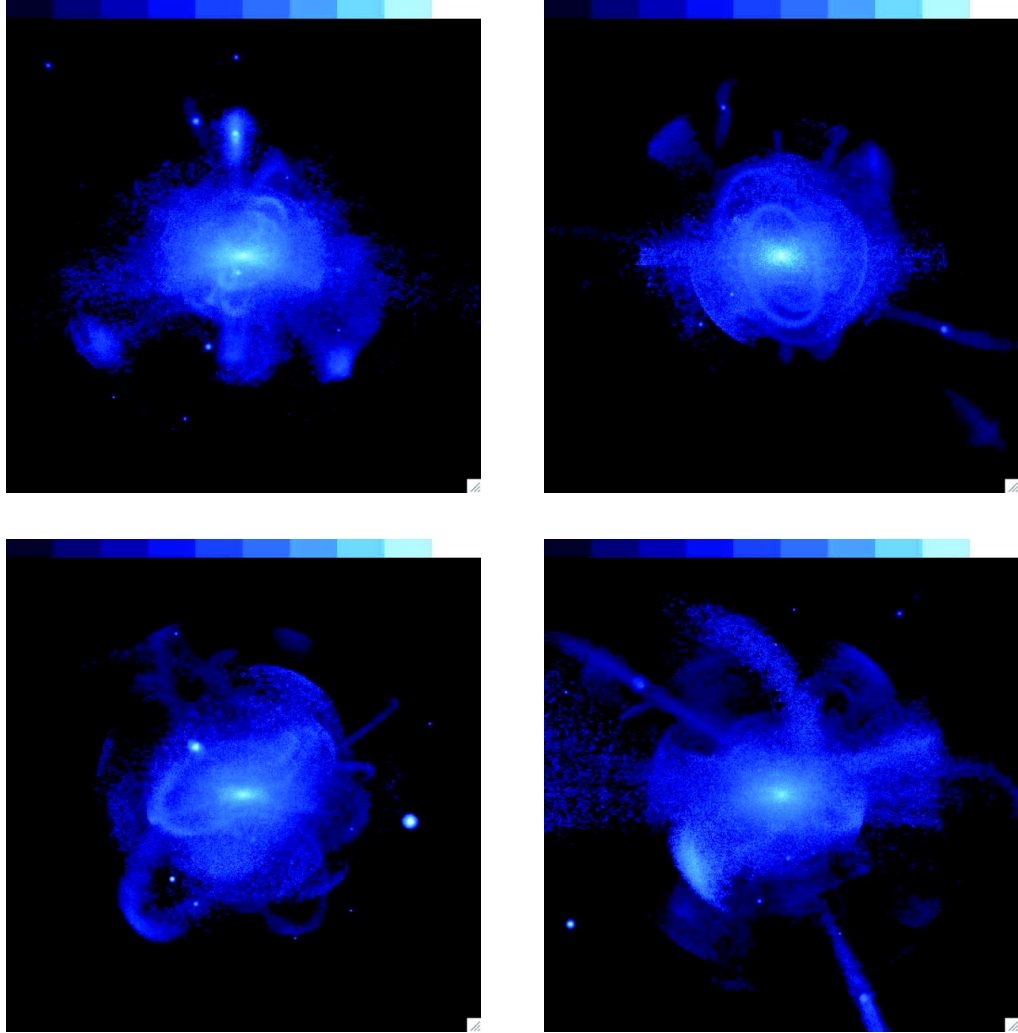


Figure 2.2: Models of a halo composed by disrupted satellites from Bullock & Johnston (2005). External view of the halo of four different realizations. Each panel is 300 kpc on the sides. The color scale reflects the surface brightness. The halo in the lower right recently experienced the accretion of a satellite.

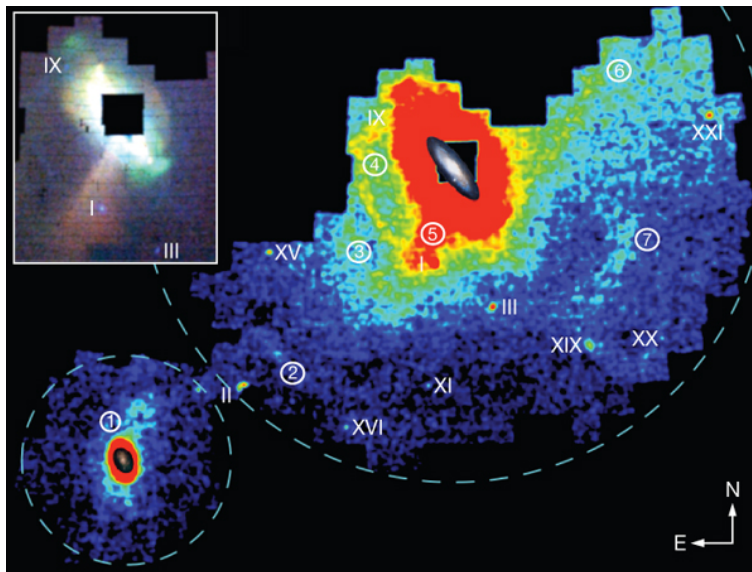


Figure 2.3: The density distribution of stars around the Andromeda galaxies as seen in the PAndAS survey. In the inset panel the central parts of the survey are shown in higher resolution. The roman numbers indicate dwarf galaxies, the numbers in circles point out the most obvious substructures that can be seen in this image. Image credit: McConnachie et al. (2009)

galaxy shows indications of a more active merger history in its recent past compared to the Milky Way.

2.4 Stellar Streams as Probes of the Potential

A good theoretical understanding of the mechanisms which influence the disruption process of satellites makes it possible to use the tidal streams as tracers of the host galaxy's potential. In particular the Sagittarius stellar stream as the largest tidal stream in the Milky Way's halo is widely used to determine the gravitational potential. Despite of a large number of theoretical modelling attempts of the formation of the stream, so far no model could reproduce the whole range of observational data.

Depending on the observational aspect of the stream modelling attempts came to different conclusions. Helmi & White (1999) showed that in non-spherical potentials precession of the orbit will cause a thickening of the stream over multiple orbits, whereas in a spherical potential the stream would follow a great circle on the sky. Following this argument Ibata et al. (2001b) and Majewski et al. (2004) argued that the distribution of the debris along a great circle on the sky would not allow for a large discrepancy

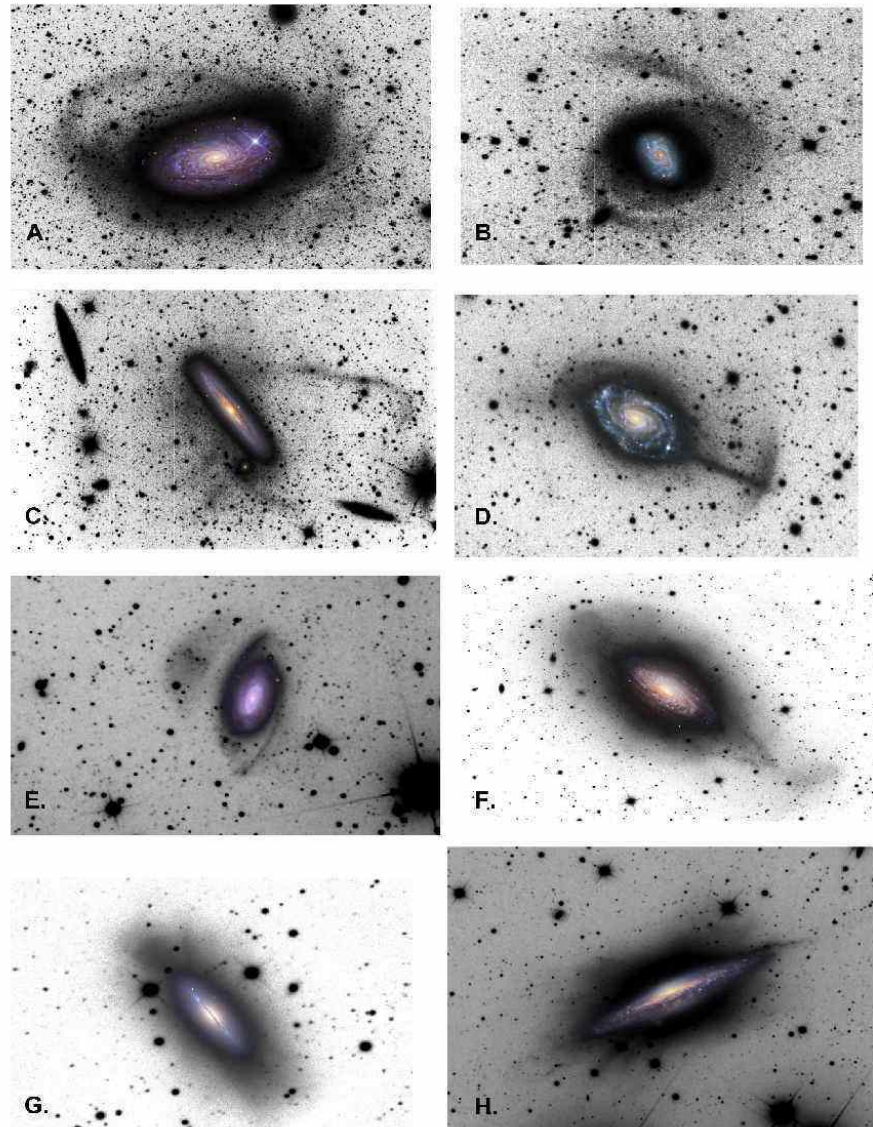


Figure 2.4: Galaxies showing large, diffuse light substructures in their outskirts: (a) a possible Sgr-like stream in Messier 63; (b) giant plumes around NGC 1084; (c) partial tidally disrupted satellites in NGC 4216; (d) an umbrella shaped tidal debris structure in NGC 4651; (e) an enormous stellar cloud in NGC 7531; (f) diffuse, large-scale and more coherent features around NGC 3521; (g) a prominent spike and giant wedge-shaped structure seen emanating from NGC 5866; and (h) a strange inner halo in NGC 1055, sprinkled with several spikes of debris. Each panel displays a (linear) super-stretched contrast version of the total image. A color inset of the disk of each galaxy (obtained from data from the same telescope as the luminance images) has been over plotted for reference purposes. In addition, some of the original images were also cropped to better show the most interesting regions around each target. Image taken from Martínez-Delgado et al. (2010).

Chapter 2 Introduction - The Stellar Halo

from a spherical shape of the dark matter halo. Helmi (2004a) found that this observation would not speak against flattened (oblate) or elongated (prolate) halo shapes² if the debris was lost over multiple orbits of the satellite. Intrinsic properties are another important influence in the thickness of the stream and also the detailed distribution of mass in the halo can contribute to the thickening. Hence, the contributions of precession and other factors to the thickening of the stream is not straight-forward to disentangle. Johnston et al. (2005) are using the orbit alignment of the stream to measure the halo shape and find a slightly flattened halo to be the preferred solution. Recently, also triaxial halo shapes were considered (Law & Majewski, 2010b; Peñarrubia et al., 2010a), also including a reconsideration of the initial properties of the satellite progenitor.

The controversial results arising from models based on the Sagittarius dwarf galaxy and its stream indicates the necessity of a more precise determination of the streams properties. In chapter 4 I present a study of the Sagittarius stellar stream in BHB stars as it can be observed in the SDSS with the goal to determine more precise measurements for the streams properties.

²Most models assume a halo shape which is axisymmetric in the disk plane and vary only the axis perpendicular to the disk to introduce a flattening or elongation. These shapes are also referred to as oblate for a shorter z-axis and prolate for a longer z-axis. Models using triaxial halo shapes also allow the two axes within the disk plane to be different from each other.

SEARCH FOR STELLAR STREAMS IN THE MILKY WAY HALO

IN THIS CHAPTER I describe the basic ingredients and techniques used in this thesis for studying structure in the stellar halo. Two things are critical for this kind of study. The first one is a dataset with a large sky coverage, for which I here use the Sloan Digital Sky Survey (SDSS). The second is an accurate standard candle to study the halo in all three spatial dimensions. For this I use blue horizontal branch (BHB) stars, which have well determined distances and have the additional advantage that they are relatively bright which allows to probe the halo out to large distances.

3.1 The Sloan Digital Sky Survey

For this study I use Data Release 7 (Abazajian et al., 2009) of the Sloan Digital Sky Survey (SDSS) to probe the stellar halo of the Milky Way with BHB stars. Started in 2000, the SDSS is an imaging and spectroscopic survey conducted with a dedicated 2.5m telescope located at the Apache Point Observatory in New Mexico that has so far mapped a little over $\sim 1/4$ of the sky mainly covering area around the North Galactic Pole, providing excellent coverage of the stellar halo in the 'northern' galactic hemisphere. Imaging data are produced simultaneously in five photometric bands, namely u , g , r , i , and z (Fukugita et al., 1996; Gunn et al., 1998; Hogg et al., 2001; Gunn et al., 2006) through drift scan mode. The data are processed through pipelines to measure photometric and astrometric properties (Lupton et al., 1999; Stoughton et al., 2002; Smith et al., 2002; Pier et al., 2003; Ivezić et al., 2004; Tucker et al., 2006) and to select targets for spectroscopic follow-up (Blanton et al., 2003b; Strauss et al., 2002). The photometric uniformity is approximately 2% in r and $g-r$ and 3% in $u-g$. The average magnitude limits are 22.0 mag in u and 22.2 mag in g and r .

3.2 Blue Horizontal Branch Stars

The blue horizontal branch is populated by stars which evolved past their red giant stage and are now burning helium in their cores and a hydrogen-burning shell. It represents the helium-burning equivalent of the hydrogen-burning main-sequence. In general they have thin hydrogen envelopes. The position of the stars on the horizontal branch is determined by its detailed properties. Among others, like age or helium abundance (e.g., Catelan, 2009), metallicity is an important parameter in the sense that there is a tendency for metal-poor stars to be found on the blue side. The thickness of the hydrogen envelope is also affecting the color since the helium-burning temperature is higher compared to hydrogen-burning. It appears that the mass of the helium cores was the same for all stars when the helium flash happened, because that determines the central temperature, but the total mass of the stars on the blue end is smaller than on the red. Blue horizontal branch stars have a mass of around $0.55 M_{\odot}$.

BHB stars have the dual advantages of a high luminosity (allowing probing of the Milky Way halo to > 100 kpc), and have a small intrinsic spread in absolute magnitudes. Their main disadvantage is that the selection of a clean sample of BHB stars is challenging from photometry alone. While broad cuts in $u-g$ and $g-r$ are sufficient to isolate BHB stars and other A-type stars (expected to be blue straggler stars; Preston & Sneden, 2000, Sirko et al., 2004) from low-redshift quasars and white dwarfs, distinguishing BHB stars from the blue straggler contaminants is considerably more challenging (e.g., Kinman et al., 1994; Wilhelm et al., 1999; Clewley et al., 2002; Sirko et al., 2004; Kinman et al., 2007; Xue et al., 2008; Smith et al., 2010). Previous works have used broad color cuts designed to mitigate this contamination (Yanny et al., 2009 and Niederste-Ostholt et al., 2010 used the selection in Fig. 10 of Yanny et al., 2000; Sirko et al., 2004 used a different cut for their faint sample of BHB candidates). Yet, these methods all suffer from very substantial contamination from blue stragglers.

Blue straggler stars are commonly found in globular clusters, dwarf galaxies and the stellar halo (e.g., Sandage, 1953; Bellazzini et al., 2006; Preston & Sneden, 2000; Carney et al., 2001). They raised attention through their odd position in the color-magnitude diagram of the globular cluster M3 (Sandage, 1953). In a globular clusters stars are expected to have similar age and therefore build a well-defined locus in the CMD, with a clear main sequence turn-off corresponding to the age of the stars in the cluster. However, there were stars found with bluer colors and higher luminosities than the main sequence turn-off - they appear to be more massive main sequence stars (not expected

in a single age cluster) and were denoted blue stragglers. This indicated a somewhat peculiar formation mechanism to explain the much higher masses of these stars compared to the other cluster members. The favored mechanisms are proposing the formation of these stars through mass transfer in binary or even triple star systems (McCrea, 1964; Perets & Fabrycky, 2009) or star collisions in dense environments resulting in the formation of a high mass star (Hills & Day, 1976).

Since BHB stars are astrophysically interesting, but photometry alone is not sufficient for a clean selection, SDSS devoted some portion of their fibers to spectroscopy of BHB star candidates. These stars were chosen to have particular properties in color-color space, but the selection criteria changed as the survey progressed and the sample used in this thesis does not have uniform area coverage. Nonetheless, these spectroscopically identified BHB stars are useful for calibrating a new photometric method, with which I can make use of the larger and much more uniform coverage of the photometric survey, and for tracing kinematics. In the following I will introduce first a selection method based on spectroscopy and then how the knowledge gained from the spectroscopic selection about the photometric properties of BHB stars can be used for improving the photometric selection.

3.2.1 Spectroscopic Classification

Due to the composition of BHB stars it is possible to distinguish them with high confidence from other stars which are located in the same area of the color–magnitude diagram through the examination of spectra. A detailed analysis of the shapes of the spectral lines, especially the Balmer lines, is necessary for that. In this thesis I use a method developed by Sirko et al. (2004) and Xue et al. (2008). In the following I will give a description of the basic steps of the spectroscopic selection performed by Xue et al. (2008).

The first selection step is actually a photometric criteria limiting the following analysis to stars in a color-color range of $0.8 < u-g < 1.6$ and $-0.5 < g-r < 0.0$ adapted from Yanny et al. (2000, see also Figure 3.1).

The following selection steps take advantage of the effects of surface gravity and temperature on the stellar spectrum, more precisely on the Balmer line profiles. Within a selected temperature range resulting from the color cuts, BHB stars show a lower surface gravity than BS stars and a higher temperature than found in old MS stars as

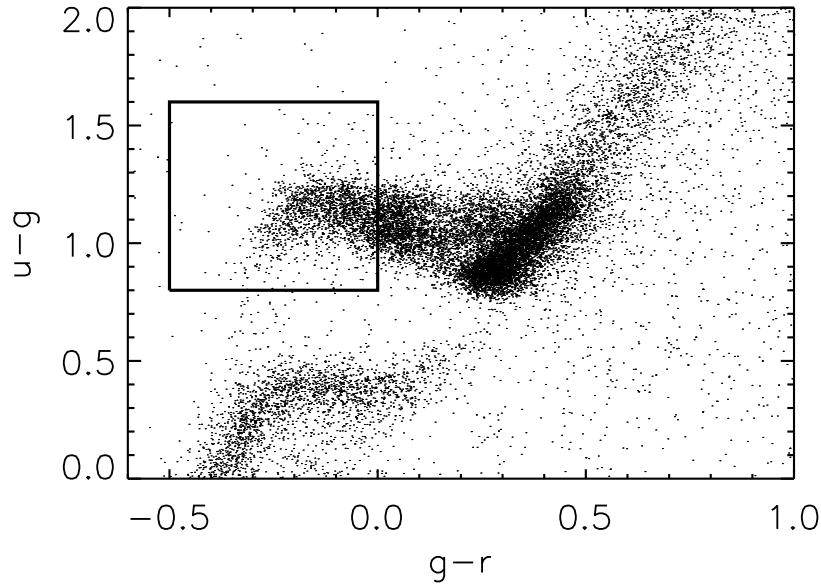


Figure 3.1: SDSS DR6 color-color diagram of all stars with spectra. The selection box for BHB star candidates is based on Yanny et al. (2000). Image taken from Xue et al. (2008).

present in the halo. These properties are getting utilized through an analysis of the Balmer line profiles in two independent selection methods in order to separate BHB stars from other stellar populations as cleanly as possible.

The first method separates BHB stars from BS stars using the width of the Balmer line at a flux value of 80% of the local continuum, $D_{0.2}$, and the flux of the minimum of the line relative to the continuum, f_m (see Figure 3.2). This method, called the $D_{0.2}$ vs. f_m method (Pier, 1983; Sommer-Larsen & Christensen, 1986; Arnold & Gilmore, 1992; Flynn et al., 1994; Kinman et al., 1994; Wilhelm et al., 1999), discriminates BHB stars from BS through the line width, since the lower surface gravity on BHB stars results in narrower Balmer lines than on the smaller BS stars (see Figure 3.3), and from MS stars through the flux at the minimum (Beers et al., 1992; Sirko et al., 2004), where cooler stars show higher flux values corresponding to weaker lines. Figure 3.4 shows all stars within the color-color box illustrating the severe amount of contamination in the color-selected sample. It is estimated to be of the order of 50%. The criteria for confirmation as a BHB star from this method are:

$$17 \leq D_{0.2} \leq 28.5, 0.1 \leq f_m \leq 0.3.$$

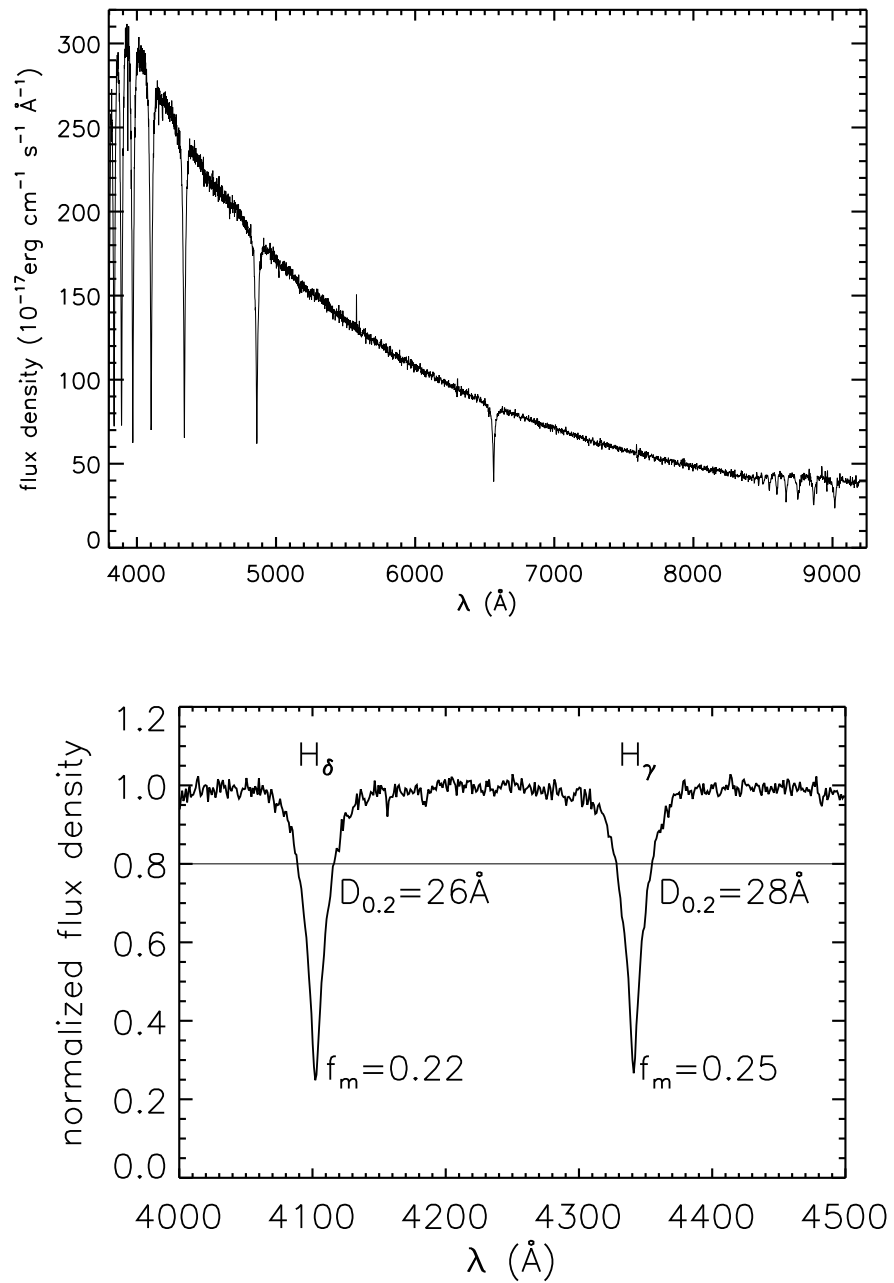


Figure 3.2: Typical spectrum of a high-S/N BHB star. The lower panel shows a blow-up on two Balmer lines. In this plot the continuum is normalized and the two parameters $D_{0.2}$ and f_m are indicated. Image taken from Xue et al. (2008).

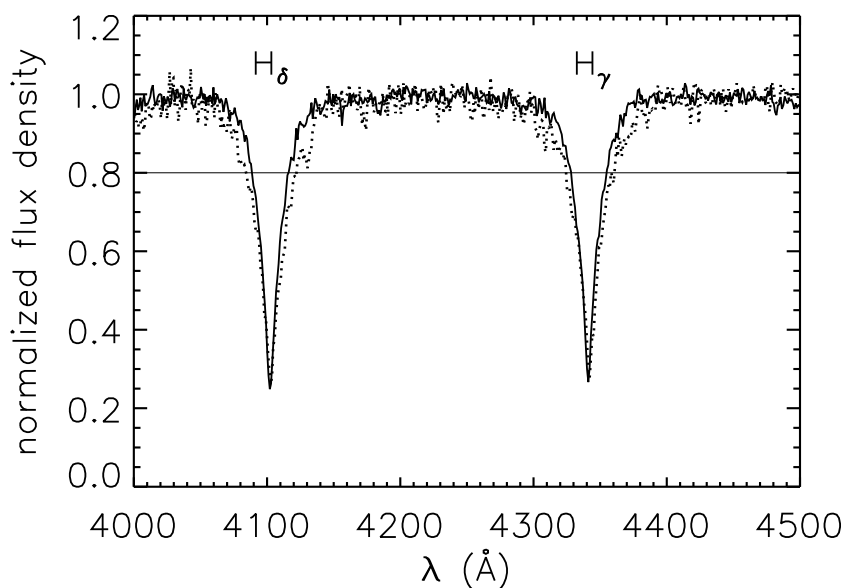


Figure 3.3: Comparison between normalized BHB star (solid) and BS star (dotted) spectra. Due to the higher surface gravity of BS stars their Balmer lines are wider around 20% below the local continuum than those of BHB stars. Image taken from Xue et al. (2008).

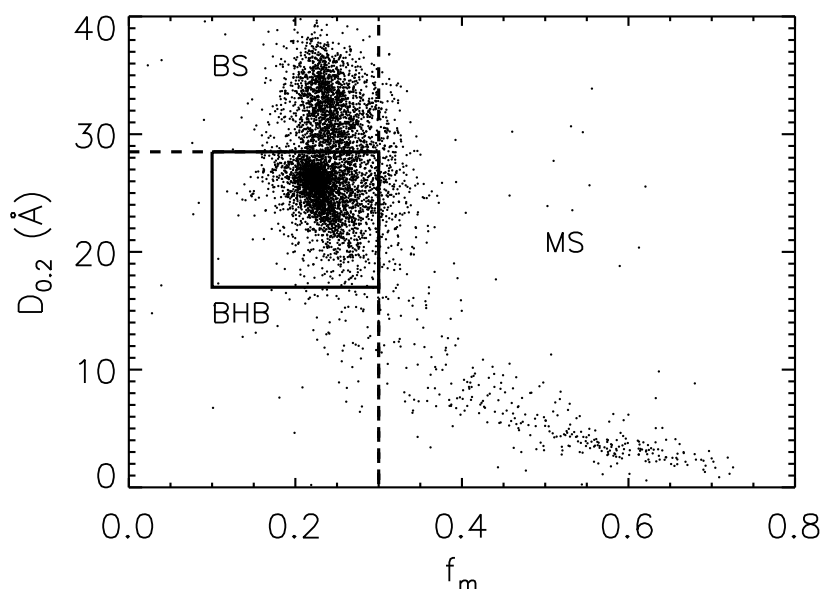


Figure 3.4: Illustration of the selection resulting from the f_m vs. $D_{0.2}$ method. The f_m parameter, representing the depth of the line, is giving a measure of the temperature; the stars to the right of the vertical line are too cool for BHB stars. The width of the lines, $D_{0.2}$, is influenced by the surface gravity. Above the box are the higher surface gravity BS stars. The box represents the acceptance criteria of this method. Image taken from Xue et al. (2008).

The second method called scale width vs. shape method (Clewley et al., 2002) is based on a Sérsic profile (Sérsic, 1968) fit to the Balmer lines. The normalized flux density y to a Balmer line at the nominal wavelength λ_0 is given by:

$$y = n - a \exp \left[- \left(\frac{|\lambda - \lambda_0|}{b} \right)^c \right], \quad (3.1)$$

with the five free parameters : a, b, c, λ_0 and n . The parameter n should account for small corrections in the radial velocity and normalization of the spectrum. The parameter a has only a small variability for a given line.

The stars which got selected through the color cuts are shown in Figure 3.5. They separate quite clearly into two distinct areas in the c_γ versus b_γ plane (with γ referring to the H_γ line), with the upper branch hosting the BS stars and the lower one the BHB stars. The parameter c also gives a measure of the temperature as cooler stars show smaller values. The color coding indicated the earlier selection based on the $D_{0.2}$ vs. f_m method, showing that this first selection already generated a good separation. The applied selection criteria in this second selection are:

$$0.75 \leq c_\gamma \leq 1.25$$

$$7.5 \leq b_\gamma \leq 10.8 - 26.5 (c_\gamma - 1.08)^2 .$$

Through the first spectroscopic selection about 50% of the color selected sample gets rejected, going down to 30% after the second criterium. The remaining contamination is estimated to be $\lesssim 10\%$, implying a contamination of about 50% after the first spectroscopic selection. Note that this selection was not optimized for completeness, but for purity.

3.2.2 Photometric Classification

Although a selection based on photometric information alone can not be as precise as a spectroscopic selection, this is still important to look into given that the SDSS, as most surveys, is providing spectra only for a very limited number of stars compared to the full size of the survey. As this is an issue which will remain relevant also for future surveys, it is important to have a selection which is not limiting the sample size and also introduces the selection effects of the spectra targeting strategy on the sample.

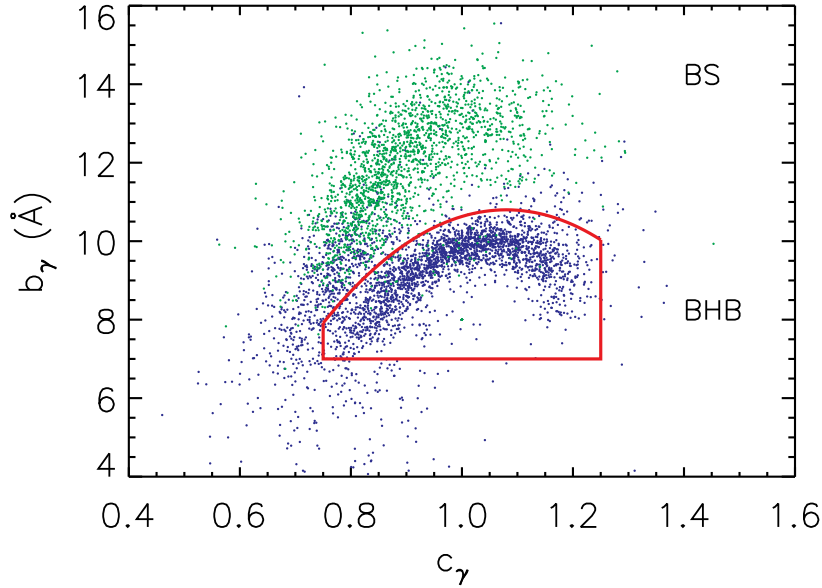


Figure 3.5: As the distribution of BHB (blue dots) and BS (green dots) star as selected with the f_m vs. $D_{0.2}$ method is showing this first selection already follows the bimodality in the b_γ vs. c_γ quite cleanly. The enclosed region represents the second selection criterium. Image taken from Xue et al. (2008).

Therefore I apply a selection based on photometric data alone which incorporated the experience on photometric properties of BHB stars gained through the spectroscopic selection. This method was developed by Bell et al. (2010).

The spectroscopic classifications of $m_g < 18$ stars from Xue et al. (2008) is used as a training set. The probability of a star in the color box $0.8 < u - g < 1.6$ and $-0.5 < g - r < 0.0$ being a BHB star from this training set is calculated (Fig. 3.6). Blue data points show stars that are very likely to be BHB stars on the basis of their spectra (a contamination of much less than 10% has been argued by Xue et al., 2008 and Sirko et al., 2004 for $m_g < 18$). Within the color box BHB stars are largely outnumbered by other blue stars (mainly BS stars). For the full spectroscopic sample with $m_g \lesssim 19.5$ the BS contamination is about 60%, for the $m_g < 18$ subsample shown in Figure 3.6 the BS to BHB fraction is $\gtrsim 3 : 1$. To reduce the contamination rate the fraction of spectroscopically-classified BHB stars to other stars is derived for a grid of locations covering the color-color space within the box. The thick contour outlines the region with $> 50\%$ and more than 16 stars in a bin of 0.025×0.04 mag. Applying this selection to the SDSS DR7 (Abazajian et al., 2009), a candidate sample with 389785 stars within the $0.8 < u - g < 1.6$, $-0.5 < g - r < 0.0$ color box is obtained. In the follow-

ing a lower probability limit of 50% for the photometric sample is applied reducing the sample size to 28270 stars. The completeness and contamination of the selection was tested both using the spectroscopic sample and BHB star-rich globular clusters. For these tests the ‘> 50%’ subsample was used. For $m_g < 18 \sim 50\%$ of the real BHB star population (taking into account the contamination rates in the spectroscopic selection) were recovered with a contamination of 20–30%. This improves the simple color box selection, which had a contamination of about 60% significantly. Performance at fainter limits is expected to degrade gradually, with increasing incompleteness and contamination. While the selection at $m_g \sim 19$ still recovers 40% and has a contamination of 40% which is still an improvement over the full color box, the selection at $m_g \sim 20$ only recovers roughly 20% with a contamination which may be as severe as 50% (Bell et al., 2010). This means that at this luminosity cut most real BHB stars are thrown out while the contamination is only slightly improved. We will later test the influence of changing the probability cuts (and therefore completeness/contamination) in Section 4.3.1.

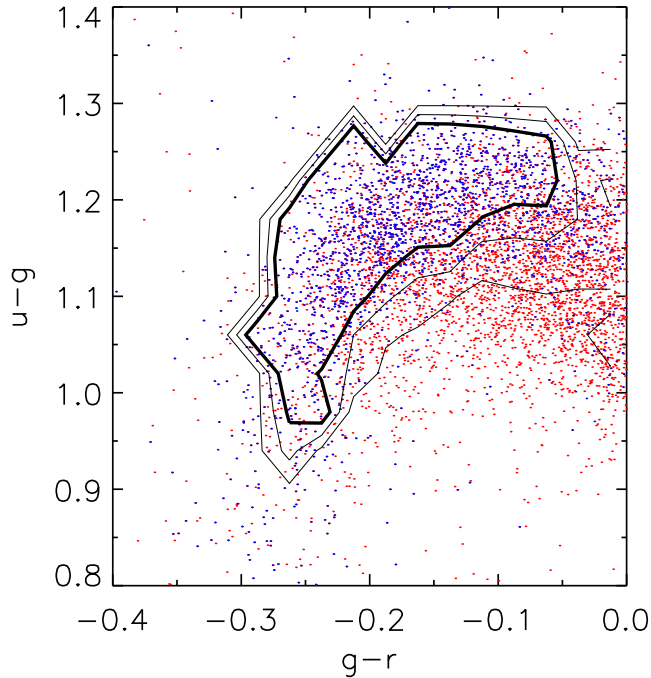


Figure 3.6: Photometric BHB star selection. All candidate BHB stars shown have with spectroscopic classification (following Xue et al., 2008). Stars spectrally classified as BHB stars are shown in blue; other stars are shown in red. Contours show regions in $(u-g)$ vs. $(g-r)$ space where the fraction of targets classified as BHB stars exceeds 10%, 30% and 50%, respectively; the 50% contour is thicker than the others. In what follows I focus primarily on BHB star candidates whose colors fall within the 50% contour.

3.2.3 Empirical Distance Uncertainties

As distance precision for the BHBs plays an important role for our analysis, I use several known globular clusters and dwarf spheroidals to determine both the statistical and systematic uncertainties of the distance determination¹. A color-magnitude diagram (CMD) for one of the dwarf spheroidals is shown in Figure 3.7. The typical shape of the blue horizontal branch shows a nearly horizontal part at redder colors and a gradual trend towards fainter magnitudes at the blue end, as can be seen in Figure 3.7. Overall this trend causes an increase in the magnitude spread and therefore distance measurement uncertainties towards bluer colors. The following will be of particular relevance in Chapter 4. As I will show in section 4.3.1, the Sagittarius stellar stream shows a larger concentration of ‘red’ BHB stars. This indicates that studying the red BHB stars separately can have two benefits compared to looking only at the sample as a whole. *i*) The signal strength for the stream will increase, and *ii*) the uncertainties introduced by the deviations from the horizontal shape of the horizontal branch can be reduced.

Therefore, I divide the sample into a blue and a red part for further analysis. The $g-r$ value at which I apply the cut throughout this thesis is illustrated in Figure 3.7 by the vertical line. This cut is chosen to divide the bright stars of the sample ($g < 18.5$ mag) in equally populated halves. I determine the statistical error of the distance measurement for BHB stars by measuring the spread of their distance moduli within one cluster (whose line-of-sight extent is negligible). The distance modulus distribution for the objects is shown in Figure 3.8. I fit Gaussians to these distributions and use the standard deviation for estimating the statistical distance uncertainty $\delta D/D$. I measure the mean value and the standard deviation for both the red part and the $> 50\%$ BHB probability sample (see Table 3.1). The distribution in distance modulus of red and blue stars is also shown in Figure 3.8 indicated by the blue and red shaded areas. The results are shown in Table 3.1. The mean statistical distance uncertainty for the objects listed here is 4% for the $> 50\%$ sample and 6% for the full sample.

Comparison with prior distance determinations (see Table 3.1) showed a systematic underestimation of the distances in our results. This effect is of the order of 4% in distance, but also includes some variance which is probably also partly due to the fact that the literature values were determined with different methods.

With this test I can not probe uncertainties in the distance determination that arise

¹The distances were derived using the $g-r$ -dependent M_g calibration from Table 2 of Sirko et al. (2004) with $[\text{Fe}/\text{H}]=-1$ (different by less than the $[\text{Fe}/\text{H}]=-2$ calibration by <0.05 mag).

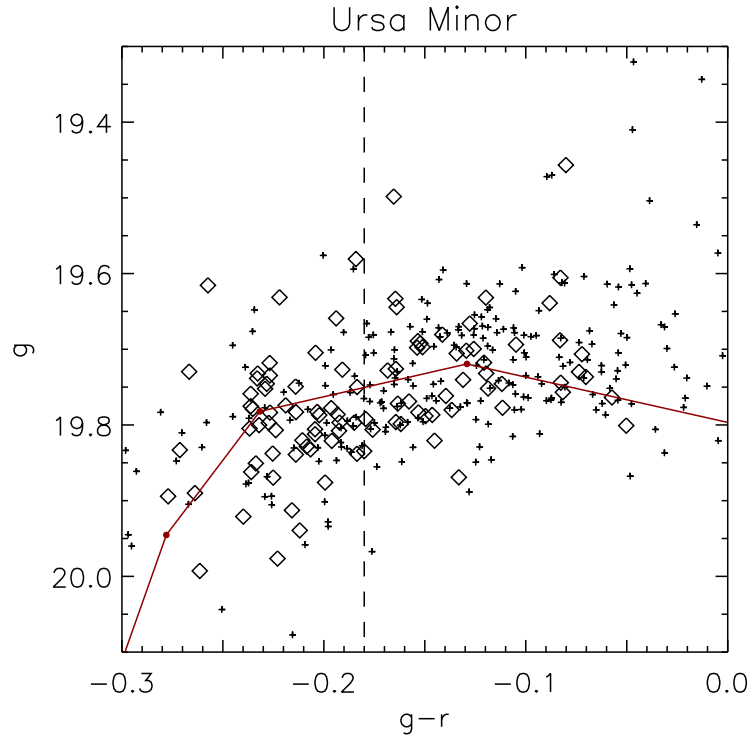


Figure 3.7: The BHB section of the color magnitude diagram for the Ursa Minor dwarf spheroidal galaxy. The diamonds represent the ugr -color selected BHB star candidates with $\geq 50\%$ BHB probability; the rest of the sample with lower probabilities is shown as crosses. It can be clearly seen that there is a trend towards fainter magnitudes for bluer colors; the $g-r$ dependent M_g calibration of Sirko et al. (2004) follows this trend closely (see red line for stars with $\text{Fe}/\text{H} = -1$). The vertical line shows the position of the color cut applied to distinguish between red and blue BHB stars.

from a spread in metallicity. The metallicity-dependent BHB star models of Dotter et al. (2007) and Dotter et al. (2008) indicate a significant contribution to the distance uncertainties by a range of metallicities in the halo BHB stars. The overall uncertainty accounting for a combination of the scatter seen in single metallicity populations and the contribution of a scatter introduced by having a variety of metallicities is estimated to be less than 10% in Bell et al. (2010). In what follows I account only for the uncertainty which was estimated using single metallicity populations, which may underestimate the overall distance uncertainties (5% vs. < 10%).

Density Maps

Having good estimates for both the probability in having selected an actual BHB star and the uncertainty in the distance determination for BHB stars this information can be used to create BHB star maps, giving a probability weighted picture of the distribution of BHB stars in the halo.

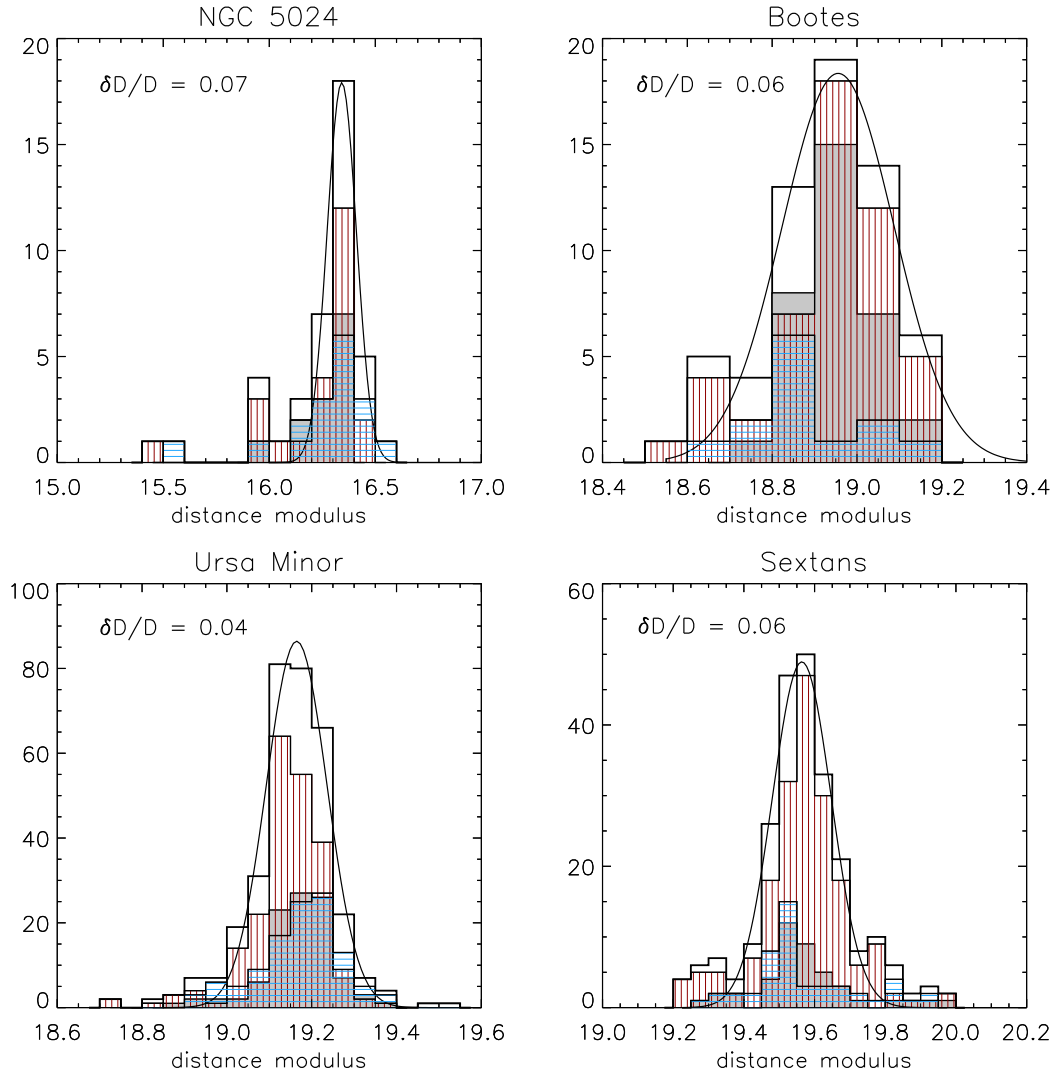


Figure 3.8: Distance accuracy for individual BHB stars. The panels show the distance modulus distribution of photometrically selected SDSS BHB stars in four clusters and dwarf spheroidal galaxies. For each object, a Gaussian is fitted to the full sample (unfilled histogram) to measure the width of the distribution as an estimate of the distance uncertainty. The gray histogram shows only the stars with a BHB probability greater than 50% (Fig. 3.6), the ones filled with vertical red and horizontal blue lines give the distribution for the red and the blue part of the horizontal branch, respectively. Clearly these clusters have a larger concentration of red BHB stars. Results of the fit to both the $> 50\%$ BHB probability sample and the red part are shown in table 3.1. The statistical distance uncertainty $\delta D/D$ resulting from the fits to the full sample are also given in the plots, being a bit higher for the full sample and a bit lower for the $> 50\%$ sample than the expected value of $\delta D/D \sim 0.05$ (Sirko et al., 2004).

3.2 Blue Horizontal Branch Stars

Object	$\langle m-M \rangle_{prob>0.5}$ (mag)	$\sigma_{prob>0.5}$ (mag)	$\langle m-M \rangle_{red}$ (mag)	σ_{red} (mag)	Literature Values (mag)	$\delta D/D$	Rel. Dist. Offset
NGC 5024	16.26	0.09	16.27	0.14	16.31 ^a	0.04	0.02
Bootes	18.95	0.08	18.95	0.12	18.94 ± 0.14^b	0.04	0.01
Ursa Minor	19.17	0.07	19.15	0.07	19.32 ± 0.12^c	0.03	0.07
Sextans	19.56	0.12	19.57	0.11	19.75 ± 0.13^d	0.05	0.06

Table 3.1: Distances to clusters and dwarf spheroidals: Mean and standard deviation in distance modulus for four clusters and dwarf galaxies given for a subsample with a BHB star probability $> 50\%$ and for the red BHB stars only. The second to last column gives the inferred distance uncertainty $\delta D/D$ for the $> 50\%$ sample of the color-selected BHB stars. The mean value is 0.04, which is a bit lower than the mean value of the full sample of 0.06. As literature values I give the mean values and standard deviations from a number of studies as listed. In the last column, the relative distance offset is given which was calculated using the literature values listed in the table.

^a Harris (1996);

^b Belokurov et al. (2006b); Dall’Ora et al. (2006); Siegel (2006); de Jong et al. (2008);

^c Mighell & Burke (1999); Bellazzini et al. (2002); Carrera et al. (2002); Tammann et al. (2008);

^d Mateo et al. (1995); Lee et al. (2003); Tammann et al. (2008).

I then create maps to visualize the BHB star density, that account both for the finite probability that stars are BHB stars (as described in §3.2.2) and for the distance uncertainties. I account for the distance uncertainty by viewing each star as an ensemble of 100 sub-objects, with line-of-sight distances drawn from a Gaussian distribution with 5% scatter (see section 3.2.3) around the mean of the distance estimate for each individual BHB star. These sub-objects, each of which has a probability of 1%, is then multiplied by the probability it has to be a BHB star. A map is then created by dividing the plane into cells for which the probabilities of the included stars are summed. The ‘signal’ therefore depends on both spatial abundance of stars and on probability of each to be a BHB star. These maps then get convolved with a Gaussian kernel for presentation purposes.

3.3 Coordinate Transformations

Having identified a stellar population which provides accurate distance information the full three dimensional positions of these stars can be derived. Knowing the positions of these stars in the survey volume is clearly important for finding and studying structures, but it is not obvious how to proceed from here. For practical reasons it seems to be reasonable to bin the volume into slices (of whatever shape seems appropriate) and collapse these bins into two dimensional representations. The three dimensional positions allow to freely choose these bins in whatever way might be useful for the task. One has to keep in mind, though, that although we have information on all three spatial dimensions the accuracy is not the same of all of these. While I claimed the distances to be very well determined, this is only true compared to other popular standard candles. Compared to the positions on the sky the distances have clearly by far the largest uncertainty of all spatial dimensions. Since the direction to the Sun, giving the direction of the dominating uncertainty, is not easily recognizable in every projection, it is important to keep track of this direction to understand the overall uncertainties on the positions of the stars. Here, this is done by smearing out the signal of each star over the line-of-sight as explained in Section 3.2.3. While there are advantages and disadvantages to many possible presentations, I want to go through the seemingly most useful possibilities here.

Spherical Galactic Coordinate System

To study the system of the Milky Way galaxy it is more natural to leave the most commonly used equatorial coordinate system behind and use a system which is based on the Galaxy itself. The equatorial system is based on the rotation of the earth. It projects a coordinate grid on the sky, which is in principle the same as the longitude-latitude system on for the surface of the earth. On the sky the two dimension are described by the right ascension and declination. For most applications this is a sensible definition of coordinates. However to describe structures and motions in the Milky Way system it is more natural to change to a coordinate system which is orientated on the disk and the poles of the Galaxy rather than the poles and equator of earth. This so called Spherical Galactic Coordinate system is using a Galactic longitude and latitude to describe positions. In this system the galactic longitude l describes directions in the plane of the galactic disk and the galactic latitude b perpendicular to that. In this system the Sun is in the center. The Galactic center gets transferred from $\alpha = 17^h45.6^m, \delta = -28^\circ56'.2$ in equatorial coordinates to $b = 0^\circ$ and $l = 0^\circ$.

Heliocentric Distance Shells

Probably the most natural presentation is to show the stars in their positions on the sky. By limiting the distance range of stars shown the halo can be investigated in concentric distance shells. Distance shells (either centered on the Sun or, as introduced later in this chapter, on the Galactic Center) can be potentially useful in detecting overdensities which have a good chance of being consistent with a concentrated object which tidally disrupted on its orbit around the Milky Way. An obvious drawback is that this will introduce a bias towards detection of structures which happen to have equidistant orbit segments in the part of the sky covered by the survey, whereas the largest fraction of highly elliptical orbits are not detectable in this projection. While the Galactocentric version of these distance shells host circular or nearly circular orbits, there is no physical reason to look for structures on shells around the Sun. However, these distance shells show a high potential of substructures by visual inspection. Another advantage of this projection is that it is the least corrupted by transformations so the assumptions put into this are as few as possible. As mentioned earlier the distances give the largest contribution to the position uncertainties. In building heliocentric distance slices this uncertainty only influences in which slice the stars are placed. If the slices are thin compared to the uncertainties this can still be an issue, but when the slices are thick compared to the uncertainties this misplacement gets less severe and become negligible.

Galactocentric Coordinate Systems

Instead of using our natural observing position, the Sun, as the Center, one can also shift the system to be centered on the Galactic center. This has the advantage of showing structures in a system which reflects the dynamics in a better way. This is called the galactocentric coordinate system. For a transformation into this system one has to make an assumption for the distance of the Sun to the Galactic center. I adopt a value of 8 kpc for the distance to the Galactic center in this thesis. We take an intermediate step here by transforming the coordinates into a cartesian system centered on the Galactic Center.

Cartesian Coordinates

For most transformations it will be useful to start from a cartesian coordinate system. Having the equatorial coordinates l and b and the distance to the Sun d_{\odot} of the stars these are derived as

$$z = d_{\odot} \cdot \sin(b \cdot \pi / 180^{\circ}) \quad (3.2)$$

$$x = 8.0 \text{ kpc} - d_{\odot} \cdot \cos(b \cdot \pi / 180^{\circ}) \cdot \cos(l \cdot \pi / 180^{\circ}) \quad (3.3)$$

$$y = d_{\odot} \cdot \cos(b \cdot \pi / 180^{\circ}) \cdot \sin(l \cdot \pi / 180^{\circ}) \quad (3.4)$$

These cartesian coordinates are already shifted by 8 kpc in the x direction to move the center of the coordinate system from the Sun to the Galactic Center. In this system the Galactic plane is in the xy-plane, with the positive x-axis pointing in the direction of the Sun. The z-axis is giving the height above or below the Galactic plane.

Galactocentric Distance Shells Then from the cartesian coordinates we can calculate back into spherical coordinates, to get the equivalent of the heliocentric distance shell, but centered on the Galactic Center:

$$b_{GC} = (180^{\circ} / \pi) \cdot \arcsin(z / d_{GC}) \quad (3.5)$$

$$l_{GC} = \begin{cases} (180^{\circ} / \pi) \cdot \arctan(y/x) + 360^{\circ} & \text{for } x > 0 \text{ and } y \leq 0 \\ (180^{\circ} / \pi) \cdot \arctan(y/x) + 180^{\circ} & \text{for } x \leq 0 \\ (180^{\circ} / \pi) \cdot \arctan(y/x) & \text{otherwise} \end{cases}$$

with the distance to the Galactic center d_{GC} begin defined as $d_{GC} = \sqrt{x^2 + y^2 + z^2}$

Distance shells can be useful in approaches to detect or study structures in the halo like stellar streams. In particular galactocentric distance shells host stellar streams on circular or nearly circular orbits around the Galaxy and segments of streams which happen to have rather constant distances in the observed part of the sky. Even not very strongly elliptical orbits have a good chance of discovery when overdensities in neighboring distance shells are moving along a paths on the sky. Streams on very elongated elliptical orbits are not likely to be discovered with this method. In this projection it gets more important to be aware of the distance uncertainties and their direction, but as the Sun is rather close to the Galactic Center compared with the extent of the stellar halo, the difference between heliocentric and galactocentric distance shells gets very small

when looking at greater distances (compare Figures 3.9 and 3.10, where the distance uncertainties are visualized in the galactocentric shells).

An important step in verifying these as good candidates can be done in taking full advantage of the 3D information and combining different projections. I take advantage of the fact that the orbital plane of every object that is moving under the influence of a gravitational potential should include the center of this potential. In this case, any stream that formed through tidal forces in the Milky Way's gravitational potential should be situated in a plane which includes the Galactic Center. On galactocentric equidistant shells the intersection with such a plane is a great circle. These shells are segments of spheres with the Galactic Center in the center. By selecting any two points on the sphere we can define a great circle. Accordingly, if we place two points in the observed overdensity we can visualize the trace of the great circle on the distance shell and see if this is consistent with the observed overdensity. For heliocentric distance shells in principle the same technique can be applied. Here the intersection with a plane through the Galactic Center is not a great circle on this sphere, but still the trace on the sphere is defined by two points as the third which is necessary to define a plane is already given by the Galactic Center. If the overdensity seen on the distance shells is matched by this intersection line with a plane, that includes the GC, we can apply the next test and investigate the structure in the galactic plane itself.

Galactic Planes Here we can mark either the stars we saw in the overdensity or the whole intersection with a shell to see if what was seen as an overdensity in the distance shell is still visible as an overdensity in the plane. Also in this plane we can test if the overdensity is consistent with an orbit around the Galactic Center. In a non-keplerian potential orbits are in general rosettes instead of ellipses, but as a first approximation one wants also to check that the stream segment looks roughly like an ellipse segment. Depending on the profile of the potential the mismatch between the epicyclic frequency (the frequency of the radial oscillation) and the angular frequency can be as much as a factor of two, leading to a rather large discrepancy from an elliptical orbit. Ultimately one can fit an orbit to the observations.

For building a galactic plane through two stars in an arbitrary structure I use the cross product of the cartesian position vectors of two points within the structure to define a normal vector \vec{n} on the plane. For two stars with the coordinates (x_1, y_1, z_1) and

(x_2, y_2, z_2) :

$$n_x = y_1 \cdot z_2 - z_1 \cdot y_2 \quad (3.6)$$

$$n_y = z_1 \cdot x_2 - x_1 \cdot z_2 \quad (3.7)$$

$$n_z = x_1 \cdot y_2 - y_1 \cdot x_2 \quad (3.8)$$

For changing this vector by small amounts for optimization of the plane, or in general for systematic construction of planes in the survey volume, it can be useful to define the normal vector using a spherical angle system.

$$n_x = \cos(\pi \cdot \vartheta / 180.) \cdot \cos(\pi \cdot \varphi / 180.) \quad (3.9)$$

$$n_y = \cos(\pi \cdot \vartheta / 180.) \cdot \sin(\pi \cdot \varphi / 180.) \quad (3.10)$$

$$n_z = \sin(\pi \cdot \vartheta / 180.) \quad (3.11)$$

with $-90^\circ < \vartheta < +90^\circ$ and $0^\circ < \varphi < +360^\circ$.

The coordinates in the new system where the two stars are located in the xy-plane are then given by

$$x' = \frac{(n_z \cdot x - n_x \cdot z)}{\sqrt{n_x^2 + n_z^2}} \quad (3.12)$$

$$y' = \frac{(-n_x \cdot n_y \cdot x + (n_x^2 + n_z^2) \cdot y - n_y \cdot n_z \cdot z)}{(\sqrt{n_x^2 + n_z^2} \cdot \sqrt{n_x^2 + n_y^2 + n_z^2})} \quad (3.13)$$

$$z' = \frac{(n_x \cdot x + n_y \cdot y + n_z \cdot z)}{\sqrt{n_x^2 + n_y^2 + n_z^2}} \quad (3.14)$$

After this transformation the two selected points are in the xy-plane. To study this plane for structure we need to allow for some thickness in the selection of the stars it contains. This could be done by accepting stars with a certain range of z-values producing two parallel boundary planes and a sample with constant thickness at all distances. Another possibility is to select stars in a wedge by accepting all stars for which the angle between the normal vector and the position vector of the star is differing

from 90° only by a given angle. In this definition the selected volume is getting wider with distance from the center. The later follows more closely the basic idea behind this selection since it is probably more robust towards slight differences to the ‘ideal’ plane through a tidal structure. Also precessing orbits might be easier to capture in a wedge. I apply the wedge selection in this thesis. For the 2D presentations I collapse the stars onto a plane by conserving the distance to the center.

$$x_{plane} = x' \cdot \frac{\sqrt{x'^2 + y'^2 + z'^2}}{\sqrt{x'^2 + y'^2}} \quad (3.15)$$

$$y_{plane} = y' \cdot \frac{\sqrt{x'^2 + y'^2 + z'^2}}{\sqrt{x'^2 + y'^2}} \quad (3.16)$$

As explained earlier I visualize the distance uncertainties of the stars by splitting each star up into 100 sub-objects which are placed at a range of distances drawn from a gaussian distribution around the star’s distance value with a standard deviation which accounts for the distance uncertainty. As this smears out the stellar positions in the direction of the largest uncertainty (the uncertainties of the position perpendicular to the line of sight are small and can be neglected) this technique helps to account for the position uncertainties even in projections where the direction to the Sun is no longer obvious. When cutting out slices of the volume it will happen in many cases that the direction of this uncertainty is pointing outwards of the slice volume. If the stars were just positioned on the most likely distance this would mean that in some cases the stars would end up outside and in other cases inside the selection area. Although this technique might not take care of this problem perfectly it still provides a better solution for this problem. Instead of making a clear yes/no decision the stars leave a fraction of their probability to be in this place inside of the selection area. This very much reflects the actual situation as it is unknown for a star with this position uncertainty if it would be located inside or outside. With this method we simply assign it with a certain probability of being inside the selected volume putting less weight on the stars which have a certain probability of going over the edge. Still, one might want to think about the construction of the wedges in this context since depending on the location of the plane in the volume the thickness of the plane will have a very different ratio to the value of the uncertainty at different parts of the wedge. While the uncertainties are small in the inner parts and the wedge is narrow in these parts as well the increase of the uncertainties is different from the increase in thickness. This will be mostly a problem for the very inner parts of the

Chapter 3 Search for Stellar Streams in the Milky Way Halo

wedge close to the Galactic center. In the following we are mostly looking at structures at distances where this is probably not an issue, but one could think of adjustments in the geometry of the selection to minimize this effect. This could be done e.g. by having a transition to parallel borders in the inner parts.

3.4 Techniques for Finding and Studying Structures

In this section I want to go through some further techniques which can be useful in detecting and studying structures. Partly I will use a stream candidate for illustration.

3.4.1 Structure Search in Distance Slices

The distance shell maps of the SDSS field impressively show a richness of structures. The largest structure in the halo, the Sagittarius stream, can be easily spotted. The same applies to very concentrated objects like clusters and also dwarf galaxies. We can see that the known structures are in general detectable in BHB stars, with some exceptions where BHB stars are too sparse in these structures like the closer part of the Sagittarius stream. It gets much more challenging, though, when looking for small, yet unknown, streams. Since the number of BHB stars is comparably low, e.g. to MSTO stars (the MSTO to BHB star number ratio is about 100:1, e.g., Bell et al., 2010), the grainy appearance of these maps might also trick the eye as the human brain is good at detecting structures. So one has to be careful to not overinterpret this ability to connect dots. Another thing to be aware of is the technique in which the survey was taken. The telescope is operating in drift scan mode, which means that it is taking images of the sky as the rotation of the earth is moving the field of view over the sky. This is producing stripes which are likely to have some discontinuities between each other. So one has to be extremely careful about overdensities running along those stripes as this is probably not real. As mentioned earlier, different projections combined can help to verify if an overdensity seen in one projection is real.

3.4.2 Nearest Neighbors Alignments

Due to the problems of a purely visual inspection I described in the last paragraph I want to introduce an attempt to get a more objective impression of alignments of stars in the halo. For that I use an algorithm to visualize these alignments. An example for this is a code which identifies a given number of nearest neighbors for each star and fits lines through the distribution of these stars. To get a representation of the strength of this alignment the length of these lines are used. The closer the stars are together the longer is this line. Thus very long lines would be produced by clusters of stars, but the lines would have randomly distributed orientations. Larger groups of stars showing

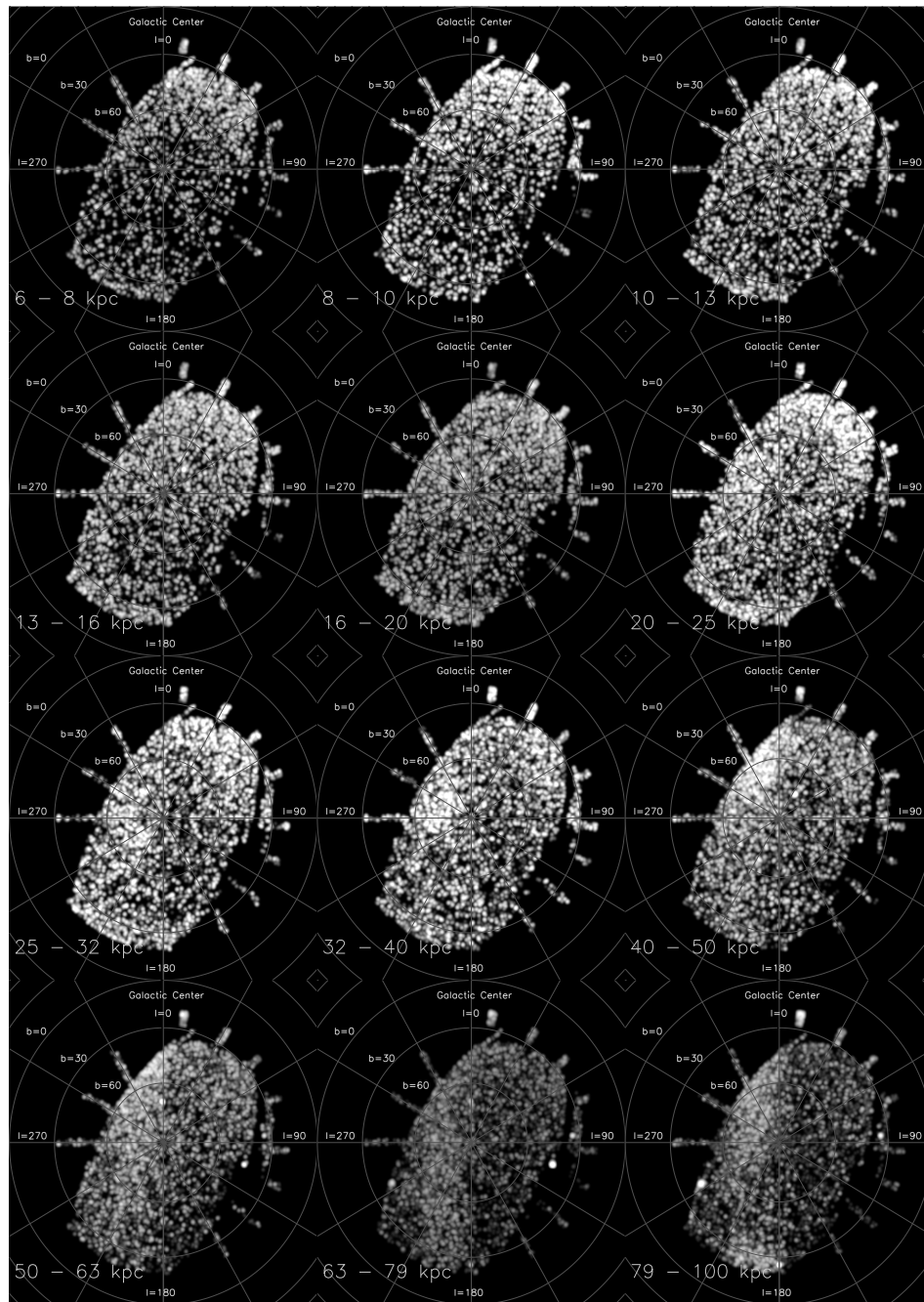


Figure 3.9: Heliocentric distance slices. The slices are chosen to have a constant distance modulus width of 0.5 mag starting with $14 \leq m - M < 14.5$. The Sagittarius stream can be clearly seen in many distance slices as it moves to the upper part of the plots with increasing distance.

3.4 Techniques for Finding and Studying Structures

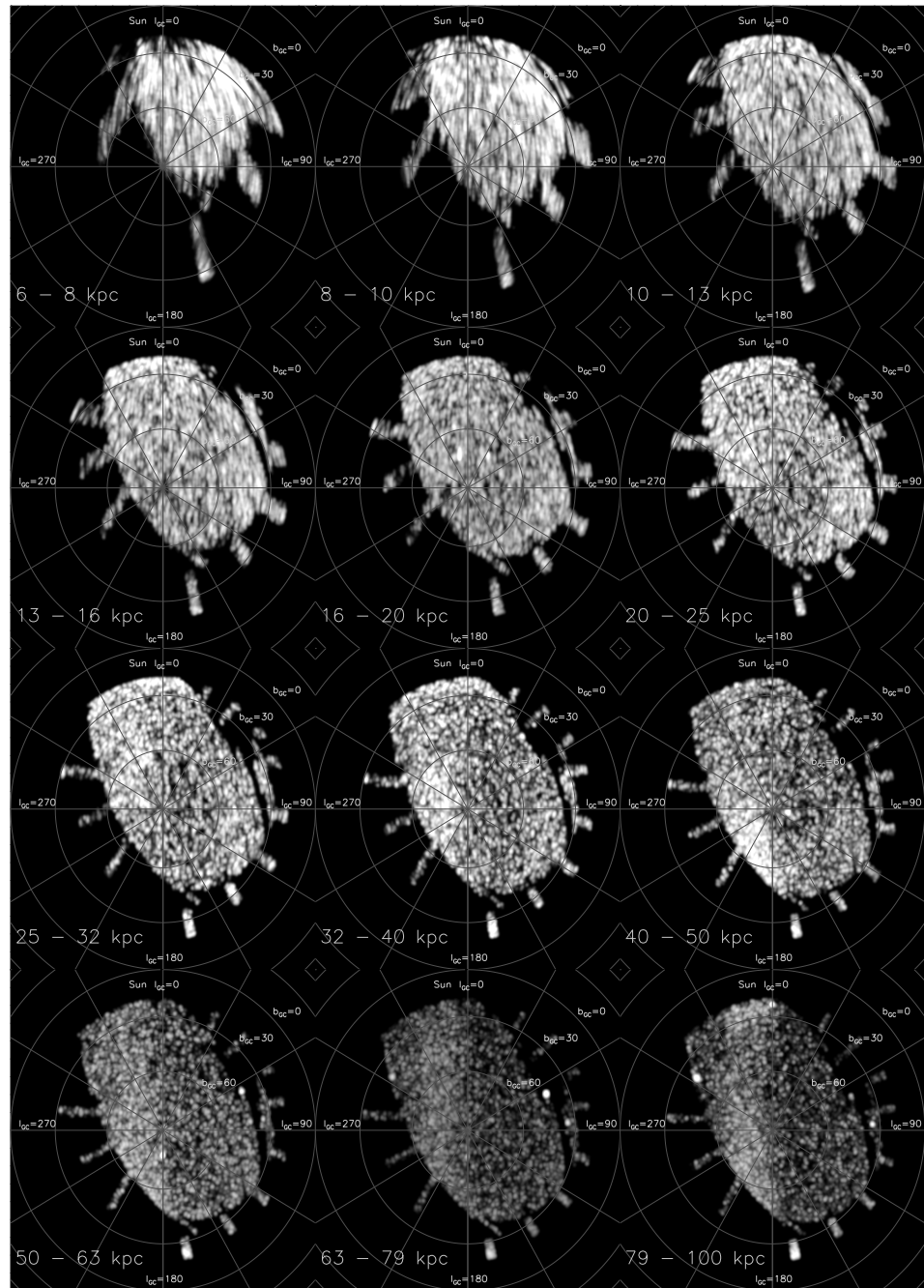


Figure 3.10: Galactocentric distance slices. It can be nicely seen in these distance slices that the relative difference of setting the viewing point to the Galactic Center instead of the Sun is large for small distances, but is getting very small quickly when increasing the distances. At small distances the visualization technique for the distance uncertainties causes the stars to smear out into long streaks whereas at larger distances they again appear pointlike as the direction of the uncertainty is nearing the line-of-sight.

the same orientation are possible stream candidates, where again the length of the line is inversely proportional to the separation of the stars. Figure 3.11 shows two example distance slices represented in this way.

Example of a Stream Candidate

In Figure 3.11 I show two distance slices which show a promising feature.

I follow up on this stream candidate by construction of a plane through the feature and the Galactic Center. As discussed earlier we can construct a plane through any two points in space and the Galactic Center. It is not clear, though, if such a plane incorporates the observed feature. To test if the feature falls into such a plane we pick two stars or simply coordinates of two points within it and build a plane through these points. Then I test if the plane includes the observed feature, e.g. by overplotting the stars included in the plane (see Figure 3.12). The critical point here is if the curvature of this intersection stripe is right, the thickness of the stripe can be adjusted according to the apparent thickness of the feature. Typically I'm using wedges instead of planes with parallel borders. The thickness of the plane can be adjusted to account for intrinsic thickness of the stream, distance uncertainties which might be directed towards the borders, increasing the thickness beyond the intrinsic one, or any effects which might have caused the stream to end up slightly off a perfect plane. If this test is passed one can go on and have a look at the plane.

Overdensity Maps

Having created a map like this one can also create overdensity maps which compare the density of stars in one plane or distance slice to the neighboring ones. In principle this method eliminates the background and thus enhances the signal from everything that deviates from a smooth background. However, the halo shows such a high level of structure that it is not clear if this method helps to enhance structures. Probably it will mostly work for strong structures for which an enhancement is not so critical in the first place.

The left panel of Figure 3.14 shows the density map of the plane in which the candidate stream is located. The middle panel shows the density distribution in the neighboring planes to both sides added up and the right panel shows the subtracted distribution.

3.4 Techniques for Finding and Studying Structures

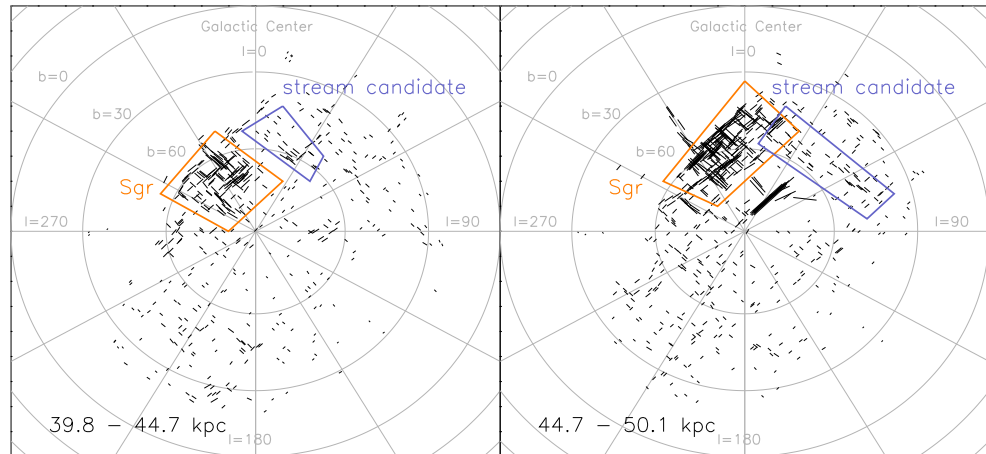


Figure 3.11: Nearest neighbor alignment visualization. Each star is represented by a line which is antiproportional in length with the area occupied by a given number of nearest neighbors (11 in this example). The orientation is given by a line fit through these stars. In the two distance slices shown here are a stream candidate was detected (marked by the blue boxes). The Sagittarius stellar stream is also very obvious through the large number of stars in the upper left of the field (marked by the orange boxes).

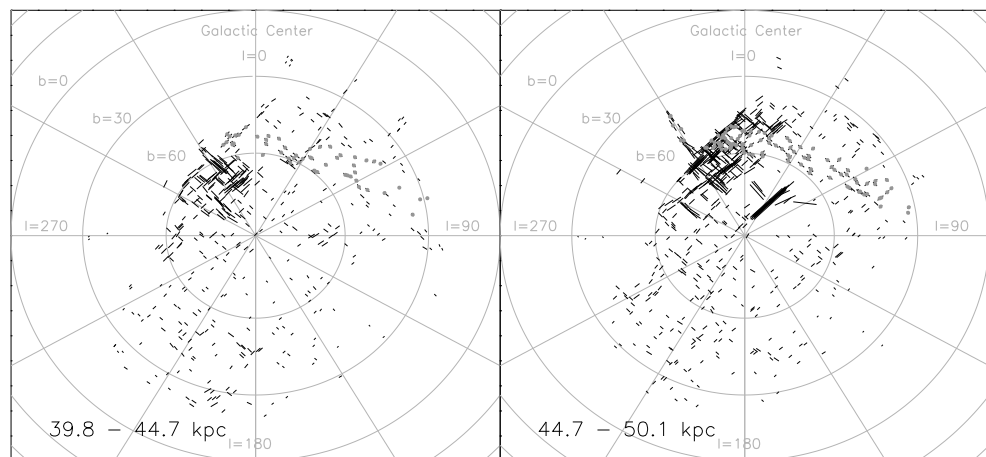


Figure 3.12: Nearest neighbor alignment visualization, stream candidate detection slices. The stars which fall onto a galactic plane are marked with gray dots.

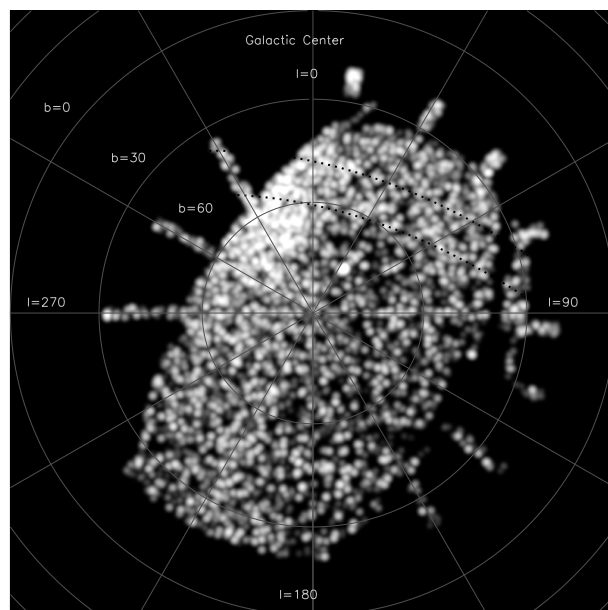


Figure 3.13: This figure presents the same distance range as in the two panels of Figures 3.11 and 3.12, but gives only the probability weighted spatial distribution of the BHB stars in this interval like in Figure 3.9. The intersection with the galactic plane is indicated by the dotted lines. There is only a very faint hint of an overdensity in this region, most likely too faint to raise attention in this visualization. This illustrates that a variety of visualization techniques can be useful as not every promising candidate seem to get picked up in every one of them.

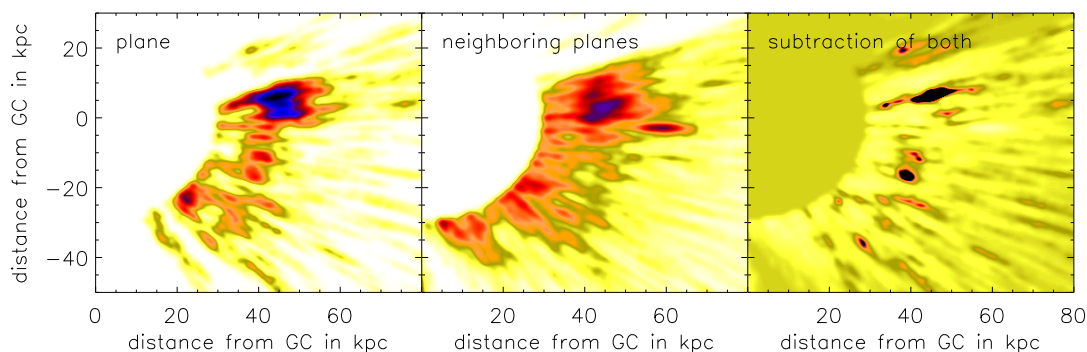


Figure 3.14: Overdensity maps. From the left: Density map of the plane, density map of the neighboring planes and an overdensity map, showing the subtraction of the other two maps. In the left and middle panel the large concentration in the upper half is part of the Sagittarius stellar stream. The chain of higher concentrated areas below that are at approximately the same distances the feature has been detected in.

Finding the Ideal Plane

There are different possibilities to find out if the chosen plane is the optimal plane for the studied structure. Maps of neighboring planes as shown before can already help as a test if the structure is spread over a wider range than included in the chosen plane. The might get solved in increasing the thickness of the plane, but one should also consider that that orientation of the plane might not be ideal for capturing the stream. Ideally the plane should include all the stars which seem to be associated with it, but to choose a wedge which is much wider than needed is also not good as it increases the contamination.

For optimizing the choice of orientation and thickness one possibility is to look at the distribution of stars perpendicular to the plane, another one is to go through different choices of the normal vector.

3.4.3 Spectroscopic Follow-up

Having the location of the feature in the plane one can fit orbits to show if it could be of tidal origin. Ultimately to show that the alignment of stars is not a coincidence one needs velocity information as well. Proper motions, meaning the velocity components perpendicular to the line-of-sight, can be only derived from observations made some years apart. Proper motions are calculated by comparing USNOB stars to the SDSS. Easier to obtain are radial velocities, which can either complement the proper motions to get the full set of velocities, or can also serve as an indicator for the nature of the stream in itself. One would expect a narrow range of radial velocities in the stream stars, whereas the halo as a whole shows a broad, approximately Gaussian distribution with a velocity dispersion of roughly 120 km s^{-1} with little dependence on galactocentric radius. Expecting some degree of contamination of stars which are not associated with the stream, a positive outcome of such a test would give a narrow spike on top of the broad halo distribution.

For the stream candidate stars for spectroscopic follow-up observations were selected using both the appearance on the on-sky distance slices and the galactic plane (see Figure 3.15 and Table 3.2). Spectroscopy of these stars with a ~ 2 meter class telescope permits measurement of radial velocities, giving an important test of the stream-like nature of the candidate overdensity.

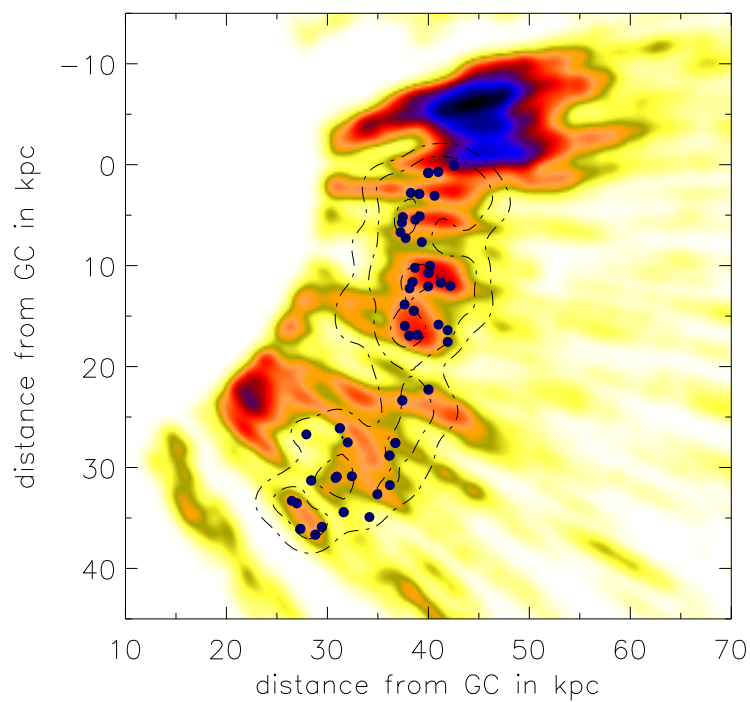


Figure 3.15: Example for the identification of spectroscopic follow-up candidates. In this case a concentration of stars detected in distance shells (black contours) lined up with overdensities in the corresponding galactic plane (color map). The stars considered for spectroscopic observations are marked as blue dots. The high density area in the top is part of the Sagittarius stream.

3.4 Techniques for Finding and Studying Structures

Table 3.2: Stream Candidate Stars

R.A. (deg)	Decl. (deg)	l (deg)	b (deg)	<i>g</i> (mag)	<i>u-g</i> (mag)	<i>g-r</i> (mag)	<i>P_{BHB}</i>
219.05870	10.959410	4.7247182	60.537704	18.78	1.22	-0.18	0.87
224.05080	7.9495860	5.7646804	54.793670	18.59	1.27	-0.13	0.89
237.74310	27.362850	43.958569	50.319871	18.79	1.21	-0.10	0.64
239.48370	27.253580	44.234942	48.779817	18.81	1.23	-0.08	0.64
227.24170	10.569040	12.509893	53.675328	18.72	1.22	-0.16	0.90
232.43280	27.224660	42.413475	54.946868	18.67	1.18	-0.21	0.79
227.92760	27.460600	41.767472	58.939984	18.83	1.26	-0.20	0.82
238.50050	23.016250	37.670946	48.676216	18.65	1.16	-0.13	0.70
235.51690	21.200610	33.766744	50.815600	18.72	1.21	-0.07	0.61
227.49910	26.543470	39.894492	59.184436	18.73	1.17	-0.18	0.81
225.56790	21.114090	28.697127	59.637746	18.89	1.05	-0.29	0.75
232.18600	19.812650	30.033224	53.345516	18.74	1.17	-0.16	0.72
223.21250	19.236350	23.612806	61.086228	18.79	0.98	-0.23	0.68
229.95940	22.206010	32.895698	56.050188	18.80	1.25	-0.13	0.89
230.09980	22.647400	33.719396	56.044531	18.83	1.24	-0.06	0.58
227.52050	20.937220	29.455767	57.849380	18.69	1.22	-0.09	0.64
226.72660	18.679620	24.991469	57.790034	18.76	1.17	-0.17	0.72
224.02710	17.852070	21.619578	59.842198	18.62	1.20	-0.23	0.83
223.88480	14.605860	15.804710	58.539960	18.81	1.15	-0.18	0.61
226.16800	14.266970	17.192060	56.430880	18.68	1.21	-0.18	0.87
222.85010	9.0471340	6.0657001	56.401725	18.72	1.12	-0.23	0.77
225.64320	7.5200600	6.7800845	53.270924	18.78	1.18	-0.16	0.72
225.41380	18.829650	24.386903	59.001414	18.80	1.21	-0.16	0.90
222.85320	5.2153250	0.82406467	54.004071	18.68	1.26	-0.16	0.91
249.61400	36.656930	59.177512	41.579014	18.85	1.22	-0.21	0.67
242.81360	44.061700	69.502532	46.768050	18.87	1.21	-0.10	0.64
238.52400	34.627540	55.408181	50.435695	19.04	1.17	-0.15	0.70
237.18300	30.915530	49.416250	51.307978	19.01	1.17	-0.13	0.70
237.56760	28.256470	45.300409	50.625399	18.93	1.25	-0.09	0.68
237.36210	32.190330	51.468367	51.269940	19.03	1.21	-0.10	0.64
257.09080	45.179820	70.684744	36.596089	18.85	1.20	-0.12	0.70
244.32370	44.317970	69.722155	45.665787	18.89	1.19	-0.13	0.70
233.73390	33.550740	53.488815	54.375853	18.97	1.13	-0.24	0.70
248.23000	49.804290	76.916957	42.431988	19.05	1.04	-0.25	0.74
240.55600	35.590810	56.981109	48.806929	19.01	1.18	-0.15	0.72
242.04460	34.542410	55.503888	47.536817	19.05	1.15	-0.24	0.70
237.80580	39.173610	62.600864	50.928429	18.92	1.22	-0.22	0.67
241.52340	30.101630	48.894687	47.496289	18.95	1.15	-0.18	0.61
245.54040	36.354000	58.389938	44.816638	18.94	1.22	-0.13	0.80

Chapter 3 Search for Stellar Streams in the Milky Way Halo

Table 3.2 (Continued)

R.A. (deg)	Decl. (deg)	l (deg)	b (deg)	<i>g</i> (mag)	<i>u-g</i> (mag)	<i>g-r</i> (mag)	p_{BHB}
242.14040	38.822180	61.848154	47.577540	19.00	1.23	-0.21	0.67
241.74860	40.344330	64.122529	47.834093	18.90	1.18	-0.14	0.70
239.81380	43.652550	69.282865	48.964401	19.05	1.21	-0.06	0.61
241.91590	42.711210	67.618174	47.547634	18.93	1.19	-0.14	0.70
237.58990	40.150710	64.169000	51.013723	18.82	1.21	-0.15	0.90
250.16330	47.471950	73.637238	41.376655	18.90	1.16	-0.18	0.81
252.55520	48.123670	74.387609	39.739238	18.95	1.22	-0.09	0.64
256.16210	42.376930	67.131922	37.064875	18.90	1.23	-0.06	0.61
245.60800	42.014780	66.376693	44.866546	19.00	1.16	-0.24	0.70
248.71270	47.821900	74.202820	42.325337	18.85	1.22	-0.19	0.87
249.26780	43.144700	67.866384	42.151687	18.95	1.25	-0.17	0.91
250.02780	42.364990	66.823195	41.589619	18.83	1.16	-0.14	0.70
225.45830	4.7502680	3.0000972	51.717787	18.97	1.17	-0.23	0.95
218.65420	10.055790	2.7844304	60.298354	18.97	1.22	-0.14	0.80
225.12980	9.3203270	8.7731904	54.729346	19.00	1.26	-0.22	0.82
227.13670	6.7554750	7.2055235	51.623671	19.06	1.06	-0.24	0.82
227.51740	10.751550	13.011901	53.541129	18.92	1.16	-0.18	0.61
226.28620	11.932690	13.671789	55.185663	18.97	1.27	-0.15	0.89
221.86550	12.920930	11.063923	59.384986	18.85	1.23	-0.15	0.80
230.02300	27.648060	42.593588	57.124763	18.84	1.25	-0.14	0.89
228.91230	10.547520	13.906440	52.264465	18.83	1.19	-0.18	0.81
229.85790	27.756700	42.755607	57.284352	18.90	1.22	-0.09	0.64
228.58050	28.412690	43.721983	58.482901	18.87	1.10	-0.22	0.63
236.16510	22.405060	35.861010	50.584325	19.12	1.07	-0.27	0.86
231.26970	23.234570	35.216156	55.155415	18.86	1.26	-0.22	0.82
231.96780	24.366150	37.397057	54.805720	19.02	1.22	-0.20	0.67
226.00590	20.684430	28.147558	59.114611	18.81	1.20	-0.14	0.70
228.45770	24.384190	36.142238	57.926594	18.89	1.23	-0.20	0.87
230.20210	17.696590	25.553726	54.359345	18.95	1.23	-0.19	0.87
232.98230	23.644670	36.570193	53.735076	18.90	1.24	-0.06	0.58
227.36370	20.106220	27.890492	57.723248	18.86	1.20	-0.09	0.64
232.99490	19.519950	29.992196	52.529876	18.94	1.20	-0.14	0.70
230.00980	19.498630	28.358418	55.173662	18.95	1.19	-0.14	0.70
227.55940	19.247020	26.503487	57.257890	19.00	1.19	-0.21	0.79
231.87560	15.766700	23.639588	52.127373	18.91	1.20	-0.17	0.72
227.71080	16.257090	21.585132	55.976366	19.02	1.04	-0.24	0.82
232.01950	14.526100	21.912951	51.480402	18.94	1.26	-0.20	0.82
221.01300	13.881410	11.829037	60.594876	18.87	1.14	-0.22	0.66
227.16910	14.033460	17.632490	55.463400	18.87	1.28	-0.21	0.82

Table 3.2 (Continued)

R.A. (deg)	Decl. (deg)	l (deg)	b (deg)	g (mag)	$u-g$ (mag)	$g-r$ (mag)	p_{BHB}
228.03000	8.3492360	10.132549	51.814628	19.03	1.20	-0.21	0.79
219.23910	11.088610	5.1503098	60.473348	18.92	1.23	-0.23	0.83
221.64420	8.3433960	3.7313560	56.921894	19.08	1.13	-0.24	0.70
223.88590	5.6234900	2.4730132	53.481945	18.94	1.18	-0.16	0.72

Table 3.2: Stream candidate stars

3.5 Summary

In this chapter I presented the basic ingredients and techniques applied in this thesis for detecting and studying structures in the stellar halo. I used the SDSS together with BHB stars as standard candles allowing to probe the large field of sky covered by the survey out to distances of more than 100 kpc with great accuracy. BHB stars are selected using a method which aims to optimize turning the knowledge about the photometric properties of spectroscopically, and therefore more accurately, classified BHB stars into a selection based on photometry alone. A photometric selection is important to make full use of the much larger photometric sample and to avoid any bias introduced by the selection of spectroscopy targets. In this chapter I presented the new detection of a candidate stream, the next chapter will focus on a well known feature in the halo, the Sagittarius stellar stream. Being the largest feature of that kind it can be studied in much more detail.

4

THE STRUCTURE OF THE SAGITTARIUS STELLAR STREAM AS TRACED BY BLUE HORIZONTAL BRANCH STARS

adapted from Ruhland et al. 2011, ApJ, 731, 119

I USE A SAMPLE of blue horizontal branch (BHB) stars from the Sloan Digital Sky Survey Data Release 7 to explore the structure of the tidal tails from the Sagittarius Dwarf Galaxy. I use a method yielding BHB star candidates with up to $\sim 70\%$ purity from photometry alone. The resulting sample has a distance precision of roughly 5% and can probe distances in excess of 100 kpc. Using this sample, I identify a possible extension to the trailing arm at distances of 60–80 kpc from the Sun with an estimated significance of at least 3.8σ . Current models predict that a distant ‘returning’ segment of the debris stream should exist, but place it substantially closer to the Sun where no debris is observed in my data. Exploiting the distance precision of my tracers, I estimate the mean line-of-sight thickness of the leading arm to be ~ 3 kpc, and show that the two ‘bifurcated’ branches of the debris stream differ by only 1–2 kpc in distance. With a spectroscopic very pure BHB star subsample, I estimate the velocity dispersion in the leading arm, 37 km s^{-1} , which is in reasonable agreement with models of Sgr disruption. I finally present a sample of high-probability Sgr BHB stars in the leading arm of Sgr, selected to have distances and velocities consistent with Sgr membership, to allow further study.

4.1 Introduction

Tidal debris from dwarf galaxies and stellar clusters dissolving in the Milky Way potential are an important contributor to the stellar halo of the Milky Way (e.g., Searle

Chapter 4 The Structure of the Sagittarius Stellar Stream

& Zinn, 1978; Ibata et al., 1994; Bullock et al., 2001; Bullock & Johnston, 2005; Belokurov et al., 2006a; Bell et al., 2008). In recent years, many elongated substructures have been found in the stellar halo of the Milky Way (e.g., Ibata et al., 1995, 2003; Yanny et al., 2003; Grillmair & Johnson, 2006; Grillmair & Dionatos, 2006; Grillmair, 2006; Belokurov et al., 2007b) and around other nearby galaxies such as Andromeda (e.g., Ibata et al., 2001a; McConnachie et al., 2009), and a number of external galaxies (e.g., NGC 891; Mouhcine et al., 2010; NGC 5907; Zheng et al., 1999; Martínez-Delgado et al., 2008, 2010) showing that the build-up of stellar halos through accretion of satellite galaxies is a common phenomenon. Besides the general implications such stellar satellite debris has for building and testing the galaxy formation paradigm, the detailed investigation of the individual structures provides important information about the specific formation history of individual galaxies. The spatial distribution and kinematics of the tidal debris of dwarf galaxies or globular clusters is also an important source of information about the gravitational potential of the Milky Way (e.g., Johnston et al., 1999; Helmi, 2004a; Law et al., 2005; Fellhauer et al., 2006; Koposov et al., 2009; Law & Majewski, 2010b; Peñarrubia et al., 2010b).

In this context, the Sagittarius stellar stream (Sgr), the most massive stellar stream around the Milky Way, is a central case study. Discovered in 1994 (Ibata et al., 1994), the tidal tail has been charted across more than one full wrap around the Milky Way in M-giants (Majewski et al., 2003, see also Yanny et al., 2009), main sequence stars (Belokurov et al., 2006a), clusters (e.g. Bellazzini et al., 2003, and references therein), and blue horizontal branch (BHB) stars (Newberg et al., 2003; Monaco et al., 2003; Clewley & Jarvis, 2006; Yanny et al., 2009; Niederste-Ostholt et al., 2010). The spatial tightness of the stream in combination with its full 360° span makes it an important probe of the potential (e.g., Helmi & White, 1999; Moore et al., 1999; Ibata et al., 2001c, 2002; Johnston et al., 2002, 2005; Helmi, 2004a; Lewis & Ibata, 2005; Binney, 2008), of the disruption process (Ibata et al., 2001b; Helmi & White, 2001; Peñarrubia et al., 2010a), and of the impact of population gradients and cluster contents of the Sgr dwarf on the properties of the tail (e.g., Da Costa & Armandroff, 1995; Majewski et al., 2003; Martínez-Delgado et al., 2004; Bellazzini et al., 2003; Law & Majewski, 2010a).

Despite the wealth of observational data, models of the stream have failed so far to match all the observational constraints by quite a margin. To explain the observations different galaxy potentials have been invoked, with arguments for prolate (Helmi, 2004b; Law et al., 2005), spherical (Fellhauer et al., 2006), oblate (Johnston et al., 2005) or triaxial (Law & Majewski, 2010b) dark matter potentials. To explain some striking

features, such as the ‘bifurcation’ (Belokurov et al., 2006a), Peñarrubia et al. (2010a) invoked that the progenitor of the Sgr stream may have been a rotating disk galaxy rather than a pressure-supported dwarf galaxy as assumed by most previous models. However, no single model seems to explain all parts of the stream while it is also not entirely clear that all the overdensities found in the plane of the Sgr stream are actually remnants of the same progenitor. A more precise and more complete empirical picture of the Sgr stream could be crucial in clarifying this issue, and this constitutes the central goal of the present chapter.

In recent studies of the Sgr stream, there has been increased attention toward BHB stars as a tracer population. Due to their relative brightness they can be observed out to ~ 100 kpc in the stellar halo of the Milky Way using Sloan Digital Sky Survey (SDSS) data. However, to take full advantage of area coverage of surveys such as SDSS, the identification of these stars needs to be done with photometric data alone. Many publications based their selection on color boxes (Yanny et al., 2000, 2009; Niederste-Ostholt et al., 2010) that included a significant contamination from other blue stars (primarily blue straggler (BS) stars). Such contaminants can dominate in number, and are 1-2 mag fainter in absolute magnitude, confusing the interpretation of halo structure using such samples.

In this thesis, I use SDSS data in the North Galactic Cap to study Sgr tidal debris. I choose color-selected BHB star candidates as sparse tracers of the ancient, metal poor populations with well-defined absolute magnitudes, that are $\sim 3-4$ magnitudes brighter than the densely populated main-sequence turn-off (MSTO) stars. Going beyond other recent studies (e.g., Yanny et al., 2009; Niederste-Ostholt et al., 2010) of the Sgr system in BHB stars I use a refined selection technique (described in Chapter 3) based on a spectroscopic training sample which reduces the contamination by other stellar populations (Bell et al. 2010). I show empirically that the distance uncertainties in my sample are small, of the order of 5%. I use these stars to chart out the Sgr stream, focusing on three issues: delineating the distant (> 50 kpc) overdensities that may be associated with the Sgr trailing arm, on constraining and measuring the thickness of the leading arm, and on presenting a sample of high-probability Sgr BHB star candidates with positions and velocities consistent with Sgr membership for further study. Furthermore I explore the bifurcation that has been found by Belokurov et al. (2006a) perpendicular to the orbital plane of the stream and its appearance in BHB stars.

4.2 Data

4.2.1 Blue Horizontal Branch Stars

Kinematic Sample

The radial velocity sample, which is a sub-sample of the photometric sample, was selected based on the spectra as described above offering a much higher BHB purity $\gtrsim 90\%$ than the method applied on the stars with photometry only (see Chapter 3 for details on both the spectroscopic (3.2.1) and photometric (3.2.2) classification). To not unnecessarily restrict the sample size, I use the full radial velocity sample in these cases and ignore for these stars the probabilities which were assigned based on their colors (i.e., I do not use the lower probability limit of 50% mentioned above). The total sample size is 5233 stars, of which 807 are located in the Sgr plane (see Section 4.2.1). From these 807 stars 616 would fulfill the 50% probability criterion, giving a success rate of spectroscopic BHB stars in this selection of 76%. Throughout this thesis the radial velocities are given in the Galactic standard of rest, which are the heliocentric radial velocities corrected for the Galactic rotation assuming a rotation velocity of 220 km s^{-1} for the local standard of rest and $(+10.0, +5.2, +7.2) \text{ km s}^{-1}$ for the solar motion where the directions are defined as pointing towards the Galactic center, in the direction of rotation and towards the north Galactic Pole (see Xue et al., 2008 for details).

Sagittarius in a Galactic Plane

For much of my analysis, I focus on stars in the presumed orbital plane of the Sgr stream only. I define this ‘Sagittarius plane’ to encompass the Sgr stream and the Galactic Center; this is presumably close to the orbital plane of the Sgr stream (see Section 3.3 for the principal technique of the plane construction). To ensure consistency with models, I use the same pole as the Two Micron All Sky Survey (2MASS) papers (e.g. Majewski et al., 2003) at $(l, b) = (273^\circ.8, -13^\circ.5)$. Stars are considered to be in the plane if they lie within $\pm \sim 27^\circ$ of this plane; this definition naturally yields not a plane but a wedge, whose physical thickness increases with distance from the Sun. Stars are projected onto this plane by conserving the distance to the Sun (i.e., the plane is a projection of shell segments onto the plane). The Sagittarius plane defined here includes 73,066 stars (6905 with a BHB star probability greater than 50%) from the total 389,785 stars (28,270 with a BHB star probability greater than 50%) in the SDSS volume that are inside the color box.

BHB distance scale comparison with M giants

As a comparison data set I use M giants from the 2MASS (Skrutskie et al., 2006) to compare the distance scale of my BHB star data set in relation to other stellar populations, which were used for studying the Sgr stellar stream. In particular, this M giant data set was also used as the basis for the models I will compare to later. M giants can be used as distance indicators out to large distances making them a good stellar population for studying the Sgr system (especially in the near infrared). Due to the complete coverage of the sky, it is possible to observe the stellar stream along its whole orbital path. A disadvantage of M giants as distance indicators is their rather large distance uncertainties (argued to be $\sim 17\%$; Law et al., 2005), and a likely distance offset with the BHB and literature distance scales.

I derive a sample of M giants from the full 2MASS catalog following the method described in Majewski et al. (2003) for which I show the distribution in the plane of the Sgr stellar stream in Figure 4.1. The comparison with the BHB star population also shown in this plot reveals a distance offset between the two populations with the M giants being about $\sim 8\%$ closer to the Sun than the BHB stars in the leading arm region of Sgr. As the distances of M giants are less well determined than those of BHB stars I also see a difference in the width of the leading arm in the different populations; the width seen in BHB stars is only $\sim 40\%$ of that seen in M giants as it appears in the samples presented here. Obviously this mismatch will propagate through to the models based on M giant observations (e.g., Law et al., 2005; Law & Majewski, 2010b), so that I am expecting to see this mismatch to some degree in the comparison to these models. Note that I do not adjust my distance scale (or those of other data or models) to account for possible distance offsets in either case (the $\sim 4\%$ mismatch between the BHB distance scale and the literature determinations, or the $\sim 8\%$ mismatch between the BHB and M giant distance scales). In particular, this means that throughout the chapter different data sets or models shown in the same plot can have different distance scales. Note that the offset to the distance scales of the two comparison samples have opposite directions, while the clusters and dwarf spheroidals have systematically larger distances, the M giants have smaller distances compared to my BHB star sample. This implies an even larger offset between these distance scales of about 12% . Evidently a better characterization of the M giant distance scale would be of importance for a direct comparability of different stellar populations as distance indicators.

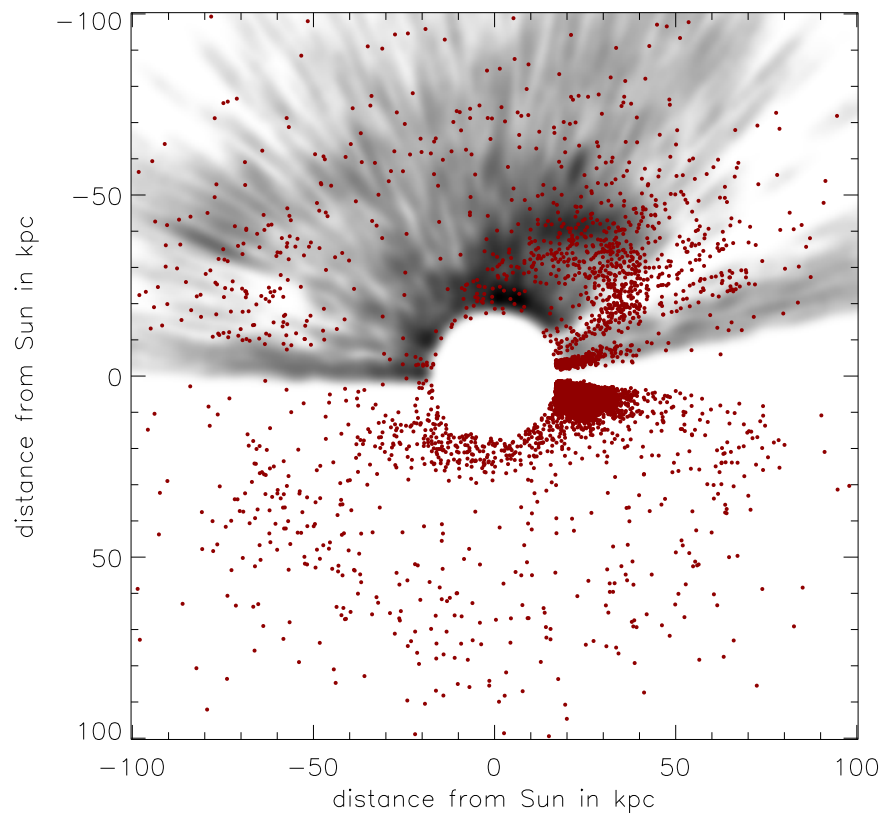


Figure 4.1: Distribution of M giants from 2MASS in the Sagittarius orbital plane is shown as red dots with a gray BHB star probability map in the background (see Section 4.3.1). For both the BHB stars and the M giants I exclude the inner 20 kpc. The M giant population in the leading arm (+20,+35) appears closer to the Sun than the BHB stars, which I interpret as an 8% mismatch in the distance scale between the two different populations. Furthermore, the leading arm appears to be much more compact in width in BHB stars than in M giants, presumably a reflection of the substantially larger distance uncertainties in the M giants.

4.2.2 N-Body Models for the Sgr Stream

I will compare my BHB maps with simulations of the evolution of the Sagittarius dwarf spheroidal in the Milky Way potential (Law et al., 2005; Law & Majewski, 2010b; Peñarrubia et al., 2010a) and summarize these models here. The Law et al. (2005) models adopt a smooth, rigid potential representing the Milky Way, which consists of a Miyamoto-Nagai disk, a Hernquist spheroid, and an axisymmetric logarithmic halo of different flattenings: $q = 0.9$ (oblate), 1.0 (spheroidal), and 1.25 (prolate). I will also use a new model by Law & Majewski (2010b) for comparison, which is based on a triaxial dark matter halo with a minor/major axis ratio $(c/a)_\Phi = 0.72$ and a intermediate/major axis ratio $(b/a)_\Phi = 0.99$ at radii $20 < r < 60$ kpc. This corresponds to a nearly-oblate ellipsoid whose minor axis is contained within the Galactic disk plane and approximately aligned with the line of sight to the Galactic Center. In both model generations, the Sagittarius dwarf itself is represented by 10^5 self-gravitating particles. All of the models were constructed to fit the system of the Sagittarius stellar stream as seen in 2MASS M giants. To account for the photometric distance errors of the M giant sample, a artificial random distance error of 17% was applied to the simulated debris particles. Following the suggestion of a triaxial halo, Peñarrubia et al. (2010a) presented a model which does not assume a pressure-supported dwarf spheroidal galaxy as the progenitor of the Sgr stellar stream, but a late-type rotating disk galaxy. This model also reproduces a bifurcation in the leading arm of the stream as seen by Belokurov et al. (2006a).

4.3 Results

4.3.1 Probabilistic BHB Density Maps

The general technique to create maps for the visualization of the BHB star density, accounting both for the finite probability that stars are BHB stars (as described in Section 3.2.2) and for the distance uncertainties (see Section 3.2.3) was already explained in Section 3.2.3. Throughout this chapter, I only consider stars with $p_{BHB} > 0.5$ unless stated otherwise. These maps then get convolved with a Gaussian kernel with a size of $\sigma = 1$ kpc for presentation purposes¹. I apply this technique to create spatial maps of the Sgr debris and for plotting the velocity distribution along the orbital longitude of the system. In Figure 4.2, I illustrate the effect of different probability cuts on the Sgr plane.

¹Later I will use a polar coordinate system, which is defined in Section 4.3.2, where a kernel of 0.5 kpc in distance and $\sim 2^\circ$ in the orbital angle coordinate is used.

Chapter 4 The Structure of the Sagittarius Stellar Stream

This is of particular interest in the context reported in Section 3.2.2 that the probability assignment is assumed to work less well for larger distances.

My basic map, the distribution of BHB stars in the Sgr stream plane, is shown in Figure 4.3 (top panel). The uppermost panel shows the full sample of stars, where the overdensities are pointed out by dashed lines. Clearly visible is the leading arm of the stream to the right of the plot (white line). Less prominent, but still significant (see below)², is the overdensity denoted by the black dashed line. In common with Newberg et al. (2003) who detected part of the overdensity and Newberg et al. (2007) where it was also shown in BHB stars, I provisionally attribute this to the Sgr trailing arm. I find further support for this overdensity in the on-sky plot of a broad distance slice ($60 \text{ kpc} < d < 80 \text{ kpc}$) covering most of the overdensity seen in the plane. Figure 4.4 shows the on-sky view in which the plane is clearly visible as an overdense region. Also clearly visible in Figure 4.3 is the globular cluster NGC 2419 at $(x,y)=(-80,-35)$, but its relation to the Sgr trailing stream is unclear.

In the direction of the leading arm, BS contamination is faintly visible as an echo of the leading arm at $\sim 80 \text{ kpc}$ from the Sun. It is noteworthy that my selection has significantly reduced this contamination compared to, e.g., Niederste-Ostholt et al. (2010). Since I assign all stars with $p_{BHB} > 0.5$ as BHB stars this causes an overestimate of BS star distances (by 1-2 mag, or a factor of two or so in distance, as observed). I illustrate the expected location of this shadow caused by stars in the leading arm region by the dotted black lines in Figure 4.3 (giving the transposition of the white line for stars overestimated by 1.5 and 2 mag, respectively). I show also the Boötes dwarf, which happens to lie in the Sgr plane.

I have adopted two different methods to estimate the significance of the candidate trailing stream. In the first approach, I estimate the significance in small areas of $4 \text{ kpc} \times 4^\circ$ along the trailing stream. I divide the plane into areas of constant radial and angular extent, and count the number of stars in these fields. For a field i the number of stars in the field is N_i . The mean number of stars in a ring with constant heliocentric distance \bar{N}_{ring} and standard deviation of σ_{ring} is derived for each value of heliocentric distance range to account for the increasing volume of the wedge with increasing distance (see Section 4.2.1 for a description of the geometry of the plane). I also exclude the angular range to the right of the area indicated in Figure 4.3 from the calculation of the mean and

²Among other features this appears somewhat more prominent if a lower probability cut for BHB stars is applied (e.g., 20% or 30%, see Figure 4.2).

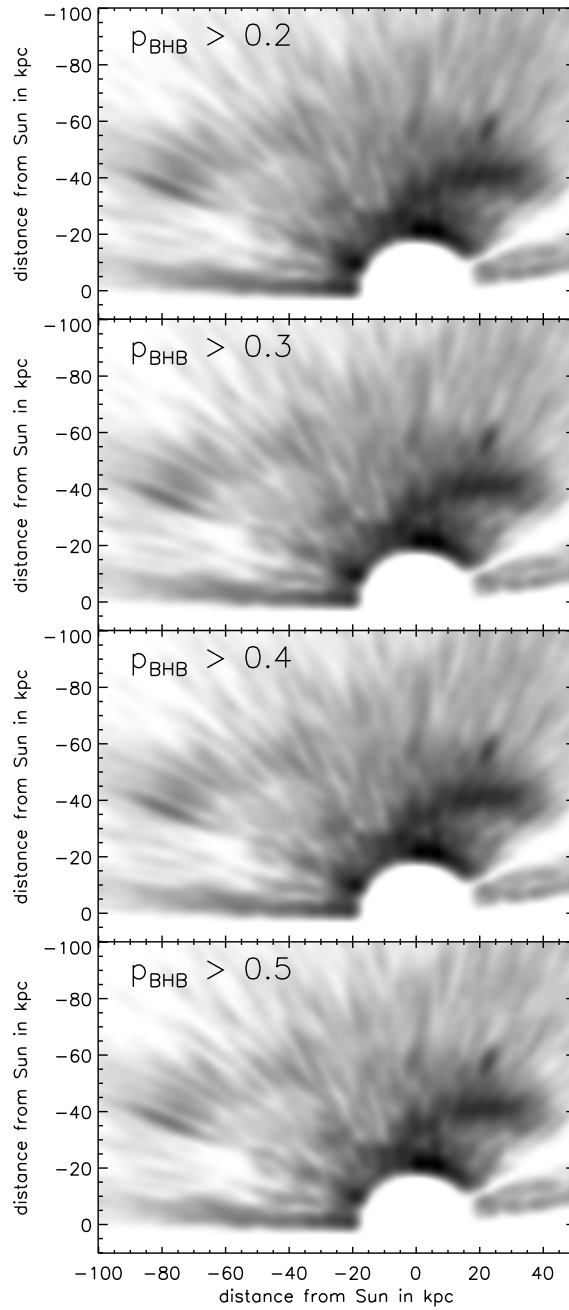


Figure 4.2: Density maps of BHB stars in a plane which includes the Sgr tidal tail and the Galactic Center. The maps are derived as explained in Section 3.2.3 (see also Section 4.3.1) taking into account BHB star probabilities and distance uncertainties. The four panels illustrate the dependence of these maps on the probability cut. The prominent overdensities in these maps are conserved for all probability cuts, showing that issues with the probability assignment are unlikely to affect my analysis significantly.

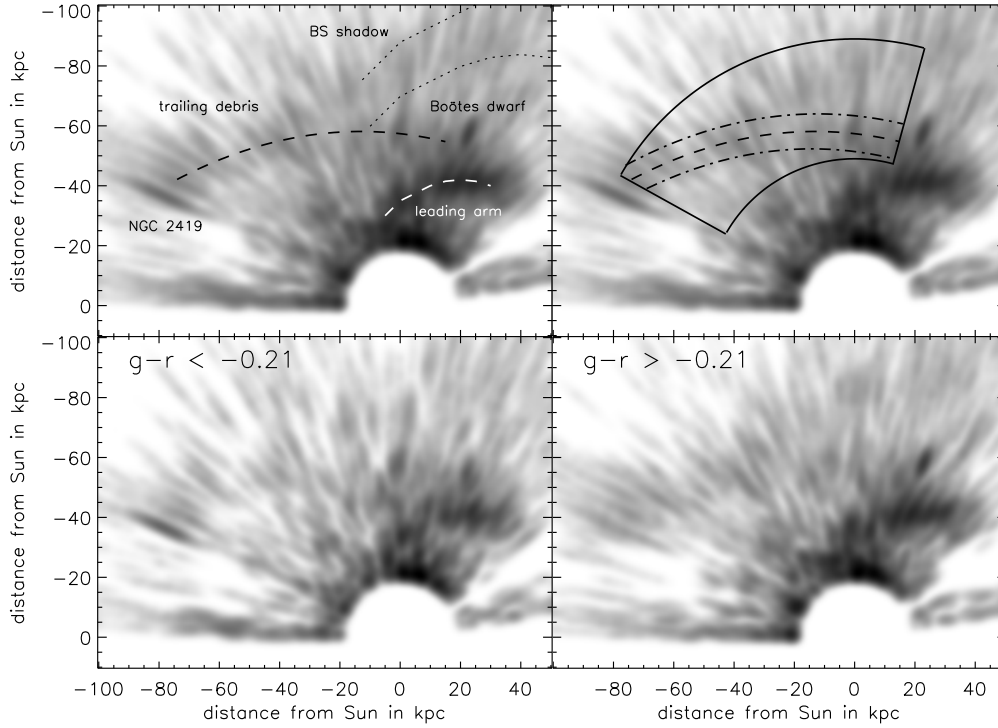


Figure 4.3: Density maps of stars with $p_{BHB} > 0.5$ in a plane which includes the Sgr tidal tail and the Galactic Center. The maps are derived as explained in Sections 3.2.3 and 4.3.1 taking into account BHB star probabilities and distance uncertainties, with a minimal accepted probability of 50%. The upper panels shows the full sample whereas the two lower panels show the sample split into redder (right panel) and bluer (left panel) BHB stars. The Sun is located at the origin. To enhance the contrast in the regions of the Sgr debris the innermost 20 kpc are not shown. Clearly visible is the leading arm of the Sagittarius stream stretching approximately from -10 to 30 in x and -20 to -40 in y (indicated by the short white dashed line). This feature is very clear in the full sample and the red subsample whereas it is very patchy in the blue subsample. The two outer dotted black lines illustrate where the expected shadow of misinterpreted blue straggler stars should be assuming stars which are intrinsically 1.5 and 2 mag fainter, respectively. Another clearly visible feature is the cluster NGC 2419 at $(x,y)=(-80,-35)$ which is, in contrast to the leading arm, more prominent in the blue. It is not clear if NGC 2419 is associated with the candidate trailing arm (see Section 4.3.4). I also see a very faint indication of an overdensity in the region of -80 to 20 in x and around -50 in y , spanning the region between the cluster and the leading arm (indicated by the long black dashed line). If this overdensity is real it could possibly be associated with Sgr and represent part of the trailing arm. The upper right panel illustrates the selection region used for an estimate of the significance of this overdensity discussed in Section 4.3.1. The Boötes dwarf galaxy can be clearly seen just above the leading arm of Sgr at $(x,y)=(20,-60)$.

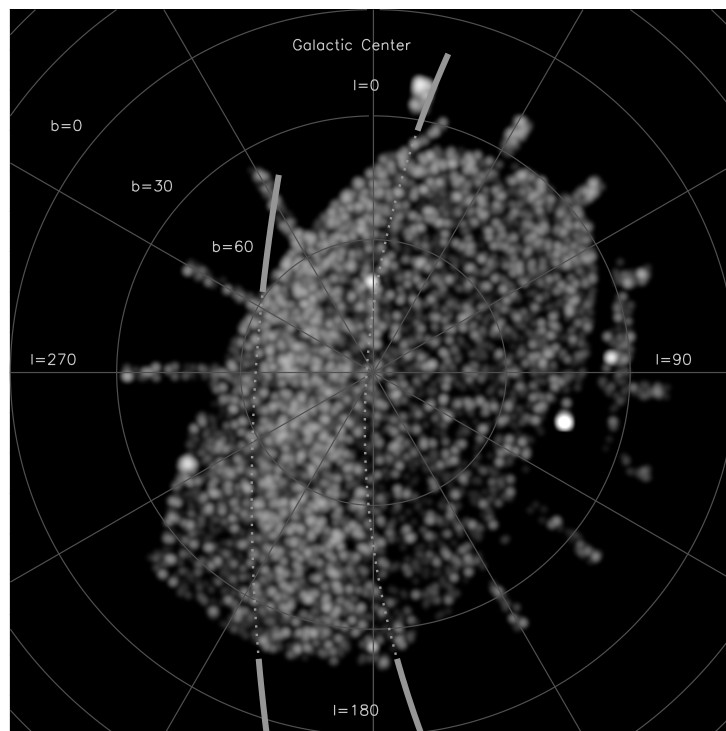


Figure 4.4: On-sky view of a distance shell ($60 \text{ kpc} < d < 80 \text{ kpc}$) which holds most part of the faint overdensity I see in the plane which could represent part of the trailing arm of Sgr. The borders of the plane are indicated by the dotted lines, for better visibility they are indicated by thick solid lines outside the survey field. The stars that I attribute to the Sgr trailing arm with $180^\circ < l < 270^\circ$ (and what I argue are blue stragglers in the leading arm at $270^\circ < l < 360^\circ$) are clearly confined to the Sgr plane.

Chapter 4 The Structure of the Sagittarius Stellar Stream

standard deviation for all distances to avoid the obvious overdensities from the leading arm in this area as well as the contamination at larger distances from misinterpreted BS stars. The significance of any deviation in the number of stars of each field within this sample of equidistant fields in units of the standard deviation σ for region i is given by $\sigma_i = (N_i - \bar{N}_{ring}) / \sigma_{ring}$.

I take the region around the suggested position of the trailing arm as indicated in the upper right panel of Figure 4.3 by the dash-dotted lines and compare the average deviation of these fields with a comparison sample in the same plane but outside the trailing arm area. Note that this area does not include NGC 2419 to get a clean estimate of the significance of the proposed trailing arm. These fields are chosen in a way that the number of fields per distance interval of on- and off-stream fields is the same. The 57 on-stream fields show an average deviation of $+0.4\sigma$ per field, indicating a weak overdensity, whereas the 57 off-stream fields show with an average deviation of -0.6σ per field the corresponding underdensity.

To get an idea of the significance of the whole extent of the structure I adopt a larger area, as shown in Figure 4.3 (upper right panel). Within this region consisting of 200 fields I randomly select a number of fields, equal to the number of stream fields I used earlier, and determine the average number of stars in this selection. Applied many times this bootstrapping method gives an estimate of the mean value and standard deviation I can expect in a randomly selected structure of this size. I find a mean value of 23.5 stars per field in the large box with a standard deviation of 1.3 stars. The average number of stars in the selected structure fields is 28.5 per field which corresponds to an deviation of 3.8σ from the mean value. The candidate stream fields are compared with all fields – including stream fields – potentially underestimating the significance.

In the two lower panels of Figure 4.3, I show the maps that result after splitting the BHB sample in $g-r$ color at $g-r = -0.18$, such that the number of stars with $g < 18.5$ is about equal in the red and blue subsamples. The main motivation to do so is to probe the variations of the stellar population in the Sgr stream. In Figure 4.3, I show the red subsample in the lower right panel and the blue subsample in the lower left panel. I find that Sagittarius (especially the leading arm) is much more prominent in the red stars (see Figure 4.3) while other parts, such as NGC 2419, are dominated by blue stars.

In summary, I find Sgr's leading arm to be a prominent feature in BHB stars, even more so when the BHB star sample gets restricted to stars which are on the red part of the blue horizontal branch in $g-r$ color. Furthermore I observe a faint overdensity

stretching out over most of the plane covered by SDSS, connecting the leading arm with the globular cluster NGC 2419. This overdensity was also described by Newberg et al. (2003, 2007) as a part of the trailing arm of Sgr.

4.3.2 Thickness of the Leading Arm, and Spatial Selection of Sgr BHB Star Candidates

In this section I measure the line-of-sight thickness of the Sgr leading arm and use this measurement to select a sample of highly likely Sgr member stars. In this subsection, I will present a selection based on the spatial distribution only which will be used for the analysis in the following subsection. Later I will restrict the selection of a ‘clean sample’ to the radial velocity subsample for which I apply a similar selection technique. In what follows, I restrict my attention to the Sgr leading arm; the trailing arm (and candidate trailing arm debris) is in the wrong hemisphere and/or too distant to have SDSS radial velocity information.

I adopt the heliocentric polar coordinate system defined by Majewski et al. (2003) which was also used by Law et al. (2005) and Law & Majewski (2010b). In this system, the angle is defined as $\Lambda_{\odot} = 0^{\circ}$ passing through the main body of Sgr and increasing along the direction of the trailing tail of Sgr. The definition of the coordinate system is illustrated in Figure 4.5 where the prolate version of the models is shown together with my BHB star data in the large panel. The inset panel shows the data alone.

I first measure the width of the leading arm using the full sample of stars in the Sgr plane (not the Gaussian-distributed sub-objects), as is appropriate for measuring line-of-sight distance scatter; the distribution of the stars is shown in Figure 4.6. I divide the angle-distance-plane into angular slices along an orbital angle range of $250^{\circ} \lesssim \Lambda_{\odot} \lesssim 300^{\circ}$ and fit the distance distribution of the stellar density with a function consisting of three components: an exponential function and constant component to fit the background distribution of halo stars, and a Gaussian for the Sagittarius stream. The fit can be described by the expression³ $\Sigma(d_{\odot}|\Lambda_{\odot}) = P_0 + P_1 * \exp(\frac{-d_{\odot}}{P_2}) + P_3 * \exp(-0.5 * (\frac{d_{\odot} - P_4}{P_5})^2)$. The best fit was determined using a chi-square algorithm. As the Sagittarius leading arm is significantly more prominent in the red subsample of BHB stars I also apply the fit to the red part alone (see Figure 4.7). For comparison the histogram of the corresponding

³Due to the proximity of Boötes, I added a second Gaussian to this expression to isolate the profile of Sagittarius in the relevant bins from Boötes.

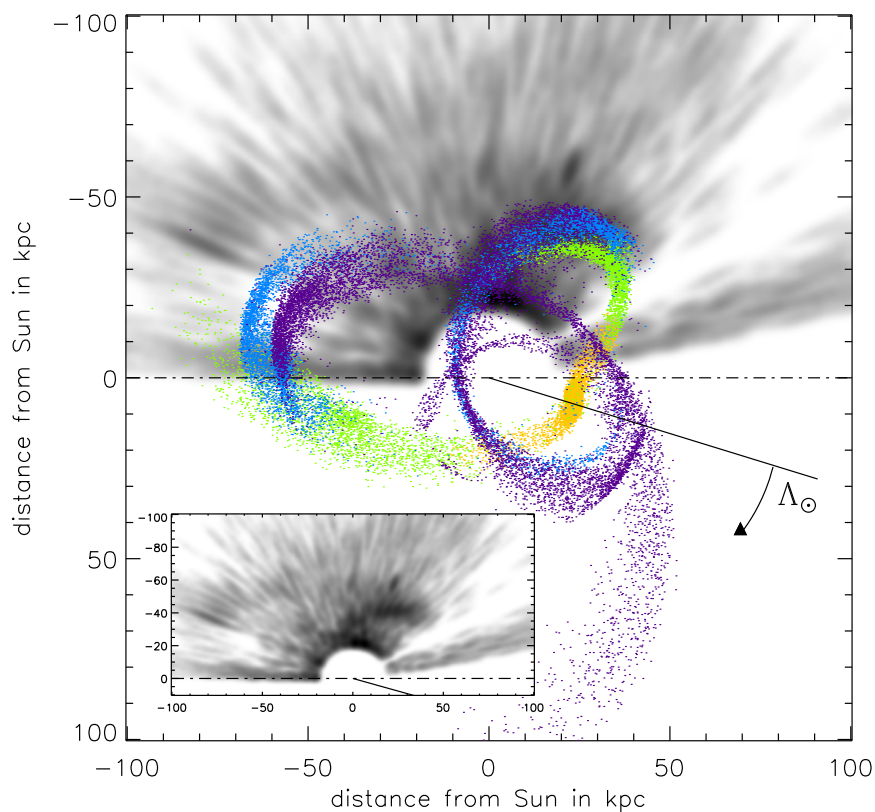


Figure 4.5: Comparison of the BHB star density ($> 50\%$ sample) with the Law et al. (2005) prolate potential model of the Sagittarius stellar stream and in the small panel data alone for clarity. The colors showing the model particles show debris lost from the progenitor during different epochs. The yellow points show debris stripped since the last apogalacticon, while green, blue, and purple show debris which became unbound two, three, and four orbits ago, respectively. The Sun is located in the center of the coordinate system. The dash-dotted line gives the position of the Galactic Plane, with the orientation is chosen such that it falls on the x -axis. The solid black line indicates the direction to the Sgr dwarf galaxy which also defined the zero direction of the longitudinal coordinate system, with the angle Λ_{\odot} increasing clockwise. To enhance the contrast in the regions of the Sgr debris, the innermost 20 kpc are not shown. Except for the ‘leading arm’, any data-model correspondence is not obvious.

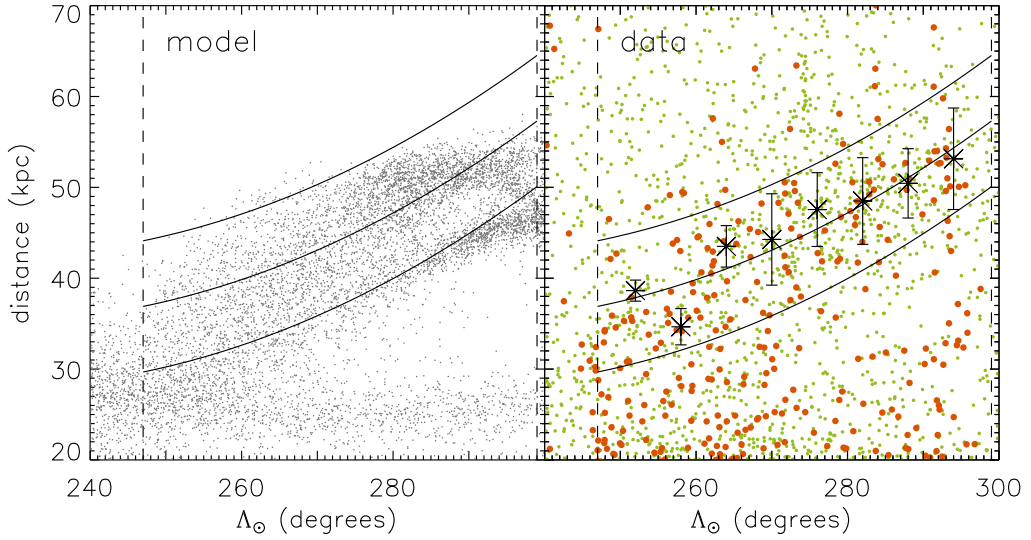


Figure 4.6: Heliocentric distance as a function of orbital longitude (see also the left column of Figure 4.10). In the left panel, the prolate model is shown as gray points. In the right panel, the data are shown with the small green points representing the photometric sample (limited to BHB probabilities $> 50\%$) and the larger orange points representing the BHB sub-sample with radial velocities. The result of the Gaussian fit to the red BHB stars in the sample (Figure 4.7) is shown as asterisks (mean distance) and ‘error bars’ (width σ). I fit the mean values with a second order polynomial function (central line) and take $\pm 2\sigma$ as my distance cuts (outer two lines). The dashed vertical lines mark the range in Λ_{\odot} over which the fit to the angle slices was performed. The orange dots falling within these outlines I denote as the kinematic BHB selection for Figure 4.11.

distribution in the models (with a prolate potential) is shown by the dashed-dotted line. The histogram is scaled down by a factor of seven to approximately match the number of stars in the data. The models show a bifurcation of the leading arm in distance between the debris lost in different orbits. I cannot see this in my data, the relative separation and size of the peaks are roughly of the same size as the fluctuations I see in the data in a typical angle slice. The results of the Gaussian fit are shown in Table 4.1 and Figure 4.6; crosses denote the mean value and the ‘error’ bars show the standard deviation σ around that mean.

I use these results as a first step in isolating a clean sample of BHB stars. A second-order polynomial is fit to the mean values, shown in Figure 4.6. I use this line, shifted by ± 2 times the mean standard deviation as borders within which I select leading arm member stars. In Section 4.3.5, I will refine this selection by taking into account an additional selection in velocity space. In the following I will use the spatially selected sample defined here since the kinematic selection also very strongly limits the sample size to stars which have radial velocity data available. The spatially selected sample will be limited to BHB star probabilities greater than 50%, whereas no probability cut is

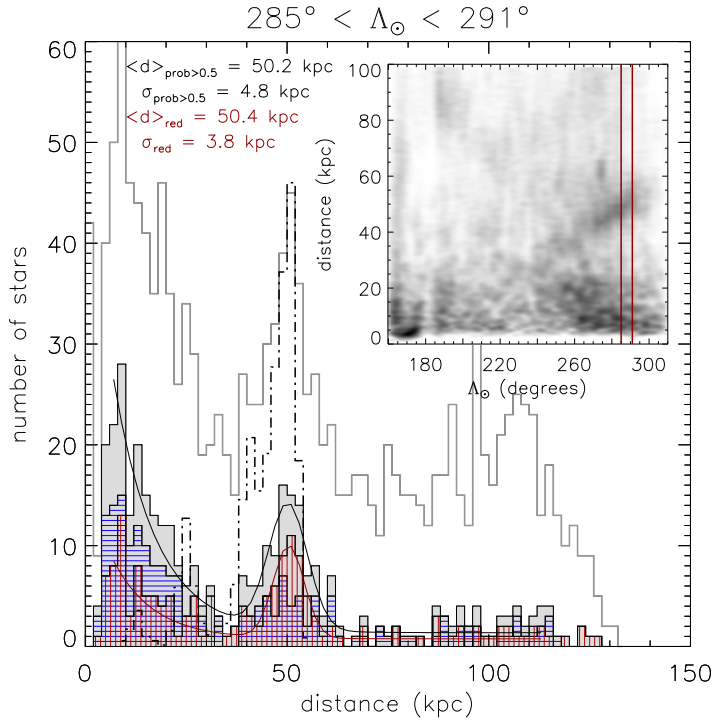


Figure 4.7: Distribution of heliocentric distances for 6° wide angle slice, $285^\circ < \Lambda_\odot < 291^\circ$, of Sgr's leading arm. The small panel on the upper right illustrates the angle slice used for this histogram. The full sample is denoted by the empty solid line histogram, while the gray histogram represents the sample with a $>50\%$ probability cut. A Gaussian has been fit to represent the stream stars in this subsample, while the fore-/back-ground has been fit by a power-law; the resulting distance and line-of-sight thickness are noted in the top left. Shown in the histogram filled with red vertical lines is the subsample of red BHB stars and shown in the one filled with blue horizontal lines is the subsample of blue BHB stars. The leading arm shows a slightly larger number of stars from the red subsample for all angles. The dash-dotted line shows the histogram for the prolate Law et al. (2005) model in the same angle slice. It has been scaled down to match approximately the number of objects in the data.

$\langle \Lambda_\odot \rangle$ (degree)	$\langle d \rangle_{\text{prob}>0.5}$ (kpc)	$\sigma_{\text{prob}>0.5}$ (kpc)	$\sigma_{\text{intr,prob}>0.5}$ (kpc)	$\langle d \rangle_{\text{red}}$ (kpc)	σ_{red} (kpc)	$\sigma_{\text{intr,red}}$ (kpc)
252	36.5	2.8	2.1	38.6	1.2	-
258	35.6	1.3	-	34.7	2.0	-
264	42.9	4.4	3.9	43.5	2.3	-
270	46.7	6.2	5.7	44.3	5.0	4.2
276	46.5	3.6	2.8	47.6	4.1	3.0
282	48.5	5.0	4.4	48.5	4.8	3.7
288	50.2	4.8	4.1	50.4	3.8	1.7
294	52.7	6.5	6.0	53.1	5.6	4.4

Table 4.1: Width of the leading arm: Results for the Gaussian fit to the leading arm. Mean $\langle d \rangle$ and standard deviation σ values are given both for the 50% probability sample and for the red subsample. I present also an estimate for the intrinsic width $\sigma_{\text{intr}} = \text{sqrt}(\sigma_{\text{obs}}^2 - (0.05\langle d \rangle)^2 - \sigma_{\text{bootstrap}}^2)$.

applied for the radial velocity sample since these stars are spectroscopically classified.

4.3.3 Bifurcation of the Leading Arm Perpendicular to the Plane

Following Yanny et al. (2009), I also look into the bifurcation of the leading arm as it was discovered by Belokurov et al. (2006a). When looking at thin distance slices of the SDSS using a population with a high abundance like MSTO stars one easily sees that the Sgr stream splits up into two parts. Given the relatively sparse distribution of BHB stars in the Sgr stream I use MSTO stars to define a selection for the two parts (see Figure 4.8). In my BHB star sample itself I do not see any indication for a bifurcation. Following Bell et al. (2008), I select MSTO stars in a color range of $0.2 < g-r < 0.4$ and a distance modulus range of $16.5 \leq m-M \leq 17.5$ assuming an absolute magnitude of $M_r = 4.5$. This corresponds to a distance range of 20–32 kpc. In Figure 4.8, I show the distribution of these MSTO stars. In the upper panels, I also show the distribution of the Sgr BHB stars as spatially selected from Figure 4.6. Note that the clearly identifiable part of the leading arm in BHB stars is not in the region on the sky where the bifurcation is most apparent. In the lower right panel, I illustrate the low density of BHB stars in the relevant distance slice (same distance modulus selection as for MSTO stars) with $\Lambda_{\odot} \lesssim 250^{\circ}$, which prevents us from investigating this part of the leading arm in BHB stars. Consequently, in the following I only study the leading arm for $\Lambda_{\odot} \gtrsim 250^{\circ}$. In Figure 4.9, I present measurements of the mean and width of the two branches in thin angle slices. Note that in contrast to Figure 4.6 this measurement was made on the pre-selected sample and not fitted to the data in the same fashion as illustrated in Figure 4.7. The two branches show similar distances with a 1-2 kpc variation in the mean distance values (see also Table 4.2 for a listing of the results). Several studies showed a systematic separation in the distance of the two branches, such that the high galactic latitude part of the stream is closer for most of the leading arm as seen in the SDSS. Yanny et al. (2009) report this offset in the distance distribution of BHB stars along the leading arm by visual impression. The same trend was also seen by Belokurov et al. (2006a) (results listed in Niederste-Ostholt et al., 2010), showing an offset of 2-3 kpc. An offset was also given by the Peñarrubia et al. (2010a) models for which I show the mean distances of the two branches in Figure 4.9, separated and measured in the same way as my data. Although I do not see a clear separation in distances in my data, the mean distances of the two branches and their relation to each other are sensitive to small changes in the separation cut between the two branches. Recently, Correnti et al. (2010)

Chapter 4 The Structure of the Sagittarius Stellar Stream

Table 4.2: Mean values with uncertainties and width for the two branches of the bifurcated stream as presented in Figure 4.9.

$\langle\Lambda_{\odot}\rangle$ (degree)	$\langle d \rangle_{high}$ (kpc)	σ_{high} (kpc)	$\langle d \rangle_{low}$ (kpc)	σ_{low} (kpc)
252	37.4 ± 1.4	3.9	36.8 ± 1.2	3.1
258	36.4 ± 1.9	4.0	37.2 ± 1.5	3.4
264	39.9 ± 0.8	3.9	41.4 ± 1.1	4.6
270	42.5 ± 0.8	3.6	42.9 ± 1.1	4.7
276	45.2 ± 0.7	3.9	47.6 ± 0.9	3.5
282	48.4 ± 0.9	4.3	48.4 ± 1.4	3.4
288	51.0 ± 0.6	3.7	50.3 ± 1.4	3.8

measured the distances of these two branches in Red Clump stars finding also only a small offset between them which is of a similar order as found in this study (see, e.g., their Figure 13).

4.3.4 Kinematics and Comparison to Models

To improve our understanding of the origin of overdense regions of the Sgr plane and the likelihood of those overdensities being associated with the Sgr system, I compare my data with models of the Sgr debris by Law et al. (2005), Law & Majewski (2010b), and Peñarrubia et al. (2010a). To complement my dataset with kinematic information, we use a sample of radial velocities determined from SDSS DR7 using the method of Xue et al. (2008) and Xue et al. (2010) (for an illustration of the spatial distribution of these stars with kinematic information in the Sgr plane, see Figures 4.10 and 4.6). The models are based on the 2MASS data set of M giants, see Figure 4.1 for their distribution. Figure 4.10 shows probability maps made in the same fashion as described above for both distance and velocity as a function of the orbital angle. In the three lower panels, I overplot the models by Law et al. (2005). From top to bottom, they show the tidal debris in a prolate, spherical, and oblate Galactic halo potential. In the third and fourth rows, two models using a triaxial halo potential are shown; in the fourth row the model from Law & Majewski (2010b) and the model by Peñarrubia et al. (2010a) in the third row which, in contrast to the other models, use a disk galaxy as a progenitor of the Sgr stellar stream. In the second row, a radial velocity sample of M giants (Majewski et al., 2004) is shown alongside with my BHB star data set. They cover mostly parts of the stream not covered by the SDSS.

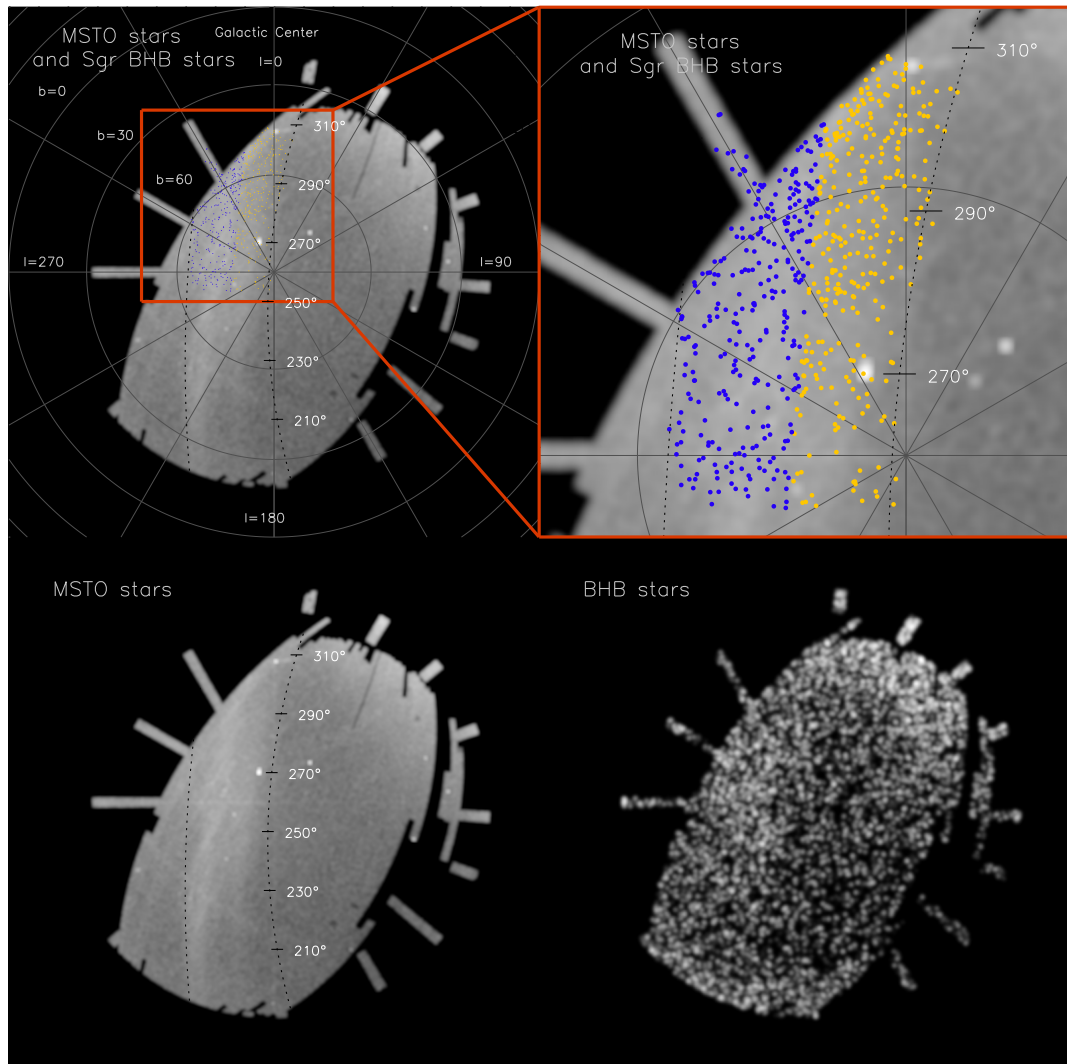


Figure 4.8: Map of the MSTO stars in a thick distance modulus slice, $16.5 \leq m-M \leq 17.5$, corresponding to a distance range of 20–32 kpc (left side and top right corner). The dotted black lines indicate the borders of the plane as this projection represents a side-view of this plane. The orbital angle Λ_{\odot} is given on the right of the plane segment. In the top panels, the BHB stars which were spatially selected as member stars of the leading arm are overplotted in yellow and blue. For better visibility, the area of interest (red box) is enlarged in the top right panel. The two colors denote the selection for the two parts of the arm following the appearance in MSTO stars. In the bottom right panel the BHB star distribution in the same distance shell is shown to illustrate why I can not select stars in the closer part of the stream where I see the strongest bifurcation in MSTO stars, as the BHB stars get much less abundant in the corresponding angle range (lower half of the plot).

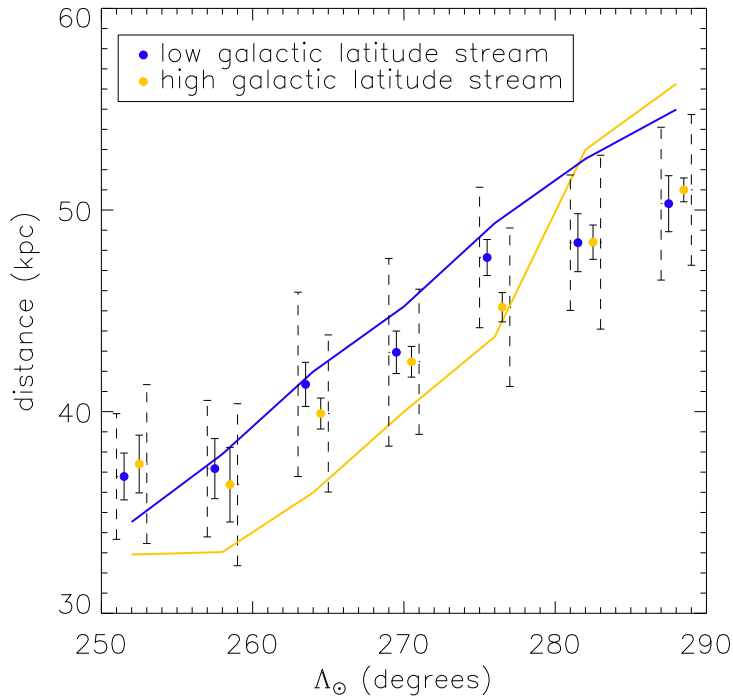


Figure 4.9: Mean distance and distance error corrected line-of-sight thickness of the two branches as determined from the spatially selected sample of Sgr BHB stars. Blue represents the branch at higher galactic latitude and yellow the one at lower galactic latitude (see also Figure 4.8). For presentation purposes, the points are offset by half a degree to the left and right, respectively. The uncertainty of the mean value determination is determined by bootstrapping and given by the solid errorbars. The dashed ‘errorbars’ represent the width of each substream, also corrected for the sample selection effects via bootstrapping. For better visibility, they are offset by another half a degree. The lines show the results of the same measurement on the Peñarrubia et al. (2010a) models. I do not see a clear trend in the distance offset of the two branches as in the models and the observed offset is much smaller than predicted by the models and seen in other analyses with different stellar populations (e.g., Niederste-Ostholt et al., 2010).

In the following, I compare the location of the predicted debris in the different models with my observations of the distribution of BHB stars. This comparison is merely meant to illustrate tentative agreements and disagreements between the models and the data with the goal of identifying features and regions of interest for further investigation, and not give a conclusive answer for a best model.

The prolate and triaxial models, which are shown in the third to fifth rows of Figure 4.10, clearly show the best consistency with the leading arm which is the most prominent part in the SDSS BHB sample (at an orbital angle of $230^\circ \lesssim \Lambda_\odot \lesssim 300^\circ$ and heliocentric distance between 20 and 60 kpc). On the other hand, the trailing arm from the Law et al. (2005) spherical and oblate models stretches out to larger distances than the prolate model, qualitatively (but not quantitatively) matching better the candidate Sgr debris shown in Figure 4.3⁴. The recent models by Peñarrubia et al. (2010a) show a trailing arm which stretches out to much larger distances than in the other models. Still, I do not see a good match with the observed overdensity. Correnti et al. (2010) report detection of a trailing arm segment in Red Clump stars which appears to be consistent with the prolate models around the crossing region of the leading and trailing arm in the range of $220^\circ \lesssim \Lambda_\odot \lesssim 290^\circ$. This feature is observed at much smaller distances than what is suggested here. I do not focus on this distance range here, as in at least my investigation I find a high degree of contamination from and/or cross-talk with the Virgo overdensity. If the detection of Correnti et al. (2010) is interpreted correctly as part of the trailing arm the overdensity seen here could possibly belong to a different trailing wrap.

Turning to the possible association of NGC 2419 with the candidate trailing arm debris, I note that the heliocentric radial velocity of NGC 2419 was measured by Peterson et al. (1986) to be -20 km s^{-1} which corresponds to a galactic standard of rest velocity of -14 km s^{-1} (Newberg et al., 2003). This corresponds well with the hypothesis that the cluster is a part of the trailing stream near its apogalacticon (Newberg et al., 2003). In addition, the properties of NGC 2419 are unusual in its own right (e.g., Dalessandro et al., 2008): it is very luminous with $M_V \sim -9.5$ and has a large half-light radius $r_h \sim 25 \text{ pc}$ (Bellazzini, 2007), placing it in a region of radius–luminosity parameter space populated also by $\omega \text{ Cen}$ and M54, that have both been argued to be the stripped cores of dwarf galaxies (e.g., Sarajedini & Layden, 1995; Hilker & Richtler, 2000; Romano

⁴Part of the issue in reproducing such debris may be related to the distance offsets between the BHB stars and M giant tracers of the Sgr tail. The models were built to reproduce the smaller distances characteristic of the M giant tracers; I speculate that models reproducing better the leading arm in BHB stars would more easily yield a trailing arm consistent with the distant candidate Sgr debris.

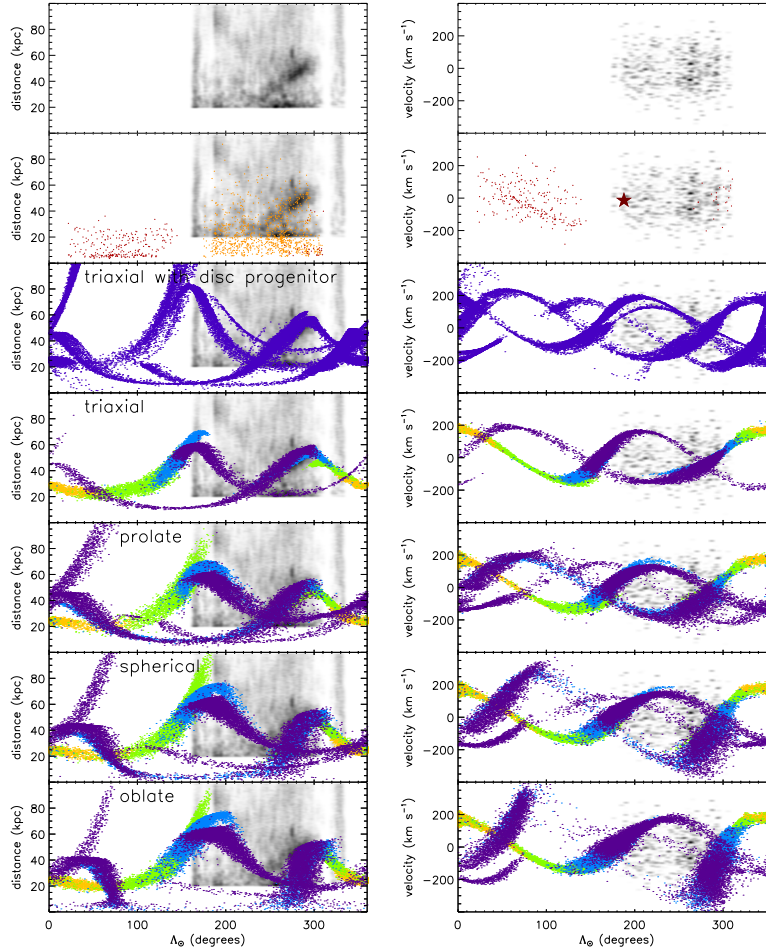


Figure 4.10: Distance and velocity of the Sgr stream for data and models as functions of orbital longitude. The upper row shows the data alone for stars within the Sgr orbital plane, analogous to Figure 4.3. The right column shows the distribution of measured heliocentric radial velocity in the Galactic standard of rest for the small subsample of BHB stars with SDSS spectroscopy. These data are repeated in the background of each row. In the second row from the top I show a sample of M giants with radial velocities from Majewski et al. (2004) in red (right, and the spatial distribution on the left), while I show the spatial distribution of my BHB star radial velocity sample in orange on the left. In the same row, the velocity of NGC 2419 is represented by the dark red star. In the lower five rows, I show different models of the Sgr debris. In the third and fourth rows, the triaxial halo models by Law & Majewski (2010b) and Peñarrubia et al. (2010a) are shown. The fifth through seventh panels show the models by Law et al. (2005) using different halo potentials: prolate, spherical, and oblate. The different colors in the models show debris from different orbits (see Figure 4.5). Comparing the BHB star maps with the models I see the best match for the leading arm region in the triaxial and prolate models for the spatial distribution. Although the radial velocity map does not resemble very well what is expected by the models, the main overdensities are also best covered by the triaxial and prolate models. Apart from the leading arm there is no good match between *any* of the models and the data. The overdensities in BHB stars seen at distances between ~ 50 and 90 kpc is not reproduced quantitatively by the models, nor do I see overdensities in the regions the models predict for the trailing arm.

et al., 2007; Bellazzini et al., 2008; Georgiev et al., 2009). Yet, the situation with NGC 2419 in particular is not clear cut. There is no evidence of multiple stellar populations in NGC 2419 (Cohen et al., 2010), in apparent contrast with the properties of, e.g., ω Cen (e.g., Ripepi et al., 2007; Sandquist & Hess, 2008). Furthermore, Casetti-Dinescu et al. (2009) have calculated a preliminary orbit for the Virgo stellar overdensity, finding that it is very eccentric, and they suggest that NGC 2419 may in fact be associated with the Virgo stellar overdensity rather than Sgr. Furthermore, I do not see a clear velocity signature of trailing debris in the SDSS velocities (although it is unclear if a signature is expected in the sparsely-sampled SDSS BHB velocity data set). Finally, the updated models of Law & Majewski (2010b) in a triaxial potential show an *increased* inconsistency with NGC 2419 as described by Law & Majewski (2010a).

Although the full velocity sample as I show it in this plot does not show a very clear signal for the prominent leading arm, it is still obvious that the main overdensities ($240^\circ \lesssim \Lambda_\odot \lesssim 300^\circ$) agree best with the models for the prolate and triaxial versions. This will become clearer when I restrict the velocity sample to stars within the region of the leading arm in distance space in the next section.

A serious inconsistency with the models can be seen in the region where the trailing arm is predicted to stretch into the region covered by the SDSS (around $(-60,0)$ and upwards in Figure 4.5). In the data I do not see a signal which would come anywhere near the intensity which is predicted by the models for this part of the arm. The absence of such a counterpart indicates a serious problem with the models. This can not be explained through differences in the stellar populations in the debris; the models predict this part to consist of stars that got unbound in the same orbits as the debris in the part of the leading arm that can be observed in the SDSS. I speculate that this discrepancy may be alleviated in models tuned to reproduce better the distances of the leading arm as traced by the BHB stars.

In the following section, I attempt to measure the velocity spread of the Sagittarius stellar stream. I continue my attempt to isolate a ‘clean’ sample of stars most likely belonging to the Sagittarius stellar stream. I use both positions and kinematics to achieve a high reliability of my selection. However, the size and distribution of the radial velocity sample limit this selection strongly.

$\langle\Lambda_{\odot}\rangle$ (degree)	$\langle\text{RV}_{\text{gal}}\rangle$ (km/s)	σ_{obs} (km/s)	σ_{intr} (km/s)
254	-76.2	40.7	35.3
264	-28.4	100.7	98.3
274	-27.6	92.8	88.1
284	-5.7	37.3	35.8
294	24.6	43.3	40.2

Table 4.3: Radial velocities of the leading arm: Results for the Gaussian fit to the radial velocity distribution of the leading arm sample. The intrinsic velocity spread is corrected for the radial velocity error and the sample composition in the bin (via bootstrapping).

4.3.5 Selection of a ‘Clean Sample’ of BHB Star Candidates

In this section, I continue my effort to select a ‘clean sample’ of Sgr BHB stars. In Section 4.3.2, I already made a spatial selection of the leading arm stars. In the following, I will restrict this selection to the radial velocity subsample to achieve a sample which follows the leading arm in both distance and velocity space. This selection of a ‘clean sample’ of Sgr BHB stars is based purely on the data, but agrees qualitatively in both distance and velocity space with the Law et al. models.

Figure 4.11 shows the radial velocity full sample (orange), with those lying in the distance selection in red. As can be seen in comparison with the models (in gray), the selected stars are mostly concentrated in an area quite consistent with the general trend of the model. I isolate candidate leading arm stars by taking angle slices in which I fit a Gaussian to the distribution of the distance-selected stars (red). Again I fit the mean values with a second-order polynomial function (see Table 4.3 for results). In Figure 4.12, I show the trends in distance and velocity, and their intrinsic dispersions, compared with the models with prolate and triaxial potentials. Stars lying within the distance selection, and within one mean standard deviation in either direction of the velocity fit are included in my ‘clean’ sample (see Table 4.4 for a full listing of the objects). When using this sample for further analysis one has to keep in mind that it is strongly restricted by the uneven coverage and magnitude distribution of the radial velocity sample.

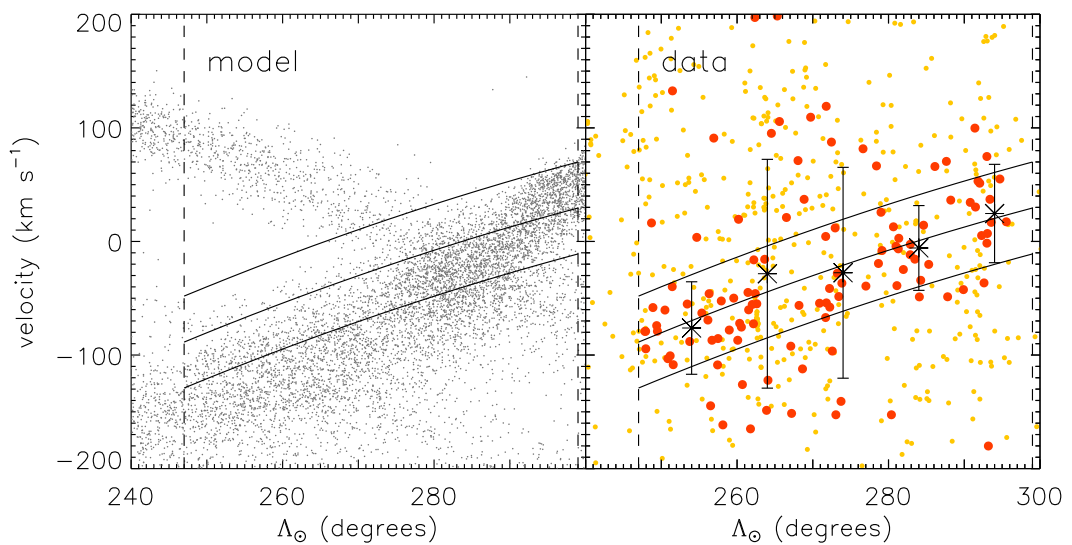


Figure 4.11: Heliocentric radial velocity in the Galactic standard of rest as a function of orbital longitude for the Law et al. (2005) prolate model and for BHB stars in the leading arm. The radial velocity sample of BHB stars is shown by the orange and red dots (right panel); big red symbols denote stars falling into the distance selection box of Figure 4.6 and small orange denotes everything falling outside this selection region. The majority of red dots follow roughly the trend indicated by the models (left panel). I fit the velocity distribution of red symbols with a Gaussian, using somewhat wider angle slices than before to account for the sparser sample. The mean and standard deviation of these fits are given by the asterisks and the bars (see also Table 4.3). I apply a second order polynomial fit to the mean values and shift this by the mean standard deviation in both directions to identify a selection area for the ‘clean’ sample.

Table 4.4: Sample selected for a high probability of association with Sagittarius.

R.A. (deg)	Decl. (deg)	l (deg)	b (deg)	g (mag)	$u-g$ (mag)	$g-r$ (mag)	P_{HBB}	HRV (km s ⁻¹)	HRVerr (km s ⁻¹)	RVgal (km s ⁻¹)	Fe/H	Fe/H error
149.31784	0.64158908	337.25807	59.124824	18.92	1.25	-0.09	0.68	-5.1	11.0	-38.9	-1.7	0.2
149.32185	0.82575434	340.25544	57.966839	19.20	1.19	-0.15	0.72	17.6	19.0	-11.7	-10.0	-10.0
151.66303	0.71303259	332.93978	60.252136	18.70	1.18	-0.06	0.44	65.9	11.0	25.7	-1.4	0.1
151.68573	0.83859047	336.16948	59.330910	19.52	1.05	-0.30	0.75	48.5	24.0	12.9	-10.0	-10.0
152.46681	0.72481130	354.09098	51.794464	19.15	1.21	-0.12	0.70	32.8	8.0	30.3	-1.2	0.1
152.73950	0.80837915	355.95736	50.489586	19.11	1.15	-0.19	0.61	5.2	21.0	7.0	-10.0	-10.0
162.91279	0.63505894	352.51890	50.663479	19.12	1.30	-0.17	0.05	11.9	8.0	5.2	-1.9	0.0
163.11225	0.80012300	355.61411	48.732353	19.11	1.20	-0.02	0.29	54.4	18.0	55.0	-10.0	-10.0
165.03563	0.82406409	291.64879	62.180853	18.84	1.29	-0.13	0.05	73.4	16.0	-16.2	-10.0	-10.0
165.26730	0.67366782	294.87797	62.247052	18.87	1.28	-0.02	0.05	71.1	7.0	-15.7	-1.9	0.1
171.35795	0.77705579	334.88970	58.104219	18.61	1.00	-0.02	0.09	42.4	11.0	2.8	-2.4	0.4
177.49904	0.69659886	355.65421	49.925343	18.97	1.18	-0.19	0.81	15.9	14.0	16.8	-10.0	-10.0
181.41167	0.68832934	292.43919	63.422670	18.86	1.20	-0.14	0.80	12.5	16.0	-72.5	-10.0	-10.0
181.54416	0.66210870	314.60980	63.437217	19.01	1.12	-0.13	0.41	7.7	11.0	-54.4	-1.5	0.1
181.57671	0.68079996	316.52701	63.065209	18.76	1.10	-0.19	0.34	6.4	7.0	-54.1	-1.7	0.0
185.50090	0.76998992	332.59194	60.542340	18.72	1.22	-0.19	0.87	20.9	17.0	-19.4	-10.0	-10.0
185.50929	0.83180709	333.63472	60.321873	18.94	1.22	-0.14	0.80	30.8	16.0	-8.0	-10.0	-10.0
185.13369	0.79081299	342.06521	57.760352	19.08	1.26	-0.06	0.58	10.2	18.0	-15.6	-10.0	-10.0
173.32034	1.2211629	359.16254	50.629827	19.09	1.24	-0.06	0.61	27.3	15.0	37.1	-10.0	-10.0
191.92214	1.1856847	353.74592	52.452357	19.20	1.25	-0.19	0.05	37.6	8.0	34.4	-1.7	0.5
192.82045	1.1740127	342.24188	58.467647	19.08	1.23	-0.15	0.90	22.3	18.0	-2.5	-10.0	-10.0
196.78478	1.0952469	353.51720	55.082748	19.13	1.16	-0.10	0.49	39.4	15.0	36.4	-10.0	-10.0
249.77752	-0.12263493	343.67858	60.877749	18.87	1.26	-0.05	0.05	15.5	14.0	-4.3	-1.3	0.0
236.23186	0.32725518	349.53368	58.140268	19.17	1.04	-0.14	0.04	24.6	18.0	14.3	-10.0	-10.0
247.67761	0.34199587	297.76277	68.420754	18.43	1.25	-0.14	0.89	19.0	13.0	-45.9	-2.2	0.1
195.51961	-0.73406591	258.01091	71.848421	18.38	1.18	-0.18	0.81	4.2	12.0	-58.2	-2.4	0.2
198.27333	-0.68782645	254.48333	72.188679	18.36	1.05	-0.21	0.30	-34.2	11.0	-94.5	-1.3	0.6
203.08792	-0.74637791	261.17467	74.794533	18.31	1.15	-0.11	0.16	-8.6	9.0	-60.4	-1.7	0.2
203.46564	-0.74396165	294.52133	78.208821	18.70	1.31	-0.13	0.05	-18.4	11.0	-52.4	-1.7	0.3
235.28992	-0.66049236	338.03357	68.100269	18.99	1.22	-0.19	0.87	-27.2	8.0	-48.5	-1.9	0.2
237.33833	-0.64090826	336.47791	68.325007	19.21	1.29	-0.13	0.05	35.0	8.0	11.9	-1.4	0.2
183.15324	-0.35575570	341.09162	68.226778	18.43	1.02	-0.01	0.09	-19.8	6.0	-36.7	-1.3	0.1

Table 4.4 (Continued)

R.A. (deg)	Decl. (deg)	l (deg)	b (deg)	g (mag)	$u-g$ (mag)	$g-r$ (mag)	P_{BHB}	HRV (km s^{-1})	HRVerr (km s^{-1})	RVgal (km s^{-1})	Fe/H	Fe/Herror
184.33572	-0.30121489	359.67778	59.904530	18.98	1.09	-0.21	0.63	-44.8	7.0	-34.2	-1.9	0.1
186.20173	-0.34449501	338.42710	69.530976	18.77	1.22	-0.17	0.90	-38.8	5.0	-57.8	-1.6	0.0
230.36425	-0.33667675	312.91600	77.668905	18.65	1.16	-0.08	0.41	-33.5	12.0	-60.2	-1.8	0.2
231.31942	-0.34046227	350.71450	70.209927	18.50	1.17	-0.05	0.44	-25.8	11.0	-28.0	-1.9	0.1
247.71507	-0.35833233	303.66505	76.708831	18.62	1.15	-0.20	0.66	-37.3	13.0	-72.1	-1.6	1.1
177.38054	0.15937633	281.06974	77.423385	18.41	1.21	-0.11	0.70	-22.3	10.0	-63.0	-2.4	0.4
213.82899	0.048201690	284.98406	76.767400	18.51	1.26	-0.21	0.82	-3.8	12.0	-46.0	-1.8	0.5
213.89940	0.18624951	300.73988	77.134295	18.58	1.16	-0.01	0.29	-15.0	9.0	-49.9	-1.3	0.3
214.76100	0.13294046	319.00435	77.535698	18.52	1.28	-0.25	0.05	-31.7	12.0	-54.9	-1.3	0.5
12.739674	15.849297	324.89192	85.302086	18.74	1.20	-0.22	0.79	-82.7	15.0	-85.5	-10.0	-10.0
21.239977	14.300256	293.68604	81.423698	18.51	1.27	-0.14	0.89	-64.0	9.0	-87.0	-1.0	0.1
11.571439	15.267388	322.21782	83.117026	18.43	1.15	-0.18	0.61	-69.6	5.0	-78.0	-2.3	0.1
37.994698	-9.4446953	322.70253	79.105115	18.51	1.19	-0.18	0.81	-38.3	9.0	-55.5	-1.8	0.0
62.479321	-6.3200403	256.52080	75.094461	18.11	1.07	-0.13	0.04	-24.1	8.0	-74.1	-2.0	0.0
40.554837	-8.7054956	260.66485	77.113803	17.92	1.15	-0.15	0.41	-60.3	7.0	-103.2	-1.8	0.1
42.311590	-8.4109077	260.92325	78.271266	18.15	1.19	-0.16	0.72	-62.2	6.0	-100.7	-1.8	0.1
181.39053	-3.3742984	279.90974	67.307502	18.24	1.21	-0.21	0.67	9.1	9.0	-69.2	-1.7	0.1
199.43635	-2.8485374	298.10400	74.487378	18.30	1.21	-0.13	0.80	-42.1	9.0	-87.0	-2.0	0.1
170.96747	-2.5415740	302.82768	75.868349	18.31	1.26	-0.16	0.91	-37.5	8.0	-75.4	-1.5	0.1
192.16892	-2.2424141	273.75164	68.019640	18.32	1.12	-0.24	0.70	-10.9	11.0	-88.1	-1.0	0.2
174.28068	-3.2210852	335.45465	68.964352	19.03	1.23	-0.23	0.83	-17.8	7.0	-41.4	-1.7	0.1
181.68676	-3.2304553	301.78123	73.471968	18.58	1.21	-0.07	0.61	1.2	3.0	-44.9	-1.7	0.1
184.50026	-2.7444692	261.08378	79.380844	18.25	1.10	-0.02	0.07	-5.6	11.0	-39.8	-1.7	0.1
185.92025	-2.8228684	245.46876	77.417677	17.96	1.22	-0.15	0.90	-40.7	3.0	-79.2	-1.8	0.1
188.14379	-2.8617039	245.13008	77.769645	18.28	1.21	-0.15	0.80	-42.0	4.0	-79.1	-1.4	0.1
187.30791	-2.7770480	249.11382	79.733714	18.85	1.18	-0.04	0.30	-48.0	20.0	-79.0	-10.0	-10.0
188.69635	-2.7577484	259.84128	80.889018	18.16	1.15	-0.17	0.42	-80.2	8.0	-108.5	-1.9	0.2
179.19443	-2.3958845	351.97783	50.812086	19.50	1.17	-0.27	0.68	59.3	13.0	51.3	-1.0	0.3
179.27744	-2.4873776	353.19843	50.061905	19.38	1.17	-0.20	0.81	3.7	11.0	-1.5	-2.0	0.2
182.51252	-2.2918592	326.21682	60.272876	18.84	1.22	-0.17	0.90	12.4	12.0	-39.3	-1.8	0.3
187.04228	-2.3998936	335.66563	58.430511	19.04	1.14	-0.20	0.66	31.2	13.0	-6.5	-10.0	-10.0
188.39442	-2.3430983	306.23529	62.775039	18.81	1.18	-0.08	0.41	17.7	11.0	-56.3	-1.5	0.2

Table 4.4 (Continued)

R.A. (deg)	Decl. (deg)	l (deg)	b (deg)	g (mag)	$u-g$ (mag)	$g-r$ (mag)	$P_{H/B}$	HRV (km s^{-1})	HRVerr (km s^{-1})	RVgal (km s^{-1})	Fe/H	Fe/H error
190.63810	-2.4297249	315.32404	62.568188	19.04	1.02	-0.21	0.25	67.7	6.0	4.4	-1.0	0.5
192.20784	-2.4226168	358.57367	48.349971	18.96	1.22	-0.14	0.80	9.0	18.0	17.3	-10.0	-10.0
172.36979	-1.4338628	272.87946	68.009004	18.48	1.24	-0.15	0.89	22.3	8.0	-55.1	-1.4	0.1
126.14404	46.955835	339.48188	55.003659	18.87	1.10	-0.12	0.06	13.8	14.0	-20.2	-10.0	-10.0
123.44799	46.625513	334.21365	57.176227	18.67	1.13	-0.03	0.19	17.5	14.0	-24.7	-1.6	0.0
140.29301	58.048908	351.40623	50.936195	19.12	1.33	-0.10	0.05	62.5	7.0	53.1	-1.4	0.1

Table 4.4: Sample selected for a high probability of association with Sagittarius.

4.4 Discussion and Conclusions

A number of previous works have explored the properties of the Sgr tidal debris using different stellar tracers, such as main-sequence turnoff stars, M giants, subgiant stars, or BHB stars. In this chapter, I have presented a discussion of the structure and properties of the Sagittarius stellar stream using candidate BHB stars selected from the SDSS coverage of the North Galactic Cap. BHB stars are in many senses an excellent tracer of tidal structure: they are luminous and can be traced to $> 100\text{kpc}$ distances from the Sun with current surveys; they are good standard candles with $\sim 5\%$ accurate distances; and although they are rather sparse compared to other stellar populations, they are still quite numerous in the Sgr tidal stream (with exception of the closest part of the leading arm as shown in Figure 4.8). Recently, there have been a number of Sgr stellar stream studies (e.g., Yanny et al., 2009; Niederste-Ostholt et al., 2010; Correnti et al., 2010) also based on various stellar populations, some including BHB stars in SDSS.

In contrast to those studies, I entirely focus on BHB stars for the analysis, using other data only to relate my distance scale to other distance indicators. I attempt to use as pure a sample of BHB star candidates as is possible for my analysis, minimizing to the greatest extent possible the high levels of contamination seen in earlier studies. For charting out the global structure of the Sgr tidal stream I make use of a method (described in Chapter 4) that selects BHB stars from SDSS imaging data using a spectroscopic training set to isolate areas of ugr color space that give a sample that should consist of $\sim 70\%$ BHB stars. This method does not just make binary acceptance or rejection decisions based on the position in color-space, but assign probabilities to the stars based on their position in color space. In my analysis I mostly reject stars with probabilities $< 50\%$ and make use of the probability information for the remaining sample by weighting the individual stars by their probabilities.

I evaluate the precision of my distance determination through comparison with distance measurements of known clusters and dwarf spheroidals. I see an offset in the mean values of $\sim 4\%$ for the literature values, and a distance variance of $\sim 5\%$. Comparison to the M giants in the Sgr orbital plane implies that the M giant distances should be revised upward by 8% or 12% when compared with my BHB scale or the cluster distance scale in the literature, respectively. The offset to the previously adopted M giant distance scale is expected to propagate through to the models built to match the M giant observations (e.g., Law et al., 2005; Law & Majewski, 2010b). When studying the kinematics of the Sgr tidal tail, I focus on a sample of stars with SDSS DR7 spectroscopy

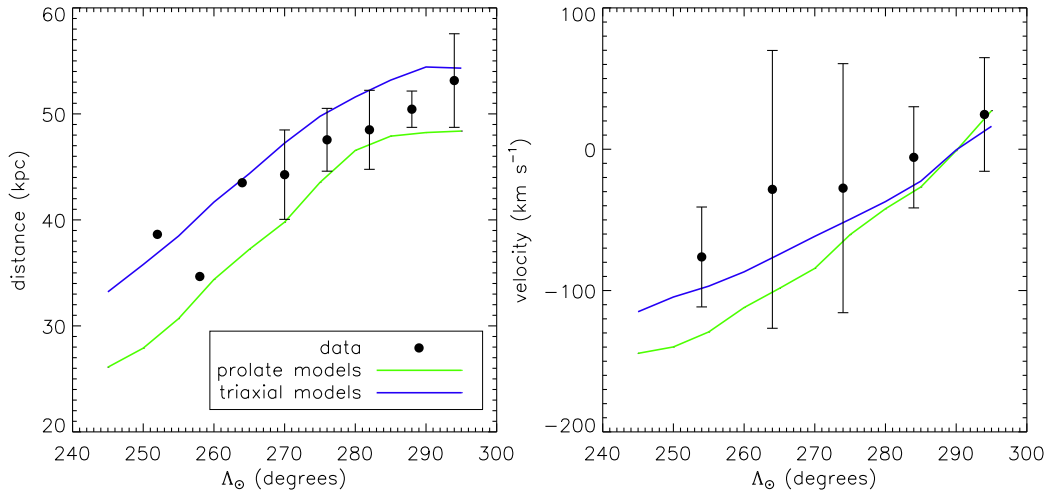


Figure 4.12: Distance and velocity dispersions of data from the spatial and kinematic selections for the leading arm and models. The velocities are again given in the Galactic standard of rest. I only show the models for a prolate and triaxial potential (Majewski et al., 2004; Law & Majewski, 2010b) since these showed the best consistency with the properties of the leading arm. The data points represent the mean and width measurements (bars) as presented in Figures 4.6 and 4.11, showing a fit to the total sample on the left and the spatially selected sub-sample on the right. The data are corrected for distance uncertainties and for uncertainties resulting from the sample selection in the bins by bootstrapping. For some bins these uncertainties are too large to resolve the intrinsic width of the stream.

classified as BHB stars using the method of Sirko et al. (2004) and Xue et al. (2008); this sample should be $> 90\%$ BHB stars.

With these samples, I focus on four Sgr stream issues that are not well-explored in the literature: a possible extension of the trailing Sgr debris stream, the line-of-sight thickness of the leading tail, the bifurcation of the leading arm and the heliocentric distances of the two branches in BHB stars and the isolation of a small sample of high-probability Sgr member stars.

Using the photometric sample with a $> 50\%$ BHB probability limitation, I identify a possible extension to the trailing tail of the Sgr debris stream to 60–80 kpc. The densest part of this feature, which coincides spatially with the globular cluster NGC 2419, was previously argued to be associated with the Sgr trailing arm by Newberg et al. (2003). My BHB star maps confirm a weak overdensity which may be the extension of this arm back towards the Milky Way, which was also seen by Newberg et al. (2003, 2007). I estimate the significance of this feature to be around 3.8σ as compared to random selections of the same area within a region spanning the angular range and distance of the proposed trailing arm. A concentration in this region, which is claimed to be associated with the trailing arm of Sgr was also found by Sharma et al. (2010) in 2MASS

M giants through a group finding technique. Such a feature is expected qualitatively by models of Sgr disruption. Quantitatively, all models predict that this ‘returning’ segment of the trailing arm should be closer to the Sun along these lines of sight. Yet, BHB stars are *not* observed at these predicted distances, and this tension would be resolved if one instead interpreted this distant overdensity as this predicted part of the trailing Sgr arm and acknowledges a discrepancy between the positions predicted by the models and the observed location. In this context it is worth noting that recently Correnti et al. (2010) reported an overdensity in Red Clump stars consistent with the predicted trailing arm location in the prolate models in a range of $220^\circ \lesssim \Lambda_\odot \lesssim 290^\circ$. Owing to confusion between Sgr and Virgo overdensity debris at the distance ranges probed by Correnti et al. (2010), I were unable to confirm or refute this feature. If their feature is indeed correctly interpreted as trailing arm debris, I would suggest the feature identified here may be another, more distant wrap of trailing arm debris from an earlier close passage of Sgr.

I use the $> 50\%$ probability sample to characterize the leading arm of the Sgr stellar stream more closely by measuring the line-of-sight thickness and selecting a high-probability sample of member stars. I find a mean thickness of ~ 3 kpc, after accounting for distance uncertainties in the BHB stars⁵, comparable to the projected width of Sgr on the sky. These measurements are in a similar range as those given by Correnti et al. (2010) in Red Clump stars (their Table 2), when the assumed overestimation by a factor of $\gtrsim 2$ which is introduced by their measurement method is taken into account. Inspired by the clear appearance of the leading arm in position (and velocity), I use this measurement of the line-of-sight thickness to select a sample of highly likely stream stars from the spectroscopic SDSS sample. I choose stars within 2σ of the stream in line-of-sight distance. This subsample of stars shows a clear overdensity in velocity space, which matches model predictions reasonably well. This strengthens the results of Yanny et al. (2009) who showed that BHB star candidates in the area selected to represent the spatial position of the leading arm in K/M-giants were overdense in velocity space. They find a similar trend in velocity space, but with far more outliers, probably due to the higher level of contamination in the BHB star sample and the broader selection box for the leading arm. From my spatially selected sample, I measure an average velocity dispersion of Sgr stars of 37 km s^{-1} . I further select stars within 1σ of this velocity overdensity to

⁵Note that I only take into account the uncertainties estimated on single metallicity populations and not the additional uncertainty introduced by having a variety of metallicities. This would cause an underestimation of the distance uncertainty, which would result in an overestimation of the thickness of the arm.

be in my 'clean' sample of ~ 70 Sgr BHB stars; such a sample suffers from the inhomogeneous angle coverage and distance limitations inherent to spectroscopically-selected SDSS BHB stars, but has the advantage of high fidelity.

Using the spatially selected Sgr BHB star sample I examine the observed bifurcation of the Sgr stream on the sky and its implications for the distances of the two branches. Different distances of the two branches of the stream have been reported by e.g., Belokurov et al. (2006a), Yanny et al. (2009) and Niederste-Ostholt et al. (2010) and are also predicted by models (Peñarrubia et al., 2010a). This bifurcation is of particular interest for the understanding of the formation history of the Sgr stream. It has been a challenge for models to reproduce and explain the origin of this feature. It was proposed to have originated from wraps of different age (Fellhauer et al., 2006), but also intrinsic properties of the progenitor were offered as explanations. Recently, Peñarrubia et al. (2010a) presented a model in which this bifurcation is reproduced when a rotating disk galaxy is assumed as the progenitor. There is no indication of a spatial bifurcation on the sky in my BHB star sample therefore I use MSTO stars to define the two branches on the sky. I measure the mean and width of the two parts along the leading arm and find only a small 1-2 kpc offset between the two branches over a wide orbital angle range and no clear systematic separation in the sense that one is always clearly closer in than the other (c.f. Yanny et al., 2009; Correnti et al., 2010). Yanny et al. (2009) reported a trend by visual impression that the branch at higher galactic latitude tends to be at closer distances than the branch at lower galactic latitude. Correnti et al. (2010) found similar to slightly higher offsets between the distances of the two branches compared to this study, but here again no clear trend is seen for one branch being always at closer distances than the other. Although the actual values for mean distances of the two branches in my data set seem to be quite sensitive to the precise location of the separation cut on the sky, I clearly do not see a separation on the level shown in Niederste-Ostholt et al. (2010) for the same range of positions along the stream or predicted by the models (Peñarrubia et al., 2010a). It is worth noting that this distance separation appears here to be much smaller than the separation of the two branches on the sky which is at a 10° level. This strong discrepancy between the small line-of-sight separation and the much larger separation perpendicular to that might be challenging to reproduce in the models.

Part II

Studying the Formation of the Elliptical Galaxy Population

PRELIMINARY NOTE

An early version of the project presented in the following chapter has been published in my diploma thesis. During the PhD the analysis and presentation was modified, improved and extended. Here, I want to give a short overview of the main alternations from the diploma thesis version:

Sample Size: The spectroscopic redshift sample was significantly increased.

k-correction: For doing the k-corrections a different code was applied. An comparison between the results of the two codes is given.

Blue spheroids: An estimate of the blue spheroid fraction in the models was added.

Improvement of analysis: Overall the measurement techniques were improved. Among other things the selection cut was chosen in a more consistent manner.

Presentation: The text and discussion were significantly improved and extended.

5

THE EVOLUTION OF THE SCATTER OF THE COSMIC AVERAGE COLOR-MAGNITUDE RELATION: DEMONSTRATING CONSISTENCY WITH THE ONGOING FORMATION OF ELLIPTICAL GALAXIES

adapted from Ruhland et al. 2009, ApJ, 695, 1058

I PRESENT FIRST MEASUREMENTS of the evolution of the scatter of the cosmic average early-type galaxy color–magnitude relation (CMR) from $z = 1$ to the present day, finding that it is consistent with models in which galaxies are constantly being added to the red sequence through truncation of star formation in blue cloud galaxies. I used a sample of over 700 red sequence, structurally-selected early-type galaxies (defined to have Sérsic index > 2.5) with redshifts $0 < z < 1$ taken from the Extended Chandra Deep Field South (173 galaxies) and the Sloan Digital Sky Survey (550 galaxies), constructing rest-frame $U - V$ colors accurate to < 0.04 mag. I find that the scatter of the CMR of cosmic average early-type galaxies is ~ 0.1 mag in rest-frame $U - V$ color at $0.05 < z < 0.75$, and somewhat higher at $z = 1$. I compared these observations with a model in which new red sequence galaxies are being constantly added at the rate required to match the observed number density evolution, and found that this model predicts the correct CMR scatter and its evolution. Furthermore, this model predicts approximately the correct number density of ‘blue spheroids’ — structurally early-type galaxies with blue colors — albeit with considerable model dependence. Thus, I con-

clude that both the evolution of the number density and colors of the early-type galaxy population paint a consistent picture in which the early-type galaxy population grows significantly between $z = 1$ and the present day through the quenching of star formation in blue cloud galaxies.

5.1 Introduction

One of the best-known and most powerful scaling relations of the early-type (elliptical and lenticular) galaxy population is the systematic reddening of their colors with increasing luminosity: the color–magnitude relation (CMR). The slope of the CMR is driven by a correlation between metallicity and mass (Faber & Jackson, 1976; Kodama & Arimoto, 1997; Terlevich et al., 1999; Trager et al., 2000; Gallazzi et al., 2006), while the scatter is determined by scatter in both age and metallicity, where it is generally thought that age is the dominant driver (Bower et al., 1992; Trager et al., 2000; Gallazzi et al., 2006, although Trager et al., 2000 argue that an anticorrelation between age and metallicity keeps the scatter of the early-type galaxy scaling relations relatively modest while allowing significant scatter in both age and metallicity). The scatter in this correlation is relatively small (Baum, 1962; Visvanathan & Sandage, 1977; Bower et al., 1992; Terlevich et al., 2001; McIntosh et al., 2005b). Because the color of stellar populations is strongly affected by their ages and metallicities (Worthey, 1994), this correlation is a powerful probe of the formation and evolution of the stellar populations in early-type galaxies. The small intrinsic scatter found in some clusters (as little as $\sigma_{U-V} = 0.04$ mag in Virgo and Coma; Bower et al., 1992; Terlevich et al., 2001; although other clusters can have scatters approaching 0.1 mag; McIntosh et al., 2005b) gave considerable momentum to the notion that early-type galaxies formed the bulk of their stars at early times and that their stellar populations have aged essentially passively to the present day.

In the last few years, this position has been challenged by evidence from deep redshift surveys that the cosmic average red sequence galaxy population (i.e., averaged over all environments) builds up in stellar mass by roughly a factor of two over the interval $z = 1$ to $z = 0$ through the addition of new red sequence galaxies (Chen et al., 2003; Bell et al., 2004b; Cimatti, 2006; Brown et al., 2006; Faber et al., 2007; Scarlata et al., 2007, although some of the papers argue for a build-up in stellar mass only in galaxies with $\lesssim 10^{11} M_{\odot}$). These ‘new’ red sequence galaxies are the result of truncation of star formation in some fraction of the blue cloud population (Bell et al., 2007) through, e.g.,

galaxy-galaxy merging (Bell et al., 2004b; Faber et al., 2007; Hopkins et al., 2007) or environmental processes such as strangulation or ram-pressure stripping (e.g., Kodama & Smail, 2001).

Such a scenario makes strong predictions about what the scatter of the CMR and its evolution should be as a function of redshift (van Dokkum & Franx, 2001); to first order the scatter is expected to be constant with redshift. The object of this chapter is to quantitatively test this picture. I carefully measure the CMR evolution of galaxies selected to have concentrated light profiles and red colors — taken as a proxy for the early-type galaxy population — from $z = 1$ to the present day, and compare it to a toy model of a growing red sequence. I use the SDSS for the low-redshift CMR measurement, and a sample of galaxies with spectroscopic redshifts and accurate HST colors from the extended Chandra Deep Field South (CDFS hereafter) to probe the CMR out to $z = 1$. As it was *a priori* unclear how large the CMR scatter should have been, I adopted a conservative approach that optimized rest-frame color accuracy at the expense of sample size, choosing galaxies with spectroscopic redshifts and within relatively narrow redshift slices (to minimize k -correction uncertainties) and with color HST imaging (to minimize color measurement error). The data are described in §2. I describe the k -corrections and their uncertainties for the intermediate redshift sample in §3. I present my measurements of the intercepts and scatter of the CMR for color and structurally selected samples as a function of redshift in §4. In §5, I compare the observed results to stellar population models of increasing complexity, finally comparing it to a model for the growth of the red sequence through the truncation of star formation in blue cloud galaxies. I present my conclusions in §6. In what follows, I assume $\Omega_{m,0} = 0.3$, $\Omega_{\Lambda,0} = 0.7$, and $H_0 = 70 \text{ km s}^{-1} \text{ Mpc}^{-1}$ and a universally-applicable Kroupa (2001) stellar IMF for stellar population modeling.

5.2 Data

I use data from two different sources, depending on redshift. For galaxies with $0.5 < z < 1$, I choose to determine accurate colors for galaxies with spectroscopic redshifts in the HST/GEMS survey of the CDFS. This is crucial for minimizing the color measurement error, placing the strongest possible constraints on the intrinsic scatter of the CMR. To complement this dataset at low redshift, I use a sample drawn from the SDSS at $z = 0.05$.

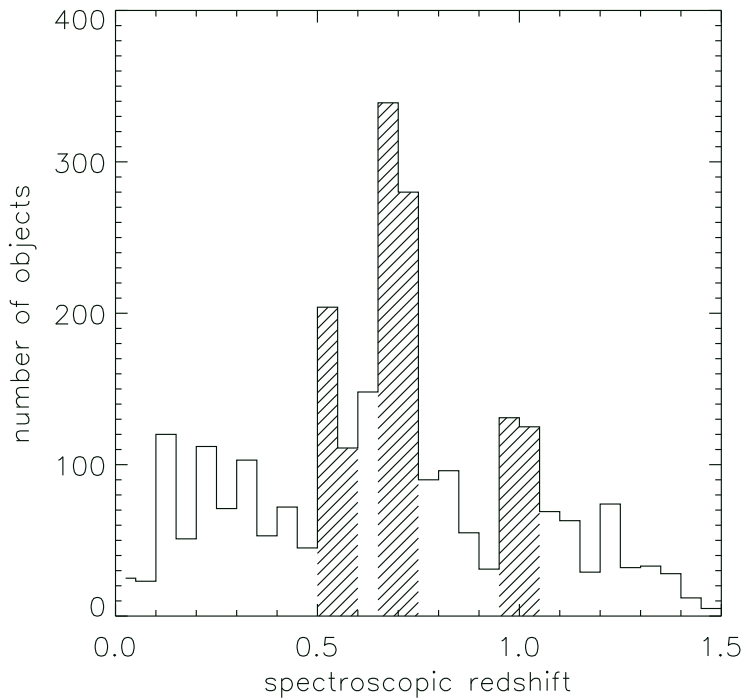


Figure 5.1: The distribution of the spectroscopic redshift samples for the intermediate-redshift range. I used galaxies with redshifts around 0.55, 0.7 and 1.0 as indicated by the shaded areas, in order to minimize the contribution of k -correction uncertainties to the CMR scatter.

5.2.1 Intermediate redshift data

For the intermediate redshift range, up to $z = 1$, I use data taken in the Extended Chandra Deep Field South (E-CDFS). A key ingredient is color HST imaging, taken from the GEMS¹ and GOODS² surveys. These data were used to estimate accurate galaxy colors within the half-light radius, and for selection by galaxy structure. A second key ingredient, required to make precise k -corrections, is accurate redshift measurements. For this investigation, a sample of objects with reliable spectroscopic redshifts was collected from a variety of sources. Insecure or uncertain spectroscopic redshifts were cross-checked with photometric redshifts from the COMBO-17³ survey. The spectroscopic selection criteria are described in the appendix and result in a final sample of 3440 galaxies with spectroscopic redshifts. I used 3030 galaxies in what follows; the remaining 410 objects could not be used either because they lacked data in one or more of the HST bands (211 galaxies), or because the object had a half-light radius smaller

¹Galaxy Evolution from Morphology and SEDs (Rix et al., 2004)

²Great Observatories Origins Deep Survey (Giavalisco et al., 2004)

³Classifying Objects by Medium-Band Observations in 17 Filters (Wolf et al., 2003, 2004)

than 2 pixels (204 objects and 5 objects satisfied both criteria). Figure 5.1 shows the redshift distribution of the 3030 useable objects. I choose the three best populated redshift bins of width $\Delta z = 0.1$ at $z \sim 0.55, 0.7$ and 1.0 for my analysis. I made this selection for two reasons. Firstly, the bins have to be quite narrow to minimize the contribution of k -correction (the wavelength range over which the interpolation must be done) uncertainties to the final error budget. Second, the best populated redshifts had to be used in order to obtain sufficiently populated CMDs for deriving CMR properties. In Figure 5.1 these redshift intervals are indicated by the shaded areas.

For further analysis, I rejected known IR and X-ray sources⁴. IR sources were identified by comparison with MIPS $24\mu\text{m}$ observations of the CDFS from Spitzer (Pavovich et al., 2004). I use the $24\mu\text{m}$ band owing to its high sensitivity to obscured star formation and AGN activity. The 80% completeness limit is $83\mu\text{Jy}$, corresponding to approximate obscured SFR limits of (5, 10, 17) $M_{\odot}\text{yr}^{-1}$ at redshifts of 0.55, 0.7 and 1.0 respectively (Bell et al., 2007) using a Kroupa (2001) IMF. I further excluded galaxies detected in deep Chandra imaging of the CDFS. The coverage is non-uniform, with an exposure time of 1Ms in the central pointing, and 250ks per pointing in each of 4 flanking fields. These depths are sufficient to detect moderate-luminosity AGNs ($L_{0.5-2\text{keV}} = 10^{41} - 10^{42} \text{ ergs s}^{-1}$) over the whole redshift range of interest (Lehmer et al., 2005).

Colors and magnitudes from GEMS Images

As the goal of this chapter was to measure the scatter of the CMR as accurately as possible, I use high accuracy HST colors for the construction of the CMR. For all objects with spectroscopic redshifts I used GEMS postage stamps to measure accurate magnitudes in the F606W and F850LP passbands. I used the GALAPAGOS⁵ software package to cut postage stamps around the position of each object. Galaxy properties were adopted from a single-component Sérsic model (Sérsic, 1968) fit to the 2-D galaxy luminosity profile using the package GALFIT (Peng et al., 2002). I estimate colors within the observed half-light radius (not the intrinsic half-light radius $r_{e,GALFIT}$ returned from fits to the light profile); such observed half-light radii are substantially larger than the intrinsic half-light radii for compact galaxies. I determined the observed half-light radius by

⁴Leaving in IR and X-ray sources gives similar results; I conservatively remove such sources in order to minimize the contribution of young stars and non-stellar light to the CMR scatter.

⁵Galaxy Analysis over Large Areas: Parameter Assessment by GALFITting Objects from SExtractor (M. Barden et al. in preparation)

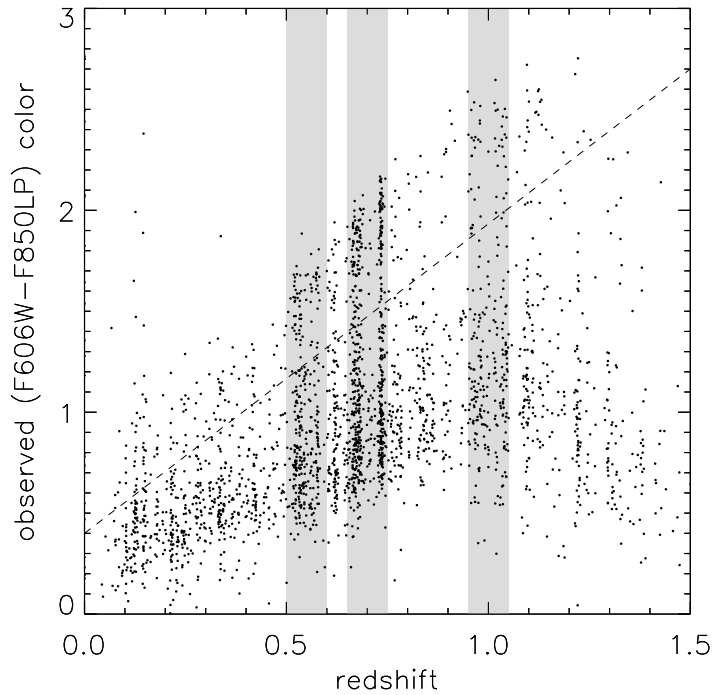


Figure 5.2: The observed F606W–F850LP color within the half light radius plotted as a function of redshift. The red sequence and blue cloud are clearly visible. The cut between the two populations is schematically indicated by the dashed line (this cut is only for illustration purposes and not used in what follows for any analysis; the actual redshift and magnitude-dependent cuts are given in Sec. 4.1). The gray shaded areas show the three redshift ranges used in this chapter.

performing aperture photometry in ellipses with the position angle and axis ratio given by GALFIT, out to $10r_{e,GALFIT}$ on the F850LP-band image. The *total* magnitude was defined as the aperture magnitude within $10r_{e,GALFIT}$. The observed half-light radius was then defined to be the semi-major axis of the ellipse within which half of the total light in F850LP was contained. In order to determine accurate F606W–F850LP colors, the F606W-image was convolved with a difference PSF, determined from the PSFs (Jahnke et al., 2004) in F606W and F850LP (the PSF correction was accurate to within 1 part in a million in terms of total flux on a pixel-by-pixel basis; see Häußler, 2007 section 4.2.2 for details), and the flux in F606W within the F850LP half-light ellipse was measured. Figure 5.2 shows the distribution of the measured colors against redshift. Uncertainties in the measured fluxes include contributions from Poisson uncertainty, read noise, and uncertainty from inaccuracies in the assumed sky level (this contribution is equal to the half-light area in pixels times the sky level uncertainty in counts per pixel). Typical values for uncertainties in the determined magnitudes are around 0.007 (slightly higher

for high redshifts and lower for smaller redshifts).

5.2.2 The low-redshift sample from the Sloan Digital Sky Survey

In order to explore the scatter of the CMR at low redshift, I use a sample of galaxies drawn from the Sloan Digital Sky Survey (SDSS) Data Release 4 (Adelman-McCarthy, 2006). I choose a sample of galaxies from the publicly-available New York University Value-Added Galaxy Catalog (NYU VAGC; Blanton et al., 2005) in a very narrow redshift range $0.0495 < z < 0.0505$ (2053 galaxies). To maximize the accuracy of the color information, I adopt colors derived from ‘Model’ magnitudes — such magnitudes use the best-fit de Vaucouleurs or exponential models in the r -band as a kernel for measuring fluxes in $ugriz$ ⁶. I k -correct the observed-frame $ugriz$ model colors to rest-frame $U - V$ color using InterRest (the same method I use for the intermediate redshift data; see Section 5.3). Rest-frame magnitudes were calculated by k -correcting Sérsic model magnitudes (Blanton et al., 2003a) from the NYU VAGC; such magnitudes are closer to the total magnitudes than Petrosian or Model magnitudes. The formal random error in the final $U - V$ color is < 0.02 mag from photometric error, with an estimated calibration error of < 0.04 mag (assuming 0.01 mag calibration errors in g and r bands); random errors in M_V are ~ 0.1 mag, dominated by systematic errors in how one defines sky levels and total magnitude.

5.3 *k*-corrections

To compare measurements in a redshift-independent manner, I k -correct the observed frame measurements into restframe properties (throughout this chapter I use $M_{V,rest}$ and $(U - V)_{rest}$ although my conclusions do not depend on this choice). To do so I use the IDL implemented restframe interpolation code InterRest by Edward N. Taylor⁷. To derive the redshift-dependent transformation between observed and rest-frame colors (the algorithm is described in more detail in Appendix C of Rudnick et al., 2003), InterRest uses observed SEDs from a set of template galaxies: four empirical model spectra from Coleman et al. (1980), and one additional starburst template from Kinney et al. (1996); this is a subset of the default template set which is used to avoid degeneracies in color space.

⁶I also used aperture magnitudes with aperture radii $5 < r/\text{arcsec} < 10$, finding similar or larger CMR scatter.

⁷<http://www.strw.leidenuniv.nl/~ent/InterRest>; this work is based on an earlier version of the code

These k -corrections were tested in two ways. Firstly, one can use the k -correction routine to predict a F775W magnitude for galaxies in GOODS (where one has F606W, F775W and F850LP). I show such a comparison in Fig. 5.3, where one can see that the k -corrections give a scatter of ~ 0.03 and an equal amount of mean color offset. Secondly, I can compare the final rest-frame colors to the results of independent k -correction codes. Comparison to (lower accuracy) COMBO-17 colors shows a scatter of 0.12 magnitudes and an offset of 0.06 mag, and comparison to a stellar population model-derived k -correction by Eric F. Bell and Boris Häußler shows measurement-to-measurement scatter of less than 0.02 mag but overall rest-frame color offsets of ~ 0.1 mag (this results primarily from a difference between the 4000Å break structure of the stellar population models and the observed ones used by InterRest). I conclude that the k -corrections of the HST-derived colors are accurate to a few hundredths of a magnitude (random error; this contributes to the scatter on the CMR; Taylor et al., 2009b), with possible overall systematics of $\lesssim 0.1$ mag (affecting primarily the zero-point of the CMR). I assume the k -correction errors to scale with the wavelength range over which the interpolation is done.

5.4 Results

In this section I present my analysis of the red sequence CMR scatter and its evolution. First, I explain the selection criteria applied for red sequence galaxies, then I discuss the actual measurement of the scatter of the red sequence at different redshifts $0.05 \leq z \leq 1.05$. With my precise magnitudes and colors I have produced color-magnitude diagrams (CMDs) for four redshift intervals and plot them in Figure 5.4.

5.4.1 Selection of Red Sequence Galaxies

My selection criteria take care to choose only non-star-forming, early-type galaxies representing the red sequence and to reject blue galaxies, galaxies with disk structure, and galaxies with ongoing star formation and/or AGN activity.

First, I applied a color cut to exclude galaxies with obvious signs of star formation from the sample. For this I made use of the bimodality of the color distribution which is visible in the CMDs at all redshifts (Figure 5.4). The color cut was chosen to fall into the gap between blue and red objects (see also histograms in Fig. 5.4). I used a tilted cut with the same slope for all samples. As the mean colors of the populations evolve

with redshift I take this into account by allowing the cut to evolve correspondingly. The cut applied here can be described as $(U - V)_{rest} > -0.085 \cdot M_{V,rest} - 0.65 - 0.5 \cdot z$. Small changes in the positions of the cuts do not influence the general results. In the diagrams the cut is made visible by different shades of gray. The light gray points are objects bluer than the color criterion whereas the dark gray and black points indicate objects on the red side of the cut.

A second selection criterion was applied to clean the sample of structurally late-type galaxies. For this the Sérsic index of the galaxy is used (for the GEMS galaxies, this is measured using GALFIT, while for the SDSS galaxies I adopt the Sérsic fits from Blanton et al., 2005). The Sérsic profile (or ‘generalized de Vaucouleurs law’, Sérsic, 1968) describes the surface brightness profile in dependence on the distance r from the center of a galaxy. The profile is given by $\Sigma(r) = \Sigma_e e^{-\kappa((r/r_e)^{1/n}-1)}$ with r_e being the effective radius and Σ_e the surface brightness at this radius. The Sérsic index n is a measure for the steepness of the profile where $n = 1$ provides a good description of disk galaxy profile (Freeman, 1970; de Jong, 1996). Higher values around $n = 4$ have been found to match elliptical galaxies and spheroidal systems like bulges in disk galaxies well. κ is set such that half of the flux is within r_e . To be treated as part of the red sequence a Sérsic index of $n > 2.5$ is required. This cut successfully weeds out edge-on spirals from the sample (McIntosh et al., 2005a). These objects are shown as dark gray points. Regardless of color and Sérsic index I reject galaxies with X-ray or $24\mu\text{m}$ detections (for the CDFS data only; the SDSS sample I use lacks such information) as their colors may be substantially affected by UV-bright young stellar populations and/or an accreting supermassive black hole (although my results remain unchanged if these systems are not excluded from my analysis). These objects are shown in the CMDs with asterisks (X-ray) and diamonds (IR). The objects which qualified as red sequence galaxies after these selection criteria are shown in black with error bars in the CMDs (number of RS galaxies in the redshift bins: 563/38/102/31).

5.4.2 Fitting the Red Sequence

The goal of this chapter is to measure the intercept of the CMR at a fiducial magnitude and its scatter, and to show the evolution of both the CMR intercept and scatter as a function of redshift (see Figure 5.4). The intercept is the color value of the relation measured at a specific magnitude (either the same magnitude value at all redshifts, or using a variable magnitude that attempts to account for the evolution of the population).

The scatter is calculated using the IDL routine *robust_sigma*, which gives an outlier-resistant estimate of the dispersion of the color distribution using the median absolute deviation as an initial estimate and then weights points using Tukey’s Biweight as a robust estimator (this is the usual approach employed in this field; e.g., Bower et al., 1992; McIntosh et al., 2005b). I fit a simple linear function to the distribution of colors and magnitudes of the non-star-forming early-type galaxies under two assumptions:

1. I fit the data points in each redshift bin separately.
2. I choose to hold the slope fixed at all redshifts ≥ 0.5 to the value measured at $z = 0.05$ from the SDSS.

The slope of the two methods are in some cases very different, but as the SDSS sample has many more objects and a larger dynamic range, this fit is much more reliable than the fits for the other bins. Further support for this assumed slope is given by the best populated GEMS bin around $z = 0.7$, which shows nearly the same slope. I note that the determination of the intercept and scatter are not sensitive to my choice of fitting method (Table 5.1)⁸. The histogram of color offsets from the CMR with redshift-independent slope is shown in the inset panels of Fig. 5.4 for early-type galaxies (black) and for all galaxies (gray). As the observed scatter contains contributions from intrinsic scatter and measurement uncertainty I estimate the intrinsic color scatter by subtracting the random color uncertainties in quadrature. The color uncertainties for the low redshift galaxies were estimated by scaling the Model $u-r$ color uncertainties⁹ by $d(U-V)_{rest}/d(u-r)$, and adding in quadrature a small empirically-determined 0.015 mag contribution accounting for real scatter in $U-V$ at a given $u-r$: $\delta(U-V)^2 = [\delta(u-r) \cdot d(U-V)/d(u-r)]^2 + 0.015^2$. If not further specified I refer to the intrinsic scatter hereafter.

⁸Furthermore the effect of excluding IR and X-ray detections from the red sequence is quite small and does not affect my results. The effect on the intercepts is around 1%. The values for intrinsic scatter would be a bit larger if IR and X-ray sources are included in the sample, changing for $z = 0.55$ from 0.128 to 0.138, for $z = 0.7$ from 0.126 to 0.133 and for $z = 1.0$ from 0.207 to 0.216.

⁹Recall that $U-V$ is estimated from the *ugriz* Model colors using InterRest. My choice of scaling from $u-r$ uncertainty is reasonable: u , g and r are the main determinants of $U-V$, where g and r are relatively well-measured and the u band uncertainty is factors of several larger.

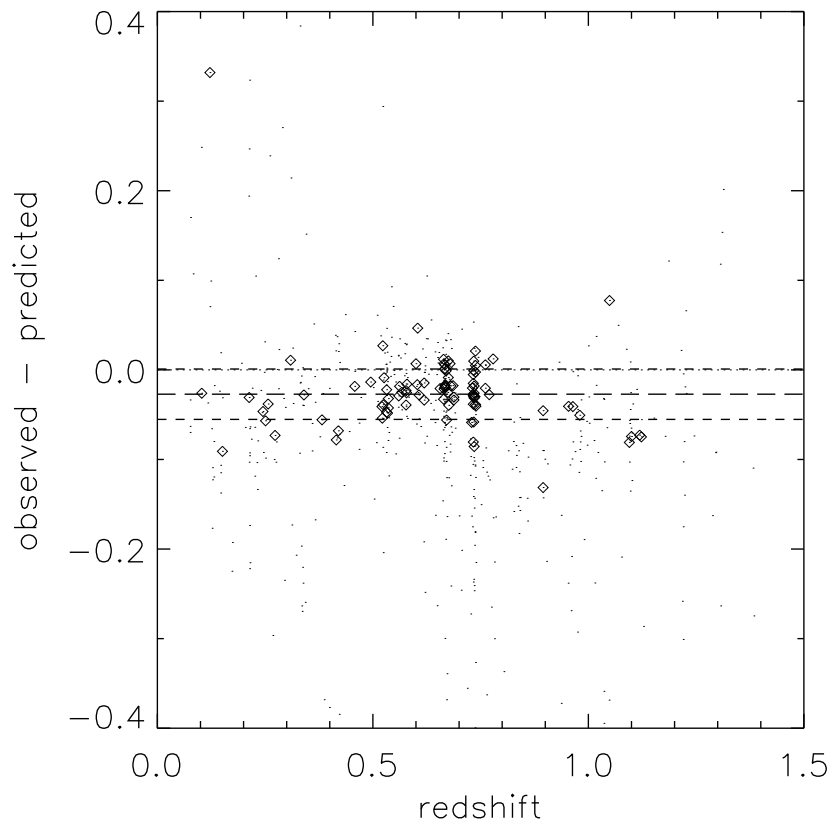


Figure 5.3: An assessment of the k -correction uncertainties through comparison of the observed F775W magnitude of those sample galaxies that overlap with the GOODS field and the F775W magnitude predicted using InterRest using only the redshift, F606W and F850LP magnitudes as input. In this plot I show the difference between measured and calculated magnitude in F775W as a function of redshift. The diamond symbols indicate red objects with a Sérsic index $n > 2.5$. The outlier at $z \sim 0.1$ is a composite merging system with both a dust-reddened and a blue component; such a composite system is too complicated to be described by the simple templates used here. The long dashed line shows the mean of these values and the short dashed lines show the RMS area around the mean value (both values are around 0.03). The random error serves as an approximation of the k -correction uncertainty.

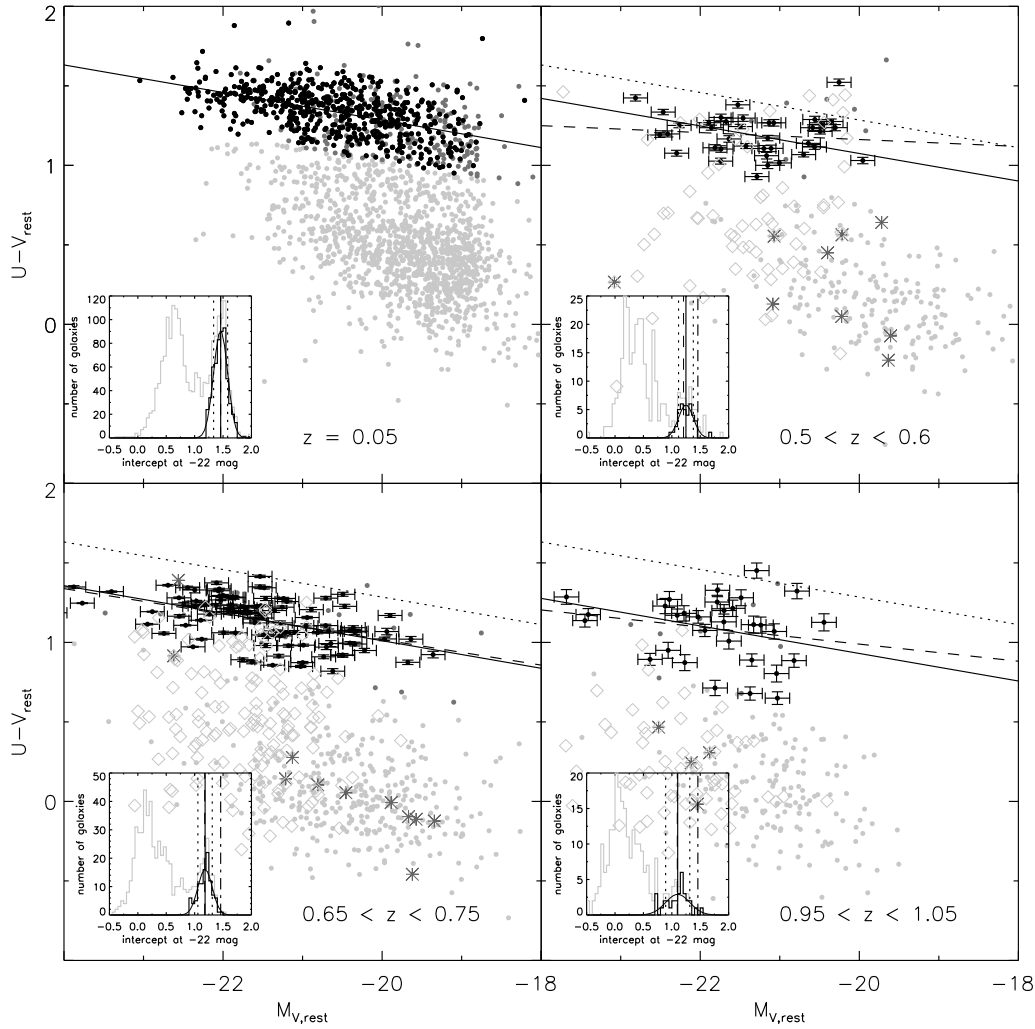


Figure 5.4: $U - V$ restframe color against M_V for four different redshift bins. The light gray points are objects below a tilted cut, dividing blue and red objects. This cut has a fixed slope and a redshift-dependent intercept. Depending on the Sérsic index the red objects are divided in a dark gray ($n < 2.5$) and a black sample ($n > 2.5$; with errorbars for the three intermediate redshift bins); the $n > 2.5$ red galaxies are retained in my analysis. Independent of color and Sérsic index IR (diamonds) and X-ray (asterisks) detections are rejected from the red sequence sample. The dashed lines are fits to the red sequence samples for the three redshift bins with $z \geq 0.5$. In the $z = 0.05$ panel the fit is shown as a solid line (the position of this fit is shown in the other panels as the dotted line). A line with the same slope is shifted to the mean color value of the three other panels (solid line). Using these ‘fits’ I calculated intercepts at $M_V = -22$. The small histograms show the color distribution measured as an offset from the relation. The complete distribution is shown in light gray, whereas the red sequence (the black points in the CMDs) is shown in black. The dashed vertical line shows the intercept of the fit (dashed line in the CMDs) at a magnitude value of -22 . The solid vertical line shows the mean intercepts with the CMR scatter (RMS) marked by the dotted vertical lines. The dash-dotted lines show the CMR intercept at $z = 0.05$. Overplotted is a Gaussian with mean and σ defined by the mean color and RMS of the red sequence sample.

	Fit				Fixed Slope			
	slope	intercept	measured scatter	intrinsic scatter	slope	intercept	measured scatter	intrinsic scatter
$z = 0.05$	-0.087 ± 0.006	1.457 ± 0.005	0.124	0.117	-0.087	1.457 ± 0.005	0.124	0.117
$z = 0.55$	-0.015 ± 0.028	1.206 ± 0.021	0.126	0.124		1.248 ± 0.022	0.130	0.129
$z = 0.70$	-0.066 ± 0.014	1.178 ± 0.010	0.127	0.127		1.184 ± 0.011	0.126	0.126
$z = 1.00$	0.010 ± 0.047	1.097 ± 0.041	0.210	0.206		1.103 ± 0.036	0.212	0.208

Table 5.1: Color intercepts (at $M_{V,rest} = -22$) and scatter in $(U - V)_{rest}$ measured with two different methods. ‘Fixed slope’ means that the slope of the CMR is fixed to the $z = 0.05$ value for all redshifts (solid lines in Fig. 5.4), while in the ‘Fit’ columns the red sequence is fitted for each bin (dashed lines in Fig. 5.4).

The color intercepts $(U - V)_{rest}$ of the fitted CMR at a fixed $M_{V,rest} = -22$ are shown as a function of redshift in Figure 5.5. The solid errorbars denote the formal error in the mean intercept, calculated using bootstrapping, although recall that the actual, primarily systematic, uncertainty in the galaxy colors is ~ 0.1 mag. The dotted ‘errorbars’ show my measurement of the CMR scatter, calculated as the resistant dispersion of the color offsets of the early-type galaxies from the CMR. The results are tabulated in Table 5.1. For comparison, intercept measurements from other studies (Blanton, 2006; Franzetti et al., 2007; Cool et al., 2006) are shown in this plot together with my data. In the case of Blanton (2006) and Cool et al. (2006), I have k -corrected their values to rest-frame $U - V$ color using the *kcorrect* software package, written by M. Blanton. I made sure that there is no significant difference ($\lesssim 0.03$ mag) between the rest-frame colors derived with *kcorrect* and *InterRest*.

I find that the intercept of the color-magnitude relation evolves by ~ 0.3 mag in $U - V$ color between $z = 1$ and $z = 0.05$, in rough agreement with previous studies (e.g. Bell et al., 2004a; Franzetti et al., 2007; Blanton, 2006; Taylor et al., 2009a), although recall that systematic errors in the intercepts of the CMR are significant, ~ 0.1 mag in $U - V$ rest-frame color. More importantly, I find a scatter of $\sigma_{U-V} \sim 0.1$ mag (Table 5.1) at all $z < 0.75$; the scatter at $z = 1$ appears to be somewhat larger (being consistent with Taylor et al., 2009a). These values are somewhat larger than the scatter measured for local galaxy clusters ($0.04 < \sigma_{U-V} < 0.1$, where the scatter appears to vary from cluster to cluster; e.g. McIntosh et al., 2005b)¹⁰. I note that subtraction in quadrature of the individual galaxy measurement errors from the CMR scatter yields almost unchanged results, even for the low redshift SDSS sample (where the scatter could decrease to ~ 0.09 mag). This shows that I measured a real scatter in the relation and not only a spread caused by measurement uncertainties. In particular, one should note that for the SDSS, spectral analysis of the drivers of the CMR scatter have demonstrated clear spectral differences between early-type galaxies of a given magnitude at the red side and blue side of the CMR (Gallazzi et al., 2006; Cool et al., 2006), demonstrating that the bulk of the CMR scatter is intrinsic.

¹⁰The possible trend towards a bluer CMR intercept at very large clustercentric radii, arguably an environmental effect, would also increase the scatter of the cosmic average CMR relative to the cluster CMR (e.g., Terlevich et al., 2001; Pimblet et al., 2002).

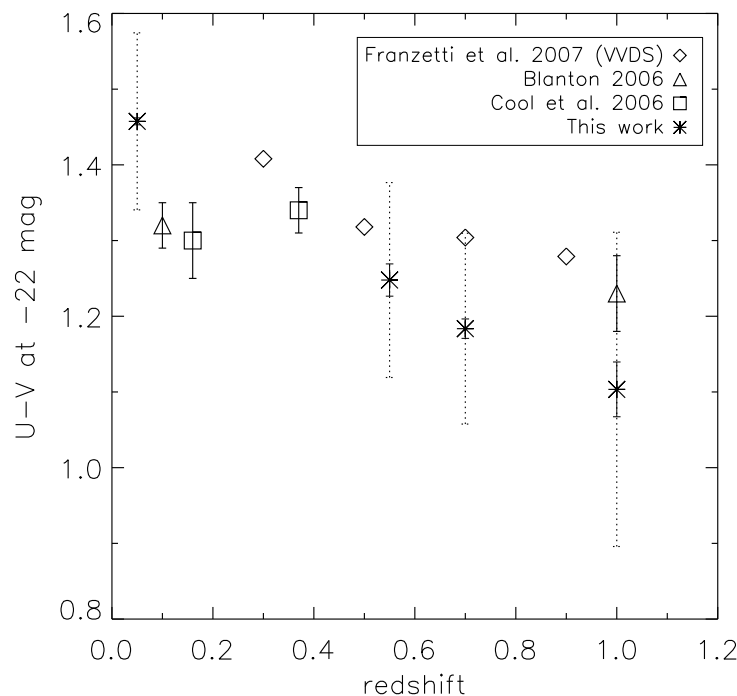


Figure 5.5: CMR intercepts in $U - V$ as a function of redshift. The small solid errorbars denote the standard deviation of all intercept values calculated with the bootstrap method. The ‘errorbars’ with dotted lines indicate the resistant dispersion of the color offsets from the best-fit CMR (i.e., the scatter of the CMR). The other symbols show measurements of the CMR intercepts from other papers, as explained in the legend. The measurements from Blanton and Cool were transformed into $U - V_{rest}$ using `kcorrect`. The errorbars reflect the uncertainties introduced by this treatment.

5.5 Interpretation

In the last sections, I described my measurements of the CMR intercept and scatter for cosmic average early-type galaxies at four redshifts between 1.0 and 0.05. I find a slowly-evolving mean color, and an almost non-evolving scatter of ~ 0.1 mag in $U - V$ rest-frame color. In this section, I build some intuition about possible interpretation of this result using stellar population synthesis modeling. I show first the evolution of single bursts, or populations of galaxies whose star formation is truncated at a particular time, in §5.1 and 5.2. Note that the purpose here is not to test ‘monolithic collapse’ models (those models are already ruled out by the observed build up of the red sequence population), rather it is to establish the basic model ingredients. In §5.3 and 5.4 I ask and answer a simple question (similar in spirit to van Dokkum & Franx, 2001): if the red sequence forms through ongoing and continuous truncation of star formation in previously star-forming systems, can one simultaneously reproduce the build-up of red

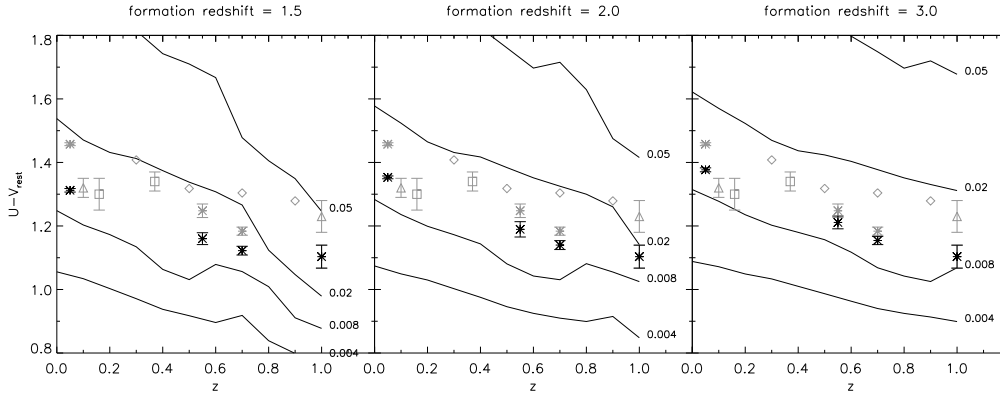


Figure 5.6: The evolution in rest-frame color of single-burst stellar populations formed at three different redshifts, and with different metallicities (where $Z = 0.02$ is solar metallicity). The asterisks denote the measured intercepts from this study; the gray asterisks are the same as in Fig. 5.5, whereas the black asterisks show color intercepts measured at a redshift-dependent absolute magnitude (to compensate for fading of stellar populations as the galaxy population ages; one can think of this as measuring the intercept at approximately constant stellar mass). The other gray symbols show data from other papers, measured in a similar fashion to my gray data points (see the legends of Fig. 5.5 or 5.7).

sequence galaxies and the scatter of the CMR?

5.5.1 The evolution of single bursts

To get my bearings, I focus first on the evolution of the CMR intercept using single bursts of star formation. In what follows, I use the stellar population model PÉGASE¹¹ (Version 2.0, see Fioc & Rocca-Volmerange, 1997, for the description of an earlier version of the model) to predict the evolution of galaxy colors and absolute magnitudes as a function of redshift.

The results are shown in Figure 5.6 for three different formation redshifts and for various metallicities. One can see that the evolution of the intercept of the CMR follows roughly the trends expected for the passive reddening and fading of ancient stellar populations. In the context of single bursts, the rate of change of the CMR intercept with redshift is related primarily to formation history, whereas the overall intercept is sensitive primarily to metallicity, with some sensitivity to age.

To compensate for the passive fading of the early-type population, I also measure the CMR intercept at a *redshift-dependent* absolute magnitude (black asterisks in Figure 5.6). I choose to adopt a model with metallicity $Z = 0.008$ and a formation redshift of

¹¹Projet d'Etude des GALaxies par Synthèse Evolutive

2 to estimate the evolution of the luminosity of an early-type galaxy as a function of redshift¹², and use this to calculate the absolute magnitude values at which I measure the intercept of the CMR (these absolute magnitudes are -22 , -21.5 , -21.3 , and -20.8 at $z = 1.0$, 0.75 , 0.55 and 0.05 respectively). One can think of these intercepts as being measured at a given, redshift-independent, stellar mass. Because these intercepts reflect the evolution at a given stellar mass, I choose to focus on these values in what follows, as a more intuitive reflection of the likely evolution of the color of a given galaxy (or a mass/metallicity bin in the evolving galaxy population).

5.5.2 The evolution of galaxies with truncated star formation

Motivated by the observational evidence for truncation of star formation in blue sequence galaxies, leading to the ongoing build-up of the red sequence galaxies at redshifts $z < 1$ (e.g. Bell et al., 2004b; Borch et al., 2006; Bell et al., 2007; Brown et al., 2007), I study the evolution of the colors of galaxies whose star formation has been truncated at a variety of redshifts $z \lesssim 1$. The purpose of this section is to get a feeling for the ingredients used for the modeling of the CMR evolution described in the next section. Figure 5.7 shows the rest-frame color evolution of a stellar population which forms stars at a constant rate from $z_f = 2$ to the truncation redshift z_{trunc} . I plot the evolution of seven different truncation histories which all have a constant metallicity of $Z = 0.02$. The rightmost track has a truncation redshift very close to the formation redshift of the model, namely at $z = 1.95$. The other lines show the evolution of galaxies with smaller truncation redshifts (from left to right) from 0.2 to 1.2 in steps of 0.2 . A general feature of such truncation models is a period of relatively rapid evolution onto the red sequence (timescales $\lesssim 1$ Gyr, as can be seen in Fig. 5.7 and Blanton, 2006; Schweizer & Seitzer, 1992), and then relatively slow subsequent fading and reddening of the population.

5.5.3 Expectations for the Scatter Measurement

With these SF modeling ingredients in place, I am now in a position to ask what the evolution of the intercept and scatter of the CMR can tell us about the evolution of

¹²The choice between the formation redshifts in the range shown in the plot does not have a great influence on the results; to choose $z_f = 3$ instead would lead to a slightly smaller evolution in magnitudes, but the resulting difference in intercepts is smaller than 0.02 for all redshifts. A different choice in metallicity has also only very small effects. To choose $Z = 0.02$ (solar metallicity) would change the results even less than the change of formation redshift.

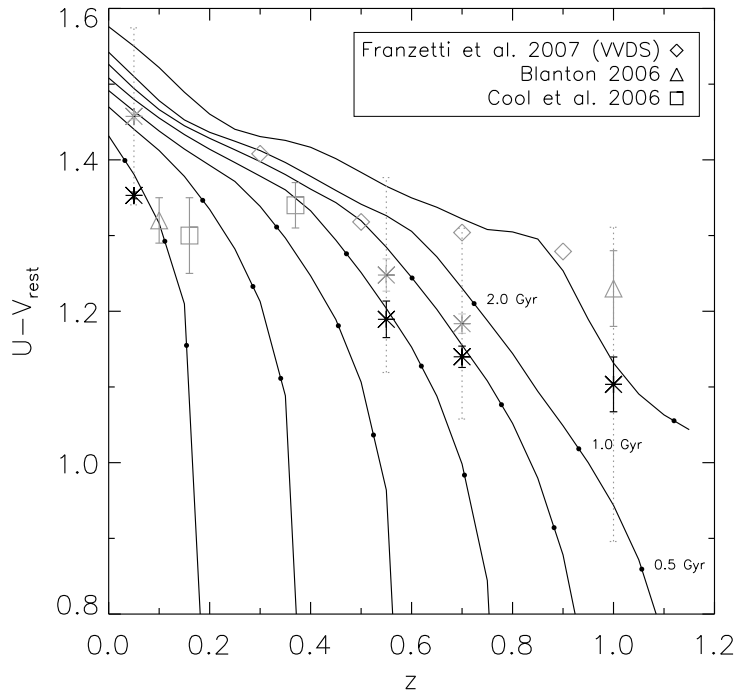


Figure 5.7: The redshift evolution of rest-frame color for different truncation times. For all lines, star formation starts at $z = 2$ and the different lines denote a variety of different truncation redshifts (from left to right: 0.2 to 1.2 in steps of 0.2). The tiny black dots on the lines indicate the point on the evolutionary track a galaxy has reached 0.5, 1 and 2 Gyr, respectively, after the truncation of star formation (as labeled on the second line from the right). The symbols are the same as in Figures 5.5 and 5.6.

the early-type galaxy population. Obviously, I will be unable to address this issue completely, as I have seen that many factors influence the colors and magnitudes of galaxies: when star formation started, metallicity, when (if!) star formation ends, and whether or not there is any residual star formation.

Instead, I limit myself to one well-defined question. Recent observations have measured a significant increase in the total stellar mass in the red sequence galaxy population since $z = 1$ (Chen et al., 2003; Bell et al., 2004b; Bundy et al., 2005; Brown et al., 2007; Borch et al., 2006; Faber et al., 2007). This evolution manifests itself primarily in terms of an increasing space density of red sequence galaxies at $\lesssim L^*$ (Borch et al., 2006; Faber et al., 2007), and is most naturally interpreted as being fed by the truncation or quenching of star formation in massive blue galaxies (Bell et al., 2004b, 2007; Faber et al., 2007). In such a scenario, one expects a significant scatter in the CMR, because of the constant flow of recently star-forming galaxies onto the red sequence. Here, I will predict the CMR scatter implied by a constantly growing red sequence, and compare

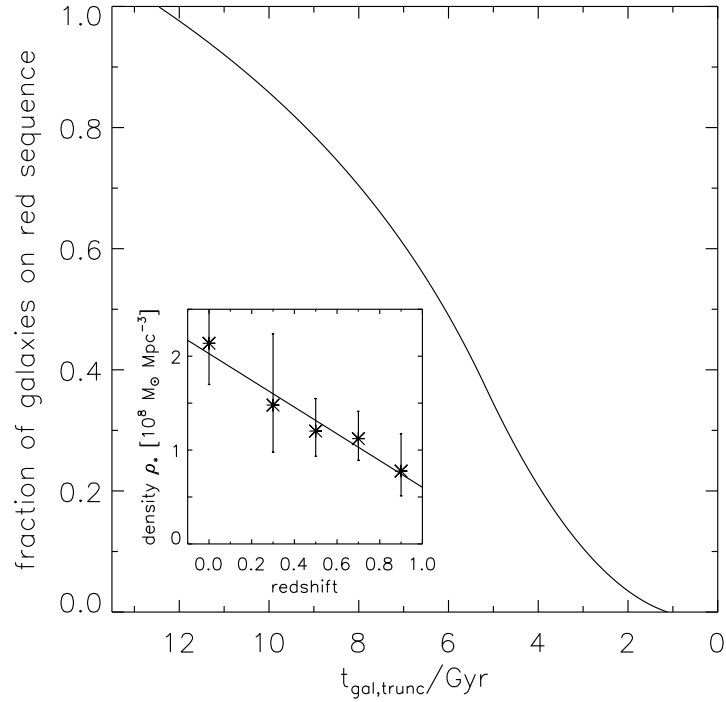


Figure 5.8: The integrated number of truncated (pre-red sequence) galaxies as a function of cosmic age ($t_{gal,trunc} = 13.5$ Gyr is the present day). Assuming that after truncation of star formation galaxies fade onto the red sequence in 1 Gyr, one reproduces (by construction) the observed evolution in stellar mass density on the red sequence (inset panel).

this predicted scatter with the observations. Such an exercise was carried out by van Dokkum & Franx (2001) for early-type galaxies in clusters; here, I extend their work to a cosmic average environment.

My first ingredient is a toy model for the build up in the number of red sequence galaxies as a function of time. I assume i) that the growth in the total mass on the red sequence is driven entirely by adding blue galaxies that have had their SF recently truncated, and ii) red sequence galaxies are added at all stellar masses equally¹³. I describe the evolution of the number of red sequence galaxies with a simple linear fit (in redshift) as shown in the small panel of Fig. 5.8, compared with the measurements of the integrated stellar mass density of Borch et al. (2006). I then determine the derivative of this relation to get the change in stellar mass density with time. This is used to estimate the *truncation rate* by shifting the time axis by -1 Gyr - approximately the time taken to redden enough to satisfy my red sequence cut (following Blanton, 2006;

¹³In fact the CMR scatter and mass build-up are both measured at $\sim 10^{11} M_{\odot}$, reducing the importance of this assumption.

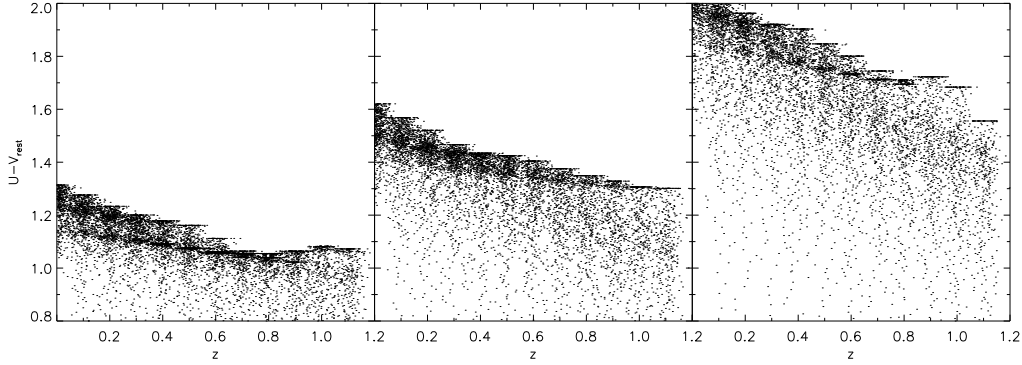


Figure 5.9: Colors of individual galaxies calculated using the truncation history shown in Fig. 5.8 using one fixed metallicity for each plot. The colors were measured for certain redshift values and are shown here spread out in redshift to illustrate the density in color space. The metallicities are from left to right 0.008, 0.02 (solar) and 0.05. There is a bimodality at some redshifts, as a result of kinks in the evolutionary tracks at some values of age/metallicity.

see also Fig. 5.7). In this way, I have a truncation rate history that is consistent with Borch et al. (2006) and can be used to estimate the evolution of the CMR scatter. To describe the truncation rate for epochs not covered by Borch et al. (2006), I choose to model the truncation rate as a constantly increasing function of time from $z_f \sim 5.5$ until $z_{trunc} = 0.9$. The influence of this choice on the results is negligible. The resulting number of truncated (pre-red sequence) galaxies – the integral of the truncation rate – as a function of cosmic epoch is also given in Fig. 5.8.

	Fit		Fixed Slope		Simulation
	measured scatter	intrinsic scatter	measured scatter	intrinsic scatter	
$z = 0.05$	0.124	0.117	0.124	0.117	0.115
$z = 0.55$	0.126	0.124	0.130	0.129	0.126
$z = 0.70$	0.127	0.127	0.126	0.126	0.132
$z = 1.00$	0.210	0.206	0.212	0.208	0.167

Table 5.2: For better comparison the measurement values for the measured and intrinsic red sequence scatter are presented here together with the values for the simulated scatter.

The next step is to build a more realistic truncation model (c.f. Fig. 5.7): instead of choosing one particular truncation time as in §5.2, I instead draw truncation times from the truncation time distribution in Fig. 5.8. I choose 12 ‘observation’ redshifts between $z = 0$ and $z = 1.1$; at each I draw 1000 galaxies from this truncation¹⁴ history shown

¹⁴The results of this chapter do not change significantly if a burst of star formation occurs before truncation, as might be expected in a gas-rich galaxy merger.

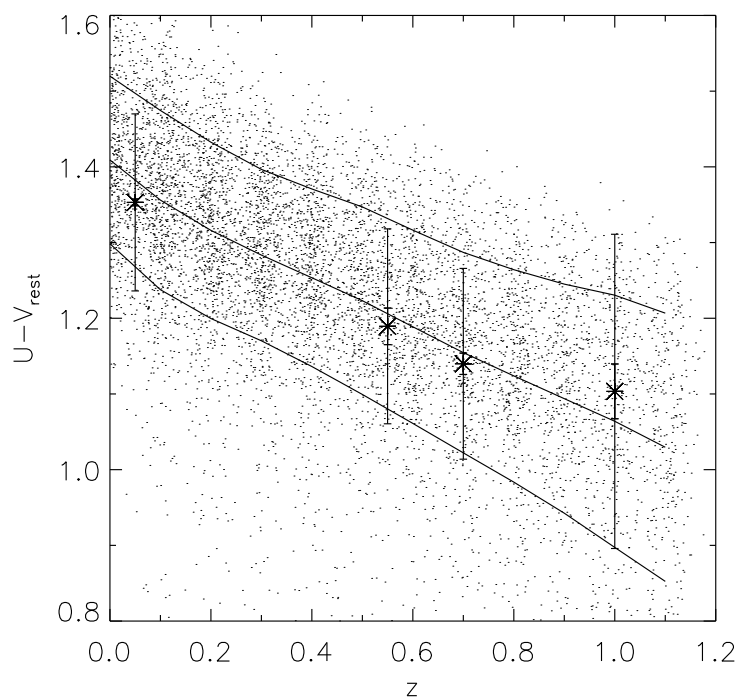


Figure 5.10: Colors of individual galaxies calculated in the same way as for Figure 5.9 but assuming a scatter in metallicity. The lines show the mean value in color and the scatter of the color distribution. Recall that I have used a redshift-dependent luminosity cut as described in Section 5.5.1 to measure the intercepts.

in Fig. 5.8 resulting in samples of galaxies with different truncation redshifts, but the same formation redshift $z_{start} = 3$ for all galaxies¹⁵. Due to this variety of truncation redshifts the galaxies in the samples experienced periods of passive evolution of different length. This then gives a distribution of galaxy colors at each redshift of interest; for display purposes in Figs. 5.9 and 5.10 I have added a small random offset in redshift. I assume no ongoing low-level star formation in red sequence galaxies; while potentially unrealistic, it allows us to estimate the expected scatter from truncation alone¹⁶.

In order to separate between the effects of age and metallicity scatter on the CMR scatter, I first consider the effects of formation history alone in Fig. 5.9. One can see a considerable color scatter from the ongoing accretion of recently-truncated galaxies,

¹⁵Note that this choice of z_{start} differs from z_f in section 5.5.1. In contrast to this former z_f , which was used to simulate the passive evolution after an initial star burst, z_{start} indicates the starting point of a longer period of star formation.

¹⁶One could argue I will estimate lower limits to the scatter of the CMR with this approach. Such an argument has merit, but would neglect (as I also have) the influence of any age/metallicity anti-correlation on the CMR scatter (as observed by e.g. Trager et al., 2000)

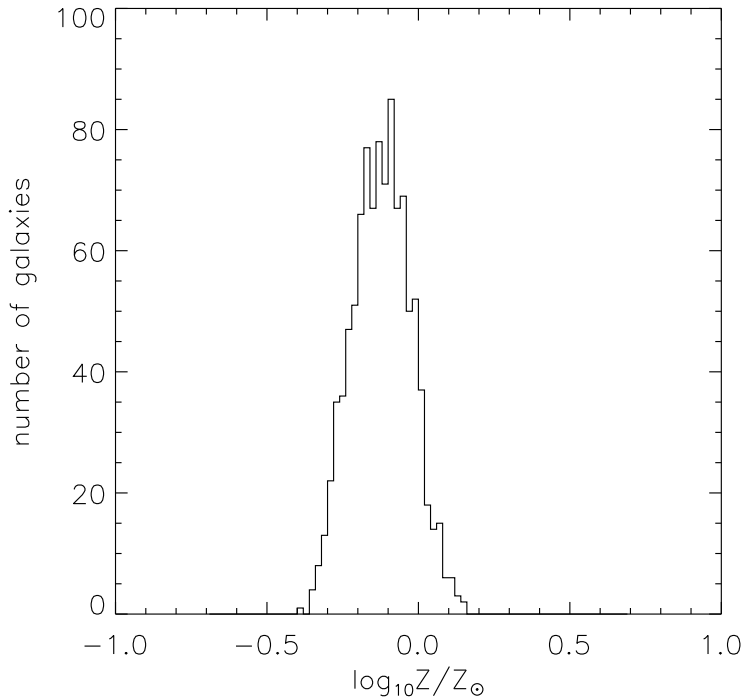


Figure 5.11: Metallicity distribution for the modeled galaxy sample in Figure 5.10. The mean value $\langle \log_{10} Z/Z_{\odot} \rangle$ is -0.12 and standard deviation is 0.1 . Solar metallicity is taken to be 0.02 .

along with some low-level bimodalities caused by kinks in the time evolution of colors for some metallicities (see, e.g., Fig. 5.6). For solar metallicity $Z = 0.02$ the color evolution is smooth, giving no 'pile-ups' in color space. The strong influence of metallicity on the color of the red sequence can also be seen in this plot.

In Fig. 5.10, I show my expectation for the evolution of the CMR intercept and scatter as a function of redshift. I have drawn galaxies from a log-normal distribution in metallicity with mean $[\text{Fe}/\text{H}] = -0.12$ and scatter 0.1 dex which is held constant over redshift (Fig. 5.11)¹⁷. This distribution was chosen to approximately match the observed CMR intercept and scatter, but it is interesting to note that this value of metallicity scatter is consistent with the estimated intrinsic scatter in metallicity of present-day early-type galaxies of ~ 0.1 dex from Gallazzi et al. (2006). I show the mean and scatter (calculated with the same estimation algorithm as the scatter in the observed relations) of the

¹⁷My assumption of a redshift-independent scatter is clearly an over-simplification; yet, in the context of my model in which each galaxy has its own single metallicity it is a defensible one. In reality, the metallicity may evolve if there is any low level residual star formation in early-type galaxies (indeed, if there is an age-metallicity relation in the stars in an individual galaxy, its light-weighted age can evolve as the galaxy ages even in the absence of star formation).

distribution as solid lines. The resulting distribution agrees well with the scatter measurements at the redshifts 0.05, 0.55 and 0.7. At $z = 1.0$, the measured scatter exceeds the model prediction (allowing for more scatter in star formation histories). The results are presented in Table 5.2.

It is interesting to compare my results with a similar analysis of early-type galaxies in clusters carried out by van Dokkum & Franx (2001). They use a similar model of a constantly-growing red sequence to predict both the mass-to-light ratio and color evolution (and scatter) of the early-type galaxy population, finding a relatively slow color evolution and a relatively constant scatter. My results are in qualitative accord with their results for the cluster early-type galaxy population, but are representative of the cosmic-averaged early-type galaxy population and are constrained to reproduce the observed build-up of the early-type galaxy population.

5.5.4 Blue Spheroids

So far, I have made no particular assumption on the mechanism by which galaxies quench their star formation and join the red sequence. In this section, I explore a rather more specific scenario: galaxies structurally transform into an early-type galaxy (e.g., through galaxy merging) *before* reddening on to the red sequence. Such a scenario predicts that there should be a non-negligible population of blue spheroids – i.e., galaxies that are structurally early-type but have blue colors. In this context, I present a range of predictions for their abundance, requiring that blue spheroids i) have colors at least 0.25 mag bluer in $U - V$ than the locus of red sequence galaxies at that redshift, and ii) are at least a given time $t_{recognize}$ from the truncation (or spheroid creation) event. This latter criterion is introduced to allow for a delay $t_{recognize}$ between the event that truncated star formation (e.g. a galaxy merger) and the galaxy becoming recognizably early type; in what follows I explore the range $0 \leq t_{recognize} \leq 0.4$ Gyr, motivated by simulations of galaxy mergers. The ratio of blue spheroids to the total number of spheroidal galaxies (red and blue spheroids) $N_{BS}/(N_{RS} + N_{BS})$ is measured as a function of redshift and is shown in Fig. 5.12 for 3 different values of $t_{recognize}$.

There are two key points to take away from Fig. 5.12. First, the predicted blue spheroid fraction depends sensitively on one's choice of $t_{recognize}$ (and therefore, also, details of the star formation history and dust content of the galaxy)¹⁸. Second, despite

¹⁸In fact, for long $t_{recognize}$, the blue spheroid fraction decreases towards higher redshift because $t_{recognize}$ becomes comparable to the time taken to transition between the blue cloud and red sequence.

this uncertainty, the range in model prediction is in reasonable agreement with observed blue spheroid fractions (e.g. $N_{BS}/(N_{RS} + N_{BS}) \sim 0.06$ at $z \sim 0.6$ from Häußler, 2007¹⁹). The fraction observed by Bamford et al. (2009) for the relevant mass range is slightly higher than in my models, but as they used a different method these values might not be directly comparable. Recall that this toy model was constructed to explore the implications of the growth of the red sequence through the truncation of star formation in blue galaxies. Here I have shown that such a model reproduces *simultaneously* the evolution of the intercept and scatter of the color-magnitude relation since $z = 1$ and the blue spheroid fraction at intermediate redshift. Such an analysis lends considerable weight to the notion that the early-type galaxy population has grown considerably between redshift one and the present day through the truncation of star formation in blue galaxies (through mergers or some other physical process).

5.6 Discussion and Conclusions

The evolution of the scatter of the red sequence is an important source of information about the evolutionary history of the red sequence/early-type galaxy population. In this chapter, I constructed high-accuracy color–magnitude relations at four different redshift ranges using accurate color and spectroscopic redshift information. I used a sample of over 3000 galaxies in the CDFS, in conjunction with a local reference sample of galaxies from the SDSS, to understand the redshift evolution of CMR scatter. I used images from the GEMS survey taken with the ACS onboard HST to provide both high-resolution morphologies (to classify galaxies as early-type) and to measure accurate colors within the half-light radius. In order to calculate accurate k -corrections to rest-frame passbands, I used spectroscopic redshifts compiled from a variety of sources. At all redshifts, I apply a structure and color cut to isolate early-type red-sequence galaxies; at intermediate redshift I were able also to excise star-forming galaxies and AGN from the sample using X-ray and $24\mu\text{m}$ information.

The resulting scatter of the color magnitude relation is ~ 0.1 mag in $U - V$ color at $z = 0.05, 0.55$ and 0.7 , and somewhat higher at $z = 1.0$. This scatter is comparable to those found in some local galaxy clusters (e.g. Abell 85 and 754 of McIntosh et al.,

¹⁹Here I are comparing with the blue spheroid fraction of relatively massive spheroidal galaxies, which have a mass range consistent with my red sequence galaxies (see Häußler, 2007, Fig. 4.13). As Häußler, 2007 (see paragraph 4.5.1) found many of the works quoting a higher blue spheroid fraction are including low-mass / low-density objects that can never turn into a present-day bulge-dominated red sequence galaxy (e.g., Abraham et al., 1999; Schade et al., 1999; Im et al., 2002).

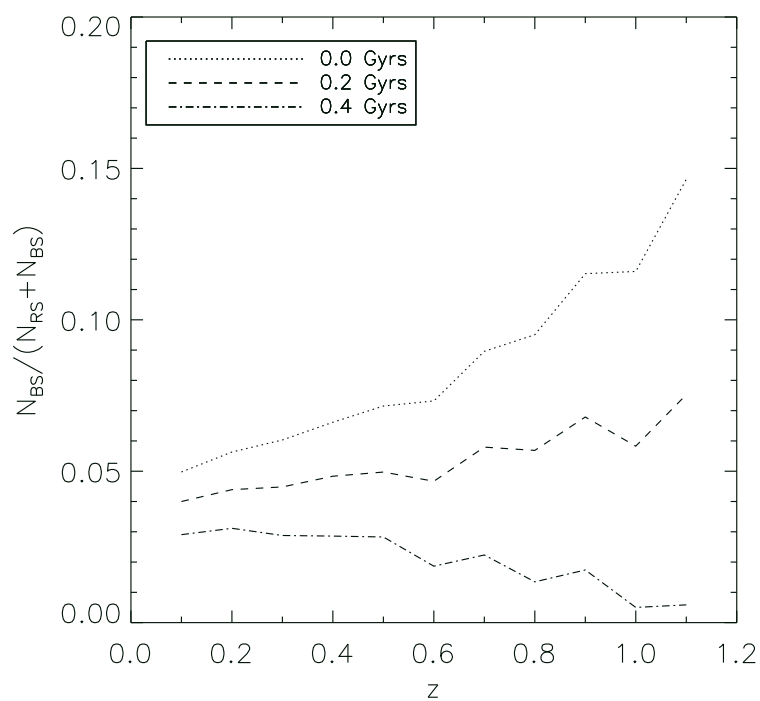


Figure 5.12: The predicted ratio of blue spheroids to the total number of spheroids as a function of redshift for my toy model for the growth of the red sequence. The three curves show the effect of three different choices for $t_{recognize}$, the time taken for a galaxy to become recognizably early type after the event that truncates star formation. Despite the dependence of $N_{BS}/(N_{RS} + N_{BS})$ on $t_{recognize}$, it is remarkable that the predicted blue spheroid fraction is in the range of the observations (e.g. Häußler et al., 2007).

2005b; their Table 8) and larger than that found for the Coma and Abell 496 clusters ($\sigma_{U-V} \sim 0.05$ mag; Bower et al., 1992; Terlevich et al., 2001; McIntosh et al., 2005b). I note in passing that a better observational handle on the environmental dependence of the scatter of the color–magnitude relation, with special attention being paid to possible cluster-to-cluster differences, would be highly desirable (but is clearly beyond the scope of this thesis).

I explored the implications of a measured CMR scatter of $\sigma_{U-V} \sim 0.1$ mag on our understanding of the evolution of early-type galaxies. The CMR scatter can be influenced by when star formation started, when star formation stopped, residual star formation and metallicity. Thus, it is not straightforward to turn the measured CMR scatter into robust constraints in this multi-dimensional space.

I adopted instead a simple approach. The evolving number density of red sequence galaxies has been measured — assuming that this evolution in number density is from the quenching of star formation in galaxies with roughly constant star formation rate before quenching, we have a prediction (motivated by other observations) for the quenching/truncation history of galaxies going on to the red sequence. I have also a measurement of the present-day metallicity scatter of early-type galaxies from Gallazzi et al. (2006). Thus, I have both elements in place where I can *predict* the evolution of the CMR scatter. Importantly, this model — in which new red sequence galaxies are being constantly added at the rate required by observations of red sequence galaxy *number density* — predicts the correct scatter in the *colors* of these red sequence galaxies.

Furthermore, this model predicts approximately the correct number density of blue spheroids - galaxies which are structurally early-type but have blue colors - although admittedly with considerable model dependence. Thus, I conclude that these different observations - the evolution of the number density of red sequence galaxies, the evolution of the intercept and scatter of the color-magnitude relation, and the blue spheroid fraction - paint a consistent picture in which the early-type galaxy population grows significantly between $z = 1$ and the present day through the quenching of star formation in blue cloud galaxies.

Table 5.3: Spectroscopic redshifts from different catalogs

redshift catalog	number of objects used
VVDS (Le Fèvre et al., 2004)	629
Szokoly et al. (2004)	38
GOODS/FORS2 DR 3.0 (Vanzella et al., 2008)	464
Ravikumar et al. (2007)	303
S. Kopolov et al., in prep.	510
VIMOS DR 1.0 (Popesso et al., 2009)	1086

Appendix: Spectroscopic Redshift Sample

In order to study the evolution of the scatter of the red sequence, one must use a sample of galaxies with spectroscopic redshifts. Toward this end, I compiled a catalog of spectroscopic redshifts from a variety of sources, listed below.

I used the data of some projects which surveyed the entire CDFS but a better coverage is reached for the GOODS field (see also Fig. 5.13). A collection of spectroscopic redshifts for the CDFS can be found in the ‘Master Catalog of CDFS spectroscopy’ (http://www.eso.org/science/goods/spectroscopy/CDFS_Mastercat/). I used data from one paper included in this catalog (Szokoly et al., 2004). Also the VVDS (VIMOS-VLT Deep Survey; Le Fèvre et al., 2004), Ravikumar et al. (2007) and S. Kopolov et al. (in preparation; VVDS high resolution spectroscopy) surveyed the CDFS. With data limited to the GOODS field I used the VLT/FORS2 Spectroscopy Data Release 3.0 (Vanzella et al., 2005, 2006, 2008) and the GOODS VLT/VIMOS Spectroscopy Data Release 1.0 (Popesso et al., 2009). For sources with good quality flags the spectroscopic redshifts were taken without further testing. These are:

- VVDS - 4 (confidence level 100 per cent) and 3 (95 per cent)
- FORS2 - A (solid redshift determination) and B (likely redshift determination)
- Szokoly et al. (2004) - 3.0 (reliable redshift determination with unambiguous X-ray counterpart) and 2.0 (reliable redshift determination)
- Ravikumar et al. (2007) - secure observations

In the case of insecure or unknown data quality, the spectroscopic redshifts were tested against photometric redshifts from the COMBO-17 survey. In such cases I used only

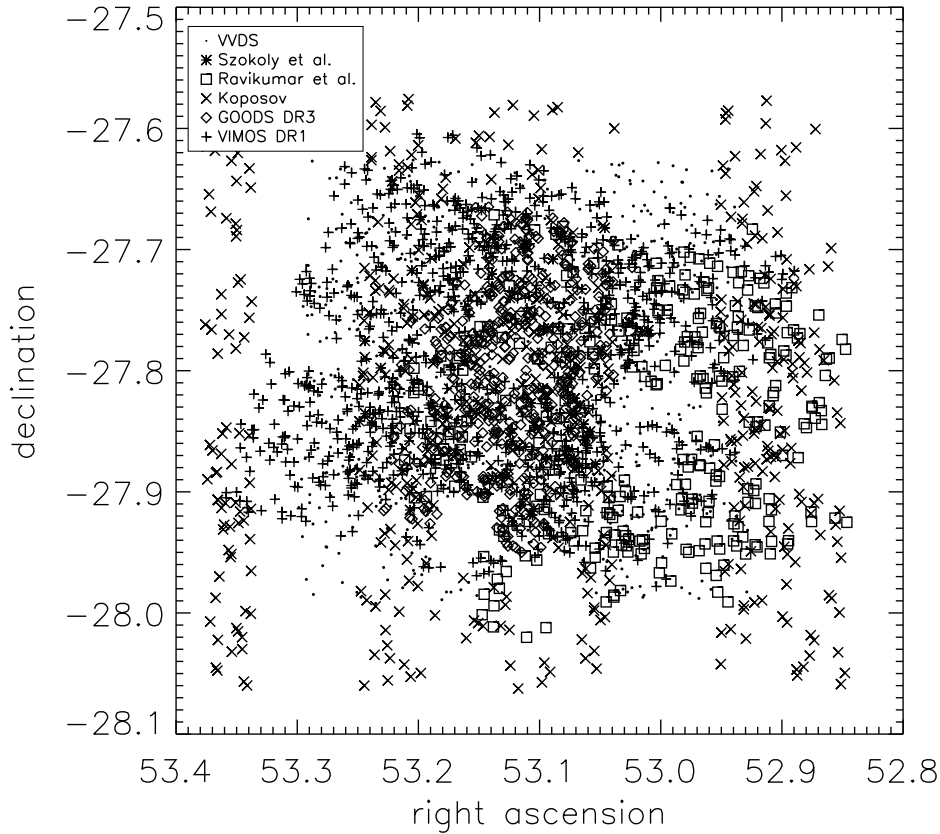


Figure 5.13: All objects with spectroscopic redshifts adopted in this chapter are shown here at their positions on the sky. The different symbols showing the origin of the spectroscopic redshift value for each object.

those spectroscopic redshifts which differ by less than 0.1 from the photometric ones. In total this leads to a sample of 3440 objects (3030 useable for this project). See Figure 5.13 for the positions on the sky of the objects used for flux measurements. The total numbers of objects of each catalog is listed in Table 5.3. The combined sample covers a roughly constant fraction of about 20% of the galaxies in the relevant magnitude range ($20\text{ mag} < M_I < 22\text{ mag}$) and then drops off towards fainter magnitudes with a fraction of about 10% for $M_I < 24\text{ mag}$. Red and blue galaxies show a similar behavior.

Part III

Conclusions and Outlook

6

SUMMARY & CONCLUSIONS

IN THIS THESIS I investigated two aspects in the framework of galaxy formation and evolution. The common aspect of these two projects is the question how galaxies, individually and as a whole population, are influenced and shaped by on-going merging in the universe. In the project presented in the first part of this thesis these merging events are directly observable, whereas in the second project the transformation of galaxies, with merging being the favored explanation for this transition, is merely used as a hypothesis in a modelling attempt to explain the evolution of a group of galaxies.

In the halos of disk galaxies traces of the accretion of satellites are conserved over a long time, in principle allowing reconstruction of some fraction of the formation history of the host galaxy. In this thesis I explored ways to discover and study stellar streams as the remnants of these merging events in the halo. In Chapter 3 I present and apply a selection method for blue horizontal branch (BHB) stars which are used as precise standard candles to probe the three-dimensional structure of the halo. I present different projection and visualization techniques used in this thesis to find and analyze stellar streams, discuss their advantages and disadvantages, and give an example of a candidate for a new stellar stream detection.

In Chapter 4 I looked in more detail into the properties of the largest formation of this kind in the Milky Way halo, the Sagittarius stellar stream. Besides tracing the formation history of the halo of the host galaxy, stellar streams are of interest also as probes of the gravitational potential. The detailed investigation of the properties of these objects is an important step for a precise modelling input. The Sagittarius stellar stream is of special value in this respect since it has been observed over a full circle on the sky providing a wealth of data. This suggests that it should also provide a good basis for models of its disruption and therefore also for the underlying gravitational potential in which the disruption process took place. However, the many controversial modeling attempts to date show that the available data still allows for a good deal of uncertainty. Stronger

constraints on the models through more precise measurements on the data are key ingredients to achieve this.

I performed a set of measurements on the stream using BHB stars as precise standard candles for which I applied a selection method which reduces the amount of contamination from other stellar populations. The severe contamination which is seen in the selection applied in previous studies of the stream with BHB stars has caused doubt in their reliability. For that reason other standard candles like M giants were widely used also as a basis for models of the stream. Although there is the clear advantage of having the full orbit probed in M giants, they are much worse standard candles. In this work I study the properties of the Sagittarius stellar stream based on its appearance in BHB stars, performing an analysis which is independent of other stellar populations or models, but showing comparisons with both. I present a set of measurements on the leading arm of the stream including the line-of-sight thickness of the stream, the distances of the two branches of the on-sky bifurcation (finding only a small offset) and the selection of a high probability sample of leading arm stars taking into account also their radial velocities. Furthermore I present an overdensity which could be associated with the stream and possibly represent part of its trailing arm. Furthermore, comparison of the observations with a number of attempts to quantitatively model the disruption of the Sagittarius dwarf spheroidal in the potential of the Milky Way showed that a predicted overdensity at ~ 20 kpc distance at this closest point, corresponding to part of the Sgr trailing arm, is not observed. Instead, a much more distant overdensity is observed. New models of the Sgr disruption process need to take account of these new observational constraints.

In the second part of this thesis I studied the evolution of the color magnitude relation of early-type galaxies. In the evolution of its properties, the mean and the scatter of the color, this relation reflects the composition of galaxies on the relation at a given cosmic time. Using HST imaging and spectroscopic redshifts for an intermediate redshift sample of about 1200 galaxies (173 of which are early-type galaxies), supplemented with a low redshift sample of 2053 galaxies drawn from SDSS data, this study provided the best measurements to date of the scatter of the color magnitude relation of early-type galaxies in four redshift intervals up to $z = 1$. To explore the implications of these measurements I use a simple model in which new galaxies are being constantly added to the red sequence through the truncation of star formation in blue cloud galaxies at the rate found by observation of the growth rate of the early type galaxy population. Furthermore the measured metallicity scatter in these galaxies was applied to the model galaxies, yielding a more realistic estimate of the color scatter of this population. The

models show a good agreement with the measurements and also make a prediction for the blue spheroid fraction which is consistent with observations.

OUTLOOK

FOR THIS THESIS I looked into the level of (sub-)structure of the stellar halo of the Milky Way using BHB stars as a tracer population. I worked on the development of techniques to find and characterize stellar streams. Here, I want to give an overview over some possible directions to follow up on this project.

Automatic Structure Search: A natural follow-up to this project would be to combine the different projection and visualization techniques developed for the PhD to develop a systematic search for streams in the halo. I started on different attempts in this direction (including looking at great circles on a galactocentric sphere, planes through the GC, nearest neighbor alignment visualizations and so on) which need to be improved/combined. The benefits of implementing an automatic search algorithm are two-fold. Besides the obvious potential and goal to discover new structures, this would add to our understanding of the global picture of the whole system and the composition of the stellar halo.

A major advantage of an automated search algorithm is that simulations can be searched in the same way as the observed data set. It has been already shown that stellar halos similar to what we see in the Milky Way can be built up to a large fraction, or even entirely, through the disruption of satellite galaxies. Through a comparison with a large set of these models, the observed degree of substructure can be related to the simulated formation histories, potentially helping us to gain a more precise picture of the formation (Bell et al., 2008; Xue et al., 2010). Secondly, models can help in testing, and improving, the search algorithm itself. As an example, using distance shells and looking for orbits on great circles introduce a bias towards streams which have an equidistant portion in their orbits. Significance tests would need to be implemented especially for the automatic identification of streams.

In recent years our picture of the Milky Way halo has developed largely with the availability of data and will continue to do so, as new and on-going surveys are building up a wider and deeper view of the stellar halo. Today the borders of survey fields are limiting our view on the halo and its many different features. As an example in the context of this thesis, the Sagittarius stellar stream was probed over the whole sky with 2MASS, but a coverage of the full orbital plane with a survey allowing more precise distance determination, such as I presented here with BHB stars selected from SDSS data, and also a wider coverage with spectroscopic surveys, would clearly provide a great dataset for modelling the orbit of the satellite and with that the gravitational potential of the Milky Way.

Search algorithms may also be applied for other nearby galaxies like Andromeda. Also for our large neighboring galaxy new insides were gained out of new data like the recently completed PAndAS survey (McConnachie et al., 2009). The panoramic view we have of Andromeda and other galaxies offers different opportunities, but also new challenges are associated with this viewpoint compared to studies of the Milky Way. The comparison of the accretion histories of the two large disk galaxies in the local group will reveal insides in the similarities and differences and thus help in understanding the global picture of galaxy formation. A less detailed view can be achieved on a growing set of external disk galaxies with prominent traces of accretion events (e.g., Martínez-Delgado et al., 2010) adding to the picture of the variety of formation histories and helping to get a sense of the 'typical' disk galaxy.

Spectroscopic Follow-up: For promising candidates spectroscopic follow-up enables studies of the kinematic properties of the stream and can confirm or rule out the nature of the overdensity as being tidally disrupted in the potential of the Milky Way. Having information about orbit positions and velocities are necessary inputs for orbit modelling. The identification and characterization of individual streams has the benefit of increasing our understanding of disruption processes in detail and helps us to determine the gravitational potential of the Milky Way. Although large structures like the Sagittarius stellar stream are known for some time and has been used to constrain the properties of the potential the outcome of these studies are, to date, quite controversial (Helmi, 2004b; Fellhauer et al., 2006; Johnston et al., 2005; Law & Majewski, 2010b). More data on stellar stream orbits could help in this respect.

Chemical Compositions: To gain more insight into the origin of the known streams around the Milky Way the chemical compositions of the stellar populations is another

constraint. While globular clusters show a homogeneous abundance of elements the stars in dwarf galaxies often show abundance spreads. This would be also reflected in the stars expelled from the progenitors along their orbits and could tell us about the nature of these progenitors. This is again important for the reconstruction of the formation history of the Milky Way.

BIBLIOGRAPHY

- Abadi, M. G., Navarro, J. F., Steinmetz, M., & Eke, V. R. 2003, *ApJ*, **591**, 499
- Abazajian, K. N., Adelman-McCarthy, J. K., Agüeros, M. A., et al. 2009, *ApJS*, **182**, 543
- Abraham, R. G., Ellis, R. S., Fabian, A. C., Tanvir, N. R., & Glazebrook, K. 1999, *MNRAS*, **303**, 641
- Adelman-McCarthy, J. K. e. 2006, *ApJS*, **162**, 38
- Arnold, R. & Gilmore, G. 1992, *MNRAS*, **257**, 225
- Bamford, S. P., Nichol, R. C., Baldry, I. K., et al. 2009, *MNRAS*, **393**, 1324
- Barnes, J. E. & Hernquist, L. 1996, *ApJ*, **471**, 115
- Baum, W. A. 1962, in IAU Symposium, Vol. 15, Problems of Extra-Galactic Research, ed. G. C. McVittie, 390–+
- Beers, T. C., Doinidis, S. P., Griffin, K. E., Preston, G. W., & Shectman, S. A. 1992, *AJ*, **103**, 267
- Bell, E. F., McIntosh, D. H., Barden, M., et al. 2004a, *ApJ*, **600**, L11
- Bell, E. F., Wolf, C., Meisenheimer, K., et al. 2004b, *ApJ*, **608**, 752
- Bell, E. F., Xue, X. X., Rix, H., Ruhland, C., & Hogg, D. W. 2010, *AJ*, **140**, 1850
- Bell, E. F., Zheng, X. Z., Papovich, C., et al. 2007, *ApJ*, **663**, 834
- Bell, E. F., Zucker, D. B., Belokurov, V., et al. 2008, *ApJ*, **680**, 295
- Bellazzini, M. 2007, *A&A*, **473**, 171
- Bellazzini, M., Correnti, M., Ferraro, F. R., Monaco, L., & Montegriffo, P. 2006, *A&A*, **446**, L1
- Bellazzini, M., Ferraro, F. R., & Ibata, R. 2003, *AJ*, **125**, 188
- Bellazzini, M., Ferraro, F. R., Origlia, L., et al. 2002, *AJ*, **124**, 3222
- Bellazzini, M., Ibata, R. A., Chapman, S. C., et al. 2008, *AJ*, **136**, 1147
- Belokurov, V., Evans, N. W., Bell, E. F., et al. 2007a, *ApJ*, **657**, L89

BIBLIOGRAPHY

- Belokurov, V., Evans, N. W., Irwin, M. J., et al. 2007b, *ApJ*, **658**, 337
- Belokurov, V., Walker, M. G., Evans, N. W., et al. 2009, *MNRAS*, **397**, 1748
- Belokurov, V., Zucker, D. B., Evans, N. W., et al. 2006a, *ApJ*, **642**, L137
- Belokurov, V., Zucker, D. B., Evans, N. W., et al. 2007c, *ApJ*, **654**, 897
- Belokurov, V., Zucker, D. B., Evans, N. W., et al. 2006b, *ApJ*, **647**, L111
- Bender, R. & Nieto, J. 1990, *A&A*, **239**, 97
- Binney, J. 2008, *MNRAS*, **386**, L47
- Blanton, M. R. 2006, *ApJ*, **648**, 268
- Blanton, M. R., Hogg, D. W., Bahcall, N. A., et al. 2003a, *ApJ*, **592**, 819
- Blanton, M. R., Lin, H., Lupton, R. H., et al. 2003b, *AJ*, **125**, 2276
- Blanton, M. R., Schlegel, D. J., Strauss, M. A., et al. 2005, *AJ*, **129**, 2562
- Böhm-Vitense, E. 1989, *Cambridge University Press*
- Borch, A., Meisenheimer, K., Bell, E. F., et al. 2006, *A&A*, **453**, 869
- Bower, R. G., Lucey, J. R., & Ellis, R. S. 1992, *MNRAS*, **254**, 601
- Brasseur, C. M., Martin, N. F., Rix, H., et al. 2011, *ApJ*, **729**, 23
- Brown, M. J. I., Brand, K., Dey, A., et al. 2006, *ApJ*, **638**, 88
- Brown, M. J. I., Dey, A., Jannuzi, B. T., et al. 2007, *ApJ*, **654**, 858
- Bullock, J. S. & Johnston, K. V. 2005, *ApJ*, **635**, 931
- Bullock, J. S., Kravtsov, A. V., & Weinberg, D. H. 2001, *ApJ*, **548**, 33
- Bundy, K., Ellis, R. S., Conselice, C. J., et al. 2005, in Bulletin of the American Astronomical Society, Vol. 37, Bulletin of the American Astronomical Society, 1235–+
- Carney, B. W., Latham, D. W., Laird, J. B., Grant, C. E., & Morse, J. A. 2001, *AJ*, **122**, 3419
- Carollo, D., Beers, T. C., Lee, Y. S., et al. 2007, *Nature*, **450**, 1020
- Carrera, R., Aparicio, A., Martínez-Delgado, D., & Alonso-García, J. 2002, *AJ*, **123**, 3199
- Casetti-Dinescu, D. I., Girard, T. M., Majewski, S. R., et al. 2009, *ApJ*, **701**, L29
- Catelan, M. 2009, *Ap&SS*, **320**, 261

- Chandrasekhar, S. 1943a, *ApJ*, **97**, 255
- Chandrasekhar, S. 1943b, *ApJ*, **97**, 263
- Chandrasekhar, S. 1943c, *ApJ*, **98**, 54
- Chen, H.-W., Marzke, R. O., McCarthy, P. J., et al. 2003, *ApJ*, **586**, 745
- Chiba, M. & Beers, T. C. 2000, *AJ*, **119**, 2843
- Choi, J., Weinberg, M. D., & Katz, N. 2007, *MNRAS*, **381**, 987
- Cimatti, A. 2006, *Memorie della Societa Astronomica Italiana*, **77**, 703
- Clewley, L. & Jarvis, M. J. 2006, *MNRAS*, **368**, 310
- Clewley, L., Warren, S. J., Hewett, P. C., et al. 2002, *MNRAS*, **337**, 87
- Cohen, J. G., Kirby, E. N., Simon, J. D., & Geha, M. 2010, *ApJ*, **725**, 288
- Coleman, G. D., Wu, C.-C., & Weedman, D. W. 1980, *ApJS*, **43**, 393
- Cool, R. J., Eisenstein, D. J., Johnston, D., et al. 2006, *AJ*, **131**, 736
- Correnti, M., Bellazzini, M., Ibata, R. A., Ferraro, F. R., & Varghese, A. 2010, *ApJ*, **721**, 329
- Cox, T. J., Dutta, S. N., Di Matteo, T., et al. 2006, *ApJ*, **650**, 791
- Da Costa, G. S. & Armandroff, T. E. 1995, *AJ*, **109**, 2533
- Dalessandro, E., Lanzoni, B., Ferraro, F. R., et al. 2008, *ApJ*, **681**, 311
- Dall'Ora, M., Clementini, G., Kinemuchi, K., et al. 2006, *ApJ*, **653**, L109
- Davies, R. L., Efstathiou, G., Fall, S. M., Illingworth, G., & Schechter, P. L. 1983, *ApJ*, **266**, 41
- de Jong, J. T. A., Rix, H., Martin, N. F., et al. 2008, *AJ*, **135**, 1361
- de Jong, R. S. 1996, *A&AS*, **118**, 557
- Dotter, A., Chaboyer, B., Jevremović, D., et al. 2007, *AJ*, **134**, 376
- Dotter, A., Chaboyer, B., Jevremović, D., et al. 2008, *ApJS*, **178**, 89
- Duffau, S., Zinn, R., Vivas, A. K., et al. 2006, *ApJ*, **636**, L97
- Eggen, O. J., Lynden-Bell, D., & Sandage, A. R. 1962, *ApJ*, **136**, 748
- Faber, S. M. & Jackson, R. E. 1976, *ApJ*, **204**, 668
- Faber, S. M., Willmer, C. N. A., Wolf, C., et al. 2007, *ApJ*, **665**, 265

BIBLIOGRAPHY

- Fellhauer, M., Belokurov, V., Evans, N. W., et al. 2006, *ApJ*, **651**, 167
- Ferguson, A. M. N., Irwin, M. J., Ibata, R. A., Lewis, G. F., & Tanvir, N. R. 2002, *AJ*, **124**, 1452
- Fioc, M. & Rocca-Volmerange, B. 1997, *A&A*, **326**, 950
- Flynn, C., Sommer-Larsen, J., & Christensen, P. R. 1994, *MNRAS*, **267**, 77
- Franzetti, P., Scodreggio, M., Garilli, B., et al. 2007, *A&A*, **465**, 711
- Freeman, K. C. 1970, *ApJ*, **160**, 811
- Fukugita, M., Ichikawa, T., Gunn, J. E., et al. 1996, *AJ*, **111**, 1748
- Gallazzi, A., Charlot, S., Brinchmann, J., & White, S. D. M. 2006, *MNRAS*, **370**, 1106
- Geha, M., Willman, B., Simon, J. D., et al. 2009, *ApJ*, **692**, 1464
- Georgiev, I. Y., Hilker, M., Puzia, T. H., Goudfrooij, P., & Baumgardt, H. 2009, *MNRAS*, **396**, 1075
- Giavalisco, M., Ferguson, H. C., Koekemoer, A. M., et al. 2004, *ApJ*, **600**, L93
- Gómez-Flechoso, M. A., Fux, R., & Martinet, L. 1999, *A&A*, **347**, 77
- Governato, F., Willman, B., Mayer, L., et al. 2007, *MNRAS*, **374**, 1479
- Grillmair, C. J. 2006, *ApJ*, **645**, L37
- Grillmair, C. J. 2009, *ApJ*, **693**, 1118
- Grillmair, C. J. & Dionatos, O. 2006, *ApJ*, **643**, L17
- Grillmair, C. J. & Johnson, R. 2006, *ApJ*, **639**, L17
- Gunn, J. E., Carr, M., Rockosi, C., et al. 1998, *AJ*, **116**, 3040
- Gunn, J. E., Siegmund, W. A., Mannery, E. J., et al. 2006, *AJ*, **131**, 2332
- Harris, W. E. 1996, *AJ*, **112**, 1487
- Häußler, B. 2007, PhD thesis, Ruprecht-Karls-Universität Heidelberg, Germany, <http://www.ub.uni-heidelberg.de/archiv/7190>, 2007PhDT.....1H
- Häußler, B., McIntosh, D. H., Barden, M., et al. 2007, *ApJS*, **172**, 615
- Helmi, A. 2004a, *MNRAS*, **351**, 643
- Helmi, A. 2004b, *ApJ*, **610**, L97
- Helmi, A. & White, S. D. M. 1999, *MNRAS*, **307**, 495

- Helmi, A. & White, S. D. M. 2001, *MNRAS*, **323**, 529
- Hilker, M. & Richtler, T. 2000, *A&A*, **362**, 895
- Hills, J. G. & Day, C. A. 1976, *Astrophys. Lett.*, **17**, 87
- Hogg, D. W., Finkbeiner, D. P., Schlegel, D. J., & Gunn, J. E. 2001, *AJ*, **122**, 2129
- Hopkins, P. F., Bundy, K., Hernquist, L., & Ellis, R. S. 2007, *ApJ*, **659**, 976
- Hopkins, P. F., Hernquist, L., Cox, T. J., et al. 2006, *ApJS*, **163**, 1
- Hubble, E. P. 1936, *Yale University Press*
- Ibata, R., Irwin, M., Lewis, G., Ferguson, A. M. N., & Tanvir, N. 2001a, *Nature*, **412**, 49
- Ibata, R., Irwin, M., Lewis, G. F., & Stolte, A. 2001b, *ApJ*, **547**, L133
- Ibata, R., Lewis, G. F., Irwin, M., Totten, E., & Quinn, T. 2001c, *ApJ*, **551**, 294
- Ibata, R., Martin, N. F., Irwin, M., et al. 2007, *ApJ*, **671**, 1591
- Ibata, R. A., Gilmore, G., & Irwin, M. J. 1994, *Nature*, **370**, 194
- Ibata, R. A., Gilmore, G., & Irwin, M. J. 1995, *MNRAS*, **277**, 781
- Ibata, R. A., Irwin, M. J., Lewis, G. F., Ferguson, A. M. N., & Tanvir, N. 2003, *MNRAS*, **340**, L21
- Ibata, R. A., Lewis, G. F., Irwin, M. J., & Quinn, T. 2002, *MNRAS*, **332**, 915
- Im, M., Simard, L., Faber, S. M., et al. 2002, *ApJ*, **571**, 136
- Ivezić, Ž., Goldston, J., Finlator, K., et al. 2000, *AJ*, **120**, 963
- Ivezić, Ž., Lupton, R. H., Schlegel, D., et al. 2004, *Astronomische Nachrichten*, **325**, 583
- Jahnke, K., Sánchez, S. F., Wisotzki, L., et al. 2004, *ApJ*, **614**, 568
- Jin, S. & Lynden-Bell, D. 2007, *MNRAS*, **378**, L64
- Johnston, K. V., Law, D. R., & Majewski, S. R. 2005, *ApJ*, **619**, 800
- Johnston, K. V., Spergel, D. N., & Haydn, C. 2002, *ApJ*, **570**, 656
- Johnston, K. V., Zhao, H., Spergel, D. N., & Hernquist, L. 1999, *ApJ*, **512**, L109
- Jurić, M., Ivezić, Ž., Brooks, A., et al. 2008, *ApJ*, **673**, 864
- Kinman, T. D., Salim, S., & Clewley, L. 2007, *ApJ*, **662**, L111

BIBLIOGRAPHY

- Kinman, T. D., Suntzeff, N. B., & Kraft, R. P. 1994, *AJ*, **108**, 1722
- Kinney, A. L., Calzetti, D., Bohlin, R. C., et al. 1996, *ApJ*, **467**, 38
- Kirby, E. N., Simon, J. D., Geha, M., Guhathakurta, P., & Frebel, A. 2008, *ApJ*, **685**, L43
- Kodama, T. & Arimoto, N. 1997, *A&A*, **320**, 41
- Kodama, T. & Smail, I. 2001, *MNRAS*, **326**, 637
- Koposov, S., Belokurov, V., Evans, N. W., et al. 2008, *ApJ*, **686**, 279
- Koposov, S. E., Yoo, J., Rix, H., et al. 2009, *ApJ*, **696**, 2179
- Kroupa, P. 2001, *MNRAS*, **322**, 231
- Law, D. R., Johnston, K. V., & Majewski, S. R. 2005, *ApJ*, **619**, 807
- Law, D. R. & Majewski, S. R. 2010a, *ApJ*, **718**, 1128
- Law, D. R. & Majewski, S. R. 2010b, *ApJ*, **714**, 229
- Le Fèvre, O., Vettolani, G., Paltani, S., et al. 2004, *A&A*, **428**, 1043
- Lee, M. G., Park, H. S., Park, J., et al. 2003, *AJ*, **126**, 2840
- Lehmer, B. D., Brandt, W. N., Alexander, D. M., et al. 2005, *ApJS*, **161**, 21
- Lewis, G. F. & Ibata, R. A. 2005, *Publications of the Astronomical Society of Australia*, **22**, 190
- Lupton, R. H., Gunn, J. E., & Szalay, A. S. 1999, *AJ*, **118**, 1406
- Majewski, S. R., Beaton, R. L., Patterson, R. J., et al. 2007, *ApJ*, **670**, L9
- Majewski, S. R., Kunkel, W. E., Law, D. R., et al. 2004, *AJ*, **128**, 245
- Majewski, S. R., Siegel, M. H., Kunkel, W. E., et al. 1999, *AJ*, **118**, 1709
- Majewski, S. R., Skrutskie, M. F., Weinberg, M. D., & Ostheimer, J. C. 2003, *ApJ*, **599**, 1082
- Markevitch, M., Gonzalez, A. H., Clowe, D., et al. 2004, *ApJ*, **606**, 819
- Martin, N. F., Ibata, R. A., Chapman, S. C., Irwin, M., & Lewis, G. F. 2007, *MNRAS*, **380**, 281
- Martin, N. F., McConnachie, A. W., Irwin, M., et al. 2009, *ApJ*, **705**, 758
- Martínez-Delgado, D., Gabany, R. J., Crawford, K., et al. 2010, *AJ*, **140**, 962

- Martínez-Delgado, D., Gómez-Flechoso, M. Á., Aparicio, A., & Carrera, R. 2004, *ApJ*, **601**, 242
- Martínez-Delgado, D., Peñarrubia, J., Gabany, R. J., et al. 2008, *ApJ*, **689**, 184
- Mateo, M., Fischer, P., & Krzemiński, W. 1995, *AJ*, **110**, 2166
- Mateo, M. L. 1998, *ARA&A*, **36**, 435
- McConnachie, A. W., Irwin, M. J., Ibata, R. A., et al. 2009, *Nature*, **461**, 66
- McCrea, W. H. 1964, *MNRAS*, **128**, 147
- McIntosh, D. H., Bell, E. F., Rix, H.-W., et al. 2005a, *ApJ*, **632**, 191
- McIntosh, D. H., Zabludoff, A. I., Rix, H.-W., & Caldwell, N. 2005b, *ApJ*, **619**, 193
- Mighell, K. J. & Burke, C. J. 1999, *AJ*, **118**, 366
- Monaco, L., Bellazzini, M., Ferraro, F. R., & Pancino, E. 2003, *ApJ*, **597**, L25
- Moore, B., Ghigna, S., Governato, F., et al. 1999, *ApJ*, **524**, L19
- Moster, B. P., Macciò, A. V., Somerville, R. S., Johansson, P. H., & Naab, T. 2010, *MNRAS*, **403**, 1009
- Mouhcine, M., Ibata, R., & Rejkuba, M. 2010, *ApJ*, **714**, L12
- Navarro, J. F. & Steinmetz, M. 1997, *ApJ*, **478**, 13
- Newberg, H. J., Yanny, B., Cole, N., et al. 2007, *ApJ*, **668**, 221
- Newberg, H. J., Yanny, B., Grebel, E. K., et al. 2003, *ApJ*, **596**, L191
- Newberg, H. J., Yanny, B., Rockosi, C., et al. 2002, *ApJ*, **569**, 245
- Niederste-Ostholt, M., Belokurov, V., Evans, N. W., & Peñarrubia, J. 2010, *ApJ*, **712**, 516
- Odenkirchen, M., Grebel, E. K., Rockosi, C. M., et al. 2001, *ApJ*, **548**, L165
- Papovich, C., Dole, H., Egami, E., et al. 2004, *ApJS*, **154**, 70
- Peñarrubia, J., Belokurov, V., Evans, N. W., et al. 2010a, *MNRAS*, **408**, L26
- Peñarrubia, J., Benson, A. J., Walker, M. G., et al. 2010b, *MNRAS*, **406**, 1290
- Peng, C. Y., Ho, L. C., Impey, C. D., & Rix, H. 2002, *Astronomical J.*, **124**, 266
- Perets, H. B. & Fabrycky, D. C. 2009, *ApJ*, **697**, 1048
- Perlmutter, S., Aldering, G., Goldhaber, G., et al. 1999, *ApJ*, **517**, 565

BIBLIOGRAPHY

- Peterson, R. C., Olszewski, E. W., & Aaronson, M. 1986, *ApJ*, **307**, 139
- Pier, J. R. 1983, *ApJS*, **53**, 791
- Pier, J. R., Munn, J. A., Hindsley, R. B., et al. 2003, *AJ*, **125**, 1559
- Pimblet, K. A., Smail, I., Kodama, T., et al. 2002, *MNRAS*, **331**, 333
- Popesso, P., Dickinson, M., Nonino, M., et al. 2009, *A&A*, **494**, 443
- Preston, G. W. & Sneden, C. 2000, *AJ*, **120**, 1014
- Ravikumar, C. D., Puech, M., Flores, H., et al. 2007, *A&A*, **465**, 1099
- Richardson, J. C., Irwin, M. J., McConnachie, A. W., et al. 2011, *ApJ*, **732**, 76
- Riess, A. G., Filippenko, A. V., Challis, P., et al. 1998, *AJ*, **116**, 1009
- Ripepi, V., Clementini, G., Di Criscienzo, M., et al. 2007, *ApJ*, **667**, L61
- Rix, H.-W., Barden, M., Beckwith, S. V. W., et al. 2004, *ApJS*, **152**, 163
- Robaina, A. R., Bell, E. F., Skelton, R. E., et al. 2009, *ApJ*, **704**, 324
- Romano, D., Matteucci, F., Tosi, M., et al. 2007, *MNRAS*, **376**, 405
- Rubin, V. C. & Ford, Jr., W. K. 1970, *ApJ*, **159**, 379
- Rubin, V. C., Ford, W. K. J., & Thonnard, N. 1980, *ApJ*, **238**, 471
- Rudnick, G., Rix, H.-W., Franx, M., et al. 2003, *ApJ*, **599**, 847
- Sandage, A. R. 1953, *AJ*, **58**, 61
- Sanders, D. B. & Mirabel, I. F. 1996, *ARA&A*, **34**, 749
- Sandquist, E. L. & Hess, J. M. 2008, *AJ*, **136**, 2259
- Sarajedini, A. & Layden, A. C. 1995, *AJ*, **109**, 1086
- Scarlata, C., Carollo, C. M., Lilly, S. J., et al. 2007, *ApJS*, **172**, 494
- Schade, D., Lilly, S. J., Crampton, D., et al. 1999, *ApJ*, **525**, 31
- Schweizer, F. & Seitzer, P. 1992, *AJ*, **104**, 1039
- Searle, L. & Zinn, R. 1978, *ApJ*, **225**, 357
- Sérsic, J. L. 1968, Atlas de galaxias australes (Cordoba, Argentina: Observatorio Astronómico, 1968)
- Sharma, S., Johnston, K. V., Majewski, S. R., et al. 2010, *ApJ*, **722**, 750

- Siegel, M. H. 2006, *ApJ*, **649**, L83
- Simon, J. D. & Geha, M. 2007, *ApJ*, **670**, 313
- Sirko, E., Goodman, J., Knapp, G. R., et al. 2004, *AJ*, **127**, 899
- Skrutskie, M. F., Cutri, R. M., Stiening, R., et al. 2006, *AJ*, **131**, 1163
- Smith, J. A., Tucker, D. L., Kent, S., et al. 2002, *AJ*, **123**, 2121
- Smith, K. W., Bailer-Jones, C. A. L., Klement, R. J., & Xue, X. X. 2010, *A&A*, **522**, A88+
- Sommer-Larsen, J. & Christensen, P. R. 1986, *MNRAS*, **219**, 537
- Sommer-Larsen, J., Götz, M., & Portinari, L. 2003, *ApJ*, **596**, 47
- Spergel, D. N., Verde, L., Peiris, H. V., et al. 2003, *ApJS*, **148**, 175
- Springel, V., White, S. D. M., Jenkins, A., et al. 2005, *Nature*, **435**, 629
- Stoughton, C., Lupton, R. H., Bernardi, M., et al. 2002, *AJ*, **123**, 485
- Strauss, M. A., Weinberg, D. H., Lupton, R. H., et al. 2002, *AJ*, **124**, 1810
- Strigari, L. E., Bullock, J. S., Kaplinghat, M., et al. 2008, *Nature*, **454**, 1096
- Szokoly, G. P., Bergeron, J., Hasinger, G., et al. 2004, *ApJS*, **155**, 271
- Tammann, G. A., Sandage, A., & Reindl, B. 2008, *ApJ*, **679**, 52
- Taylor, E. N., Franx, M., van Dokkum, P. G., et al. 2009a, *ApJ*, **694**, 1171
- Taylor, E. N., Franx, M., van Dokkum, P. G., et al. 2009b, *ApJS*, **183**, 295
- Terlevich, A. I., Caldwell, N., & Bower, R. G. 2001, *MNRAS*, **326**, 1547
- Terlevich, A. I., Kuntschner, H., Bower, R. G., Caldwell, N., & Sharples, R. M. 1999, *MNRAS*, **310**, 445
- Tollerud, E. J., Bullock, J. S., Strigari, L. E., & Willman, B. 2008, *ApJ*, **688**, 277
- Toomre, A. & Toomre, J. 1972, *ApJ*, **178**, 623
- Toth, G. & Ostriker, J. P. 1992, *ApJ*, **389**, 5
- Trager, S. C., Faber, S. M., Worthey, G., & González, J. J. 2000, *AJ*, **120**, 165
- Tucker, D. L., Kent, S., Richmond, M. W., et al. 2006, *Astronomische Nachrichten*, **327**, 821
- van Dokkum, P. G. & Franx, M. 2001, *ApJ*, **553**, 90

BIBLIOGRAPHY

- Vanzella, E., Cristiani, S., Dickinson, M., et al. 2008, *A&A*, **478**, 83
- Vanzella, E., Cristiani, S., Dickinson, M., et al. 2005, *A&A*, **434**, 53
- Vanzella, E., Cristiani, S., Dickinson, M., et al. 2006, *A&A*, **454**, 423
- Velazquez, H. & White, S. D. M. 1999, *MNRAS*, **304**, 254
- Visvanathan, N. & Sandage, A. 1977, *ApJ*, **216**, 214
- Vivas, A. K., Zinn, R., Andrews, P., et al. 2001, *ApJ*, **554**, L33
- Walsh, S. M., Willman, B., & Jerjen, H. 2009, *AJ*, **137**, 450
- White, S. D. M. 1978, *MNRAS*, **184**, 185
- White, S. D. M. & Rees, M. J. 1978, *MNRAS*, **183**, 341
- Wilhelm, R., Beers, T. C., & Gray, R. O. 1999, *AJ*, **117**, 2308
- Willman, B., Dalcanton, J. J., Martinez-Delgado, D., et al. 2005, *ApJ*, **626**, L85
- Wolf, C., Meisenheimer, K., Kleinheinrich, M., et al. 2004, *A&A*, **421**, 913
- Wolf, C., Meisenheimer, K., Rix, H.-W., et al. 2003, *A&A*, **401**, 73
- Worthey, G. 1994, *ApJS*, **95**, 107
- Xue, X., Rix, H., Yanny, B., et al. 2010, *ArXiv e-prints*
- Xue, X. X., Rix, H. W., Zhao, G., et al. 2008, *ApJ*, **684**, 1143
- Yanny, B., Newberg, H. J., Grebel, E. K., et al. 2003, *ApJ*, **588**, 824
- Yanny, B., Newberg, H. J., Johnson, J. A., et al. 2009, *ApJ*, **700**, 1282
- Yanny, B., Newberg, H. J., Kent, S., et al. 2000, *ApJ*, **540**, 825
- Zel'Dovich, Y. B. 1970, *A&A*, **5**, 84
- Zheng, Z., Shang, Z., Su, H., et al. 1999, *AJ*, **117**, 2757
- Zucker, D. B., Belokurov, V., Evans, N. W., et al. 2006, *ApJ*, **643**, L103
- Zwicky, F. 1933, *Helvetica Physica Acta*, **6**, 110

ACKNOWLEDGEMENTS

First of all I want to thank Eric Bell for his supervision, his help and his friendship over the last years. Although communication became somewhat more complicated with an ocean and 6 hours of time difference between us, he always tried hard to support me the best he could. Many thanks also for inviting me for three visits to Ann Arbor and the help with various organisational things concerning that, especially for my extended stay this year. A huge thanks to the whole Whitebell family for hosting me at their home so many times, their friendship and help.

Many thanks also to Hans-Walter Rix for his help and support, especially after Eric moved to Ann Arbor, and also for participation in the defense committee and refereeing my thesis.

I also thank Eva Grebel for taking part in my IMPRS committee and the many helpful suggestions for my work that came out of these meetings. Many thanks also for the letter writing and agreeing to participate in my defense committee and refereeing my thesis.

Many thanks also to Norbert Christlieb and Werner Aeschbach-Hertig for agreeing to participate in my defense committee.

Also I would like to thank a lot of people at the MPIA for their help and friendship over the years I spent there. I don't want to list names here, since I will probably forget someone. So I want to thank the MPIA students in general and especially the student coffee break crowd and my great officemates for the uncounted times I didn't even have to leave my chair to get a problem solved. I also want to thank the IMPRS students, especially the third generation, and Christian Fendt for the opportunity to get to know some people in the other Heidelberg astronomy institutes. Also I would like to thank the members of Eric's former group at MPIA who always helped me a lot with various problems.

Last, but not least, I also want to thank Steffen and my family for all their support.

